Università degli Studi di Milano-Bicocca

Dipartimento di Fisica

Ph.D. Thesis

OPTIMIZATION AND CHARACTERIZATION OF PET SCANNERS FOR MEDICAL IMAGING.

Giacomo Cucciati

Supervisor:
Prof. Marco Paganoni

Corso di Dottorato in Fisica e Astronomia Ciclo XXVI
Settore Scientifico Disciplinare FIS/07

Anno Accademico 2013-2014

Abstract

Positron emission tomography is an imaging technique that appeared to be a valid instrument for cancers detection and neuro-imaging studies. Since first models built during 1960s, an incredible effort has been done by researchers to develop scanners more and more advanced with higher specificity and efficiency. Monte Carlo simulations have shown to be a very important tool during design phase of PET prototypes thanks to their ability to simulate systems with many coupled degrees of freedom, as it happens when particles interact with matter. This Thesis work has started in the frame the Crystal Clear Collaboration when the EndoTOFPET scanner was already under development. This prototype is an high spatial resolution scanner for the study of pancreatic carcinoma and prostatic cancer, composed by a PET head mounted on an ultrasound endoscope and a PET plate to be placed outside the body. The Collaboration has chosen to use Monte Carlo simulations to support the design of this project and two simulations toolkits were available: Geant4 and SLitrani. In this work both the toolkits are studied and ray tracing in scintillator crystals are tested. In particular photon extraction efficiency is simulated under different surface treatments as coating and wrapping. Also the influence of the crystals geometry on light output is tested simulating different scintillators sections and lengths. Both Geant4 and SLitrani have shown to give similar results under these conditions. A main issue was observed regarding secondary particles since Geant4 is able to simulate their production while it is not possible with SLitrani. On other hand crystals anisotropy for optical photons can be activated in SLitrani. Light yield measurements were performed in laboratory on LYSO and $PbWO_4$ crystals to have a comparison with the results obtained by mean of simulations. Good agreements are obtained for what regards surfaces treatments while more tuning was required to simulate the effect of surface imperfections and diffusion inside crystals.

For the Collaboration purposes, Geant4 results more reliable and it allows to use GATE, an open source software specifically developed for the simulation of medical imaging scanners. Due to the peculiar structure of the PET prototype it was necessary to develop a code to simulate the electronic chain, responsible for transforming the gammas detected in usable data for image reconstruction. Different coincidences sorting algorithms were studied and methods to introduce instrumental uncertainties in data were developed and reported in this work. Simulations of EndoTOFPET scanner with different scintillator dimensions, modules geometries and plate configurations were performed. Sensibility and spatial resolution were used as elements of comparison and results collected by simulations are reported and analysed in this work. Time of flight was tested applying different time resolutions while system response to DOI analysis was studied too. Thanks to these first simulations, valuable information for the developing of this prototype were collected.

Acknowledgement

In my opinion this is always the most difficult part to write at least as the title. This is the reason I keep it at last. Every time I am worried to forget someone, to be too concise (the opposite is impossible) or too vague. Apparently it is not even possible to write down just a list of names... So let's start in the old fashioned way and I hope that will be enough!

First of all I want to thank my supervisor, Marco, for the opportunity he gave me to work on this project and in particular to work inside the CERN walls. Even if I lived a very small part of what this international organization can offer it was a great experience! For this reason I want to thank also the Crystal Clear Collaboration and all its members (the ones I met at least). In particular, a thank to Etiennette, key figure of what showed to be a very good team. Avoiding a long list of names of all the people I have worked with, a special thank to the *RS task force*, that means: Ben (I hope I have been a good office colleague for him), Aron (the beer guy) and Milan (most of the time a voice in the headphones)! And of course I want to thank also the Italian group (too many!), colleagues and friends outside the walls of the office. I really don't like to list all of them, so lot of thanks to Marco and Nicolas for their help in this work and I let them spread the word to the other guys... To be honest a double thank to Marco and Alessio for the revision of my Thesis.

I have already written too many lines and my family will understand if I stop here. I will have the opportunity to thank them in person. I hope that the same will be with all the other people I mentioned and who I don't.

Almost a page... not bad.

17/01/2014

Contents

List of Figures

List of Tables

List of abbreviations

ADC: analog digital converter.
APD: Avalanche photodiode.
BGO: Bismuth-Germanate-Oxide.
CCC: Crystal Clear Collaboration.
CeF_3: Cerium Fluoride.
CERN: European Organization for Nuclear Research.
CMS: Compact Muon Solenoid.
CS: coincidences sorter.
CT: computerized tomography.
CTR: coincidence time resolution.
d-SiPM: digital silicon photo-multipliers.
DAQ: data acquisition.
DOI: depth of interaction.
ECAL: Electromagnetic Calorimeter.
EM: electro-magnetic.
ET: emission tomography.
FDG: fluorodeoxyglucose.
FOV: field of view.
FWHM: full width half maximum.
G4: Geant4.
LHC: Large Hadron Collider.
LOR: line of response.
LSO: Lutetiumoxyorthosilicate.
LYSO: Lutetium Yttrium Oxyorthosilicate.
MC: Monte Carlo.
MPPC: multi-pixel photon counter.
MRI: magnetic resonance imaging.
NaI: Sodium Iodide.
PET: positron emission tomography.
PMT: photomultiplier tube.
ROI: region of interest.
$PbWO_4$: Lead Tungsten Oxide.
PSF: point spread function.
PSMA: prostate-specific membrane antigen.
SiPM: silicon photomultiplier.

SL: SLitrani.
SPAD: single-photon avalanche diode.
SPECT: single photon emission computed tomography.
STD: standard deviation.
STR: single time resolution.
TOF: time of flight.
UV: ultraviolet.

Chapter 1

INTRODUCTION

1.1 Thesis overview

During my master degree studies I used Monte Carlo simulations software for physics applications. They play an important role in this sector, thanks to their ability to predict particles behaviour under defined conditions and they are greatly used from the biggest high energy physics experiments to the smallest radiation detectors. My interest for simulation software has brought, thanks to my Tutor, to conceive the guide lines for this Ph.D. thesis. Working side by side with physicists of the Crystal Clear Collaboration at CERN, I had the opportunity to study in deep how Monte Carlo simulators work and I was able to support the developing of an innovative PET scanner, an international project started in the frame of the CCC. My thesis follows the steps of the work I conducted during these three years of my Ph.D.:

- in Chapters 2 and 3, I will briefly explain the groundwork of how PET scanners work and the theory of scintillator crystals. It should act as support to better understand the analysis I have conducted and explained further in the thesis. A section is dedicated to the CCC projects I worked in;
- Chapter 4 is an introduction to Monte Carlo simulations and to the software I have studied, Geant4 and SLitrani. I will try to explain with more details how these software handle optical photons and ray tracing in crystals;
- in Chapter 5, I show the analysis I conducted on Geant4 and SLitrani and their comparison, with a particular attention to light yield measurements and anisotropic crystals;
- in Chapter 6 I will explain the study I have conducted on the EndoTOFPET scanner using Monte Carlo simulations;

- eventually conclusions are reported in Chapter 7.

1.2 Crystal Clear Collaboration, a technology transfer.

Crystal Clear Collaboration [1] was founded in 1990 at CERN. Its activity was focused on the study and development of scintillator crystals to be used as particles detectors in physics experiments related to LHC [2]. In this collaboration experts coming from different disciplines as material science and instrumentation for particle detection were grouped to work side by side, creating a world wide community of about 250 scientists. One of the main goal achieved by CCC during the first years was the study of the $PbWO_4$ scintillators and the decision in 1994 to apply these crystals to the electromagnetic calorimeter of CMS [3]. Knowledge acquired in this period naturally flowed in medical imaging applications where scintillators crystals were already applied for PET and SPECT scanners. Less bulky scanners, higher spatial resolution and lower energy particles are some of the different working conditions to which crystals have to be adapted from LHC to medical application. New scintillator materials and new technologies for particles detectors were studied by the collaboration and, once formed a background experience, the collaboration has started some international projects in medical imaging. Milestones of the collaboration:

- *ClearPET*: for dynamic studies of mice and rats with an high spatial resolution;
- *ClearPEM-Sonic*: a multimodal mammography system PET-Ultrasound;
- *EndoTOFPET*: an innovative endoscopic PET scanner.

Chapter 2

POSITRON EMISSION TOMOGRAPHY

2.1 The technique

Positron emission tomography (PET) is a technique belonging to a main branch of medical imaging called emission tomography (ET) which uses radioactive materials to image properties of the body's physiology [4]. Another technique based on the same main principles is single positron emission tomography (SPECT). Images from a PET exam can represent, for example, the spatial distribution of properties such as glucose metabolism, blood flow, and receptor concentrations. Thus, emission tomography can be used to detect tumours, locate areas of the heart affected by coronary artery disease, and identify brain regions influenced by drugs. ET is categorized as a functional imaging approach to distinguish it from methods such as X-ray computed tomography (CT) that principally depicts the body's architectural structure (anatomy).

2.1.1 The tracer

The main agent of the PET technique is the tracer. It must play two roles: move inside the patient's body in order to reach the physiological parts to investigate and emit an unique signal that can be received by an external detector and identify its position. At the same time without harming the patient himself.

Some radionuclides show to be good candidates because:

- they are not normally present in the human body and their presence can be explained only by human intervention;

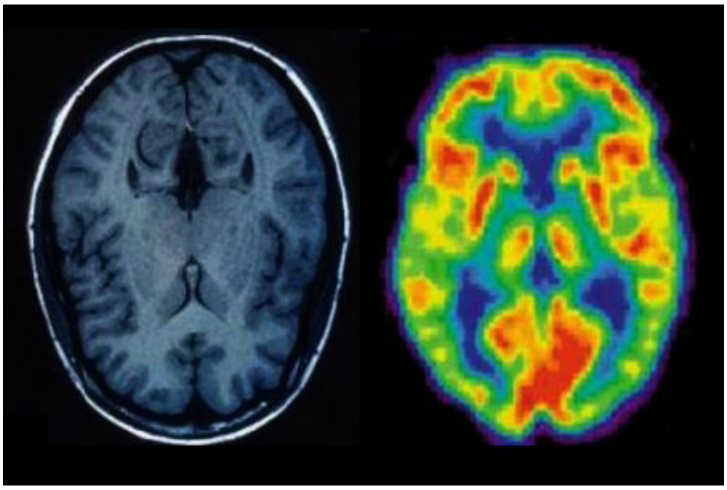

Figure 2.1: Neuronal activity can be easily studied by mean of a PET scanner and the injection of FDG in the body.

- their nuclear decay produces a characteristic gamma emission that can exit the human body with a low probability of being absorbed and so be received and recognized by an external detector;
- they can be included in some molecules that are normally present in physiological processes and so reach specific organs or follow particular metabolisms;
- they are safe for human body from a chemical point of view.

One of the most used radiochemical compound is the ^{18}F-fluorodeoxyglucose (^{18}F-FDG). It is a tracer for measuring glucose metabolism and it consists of two components: FDG (similar to glucose) and a fluorine-18 label (^{18}F) that permits to detect the tracer by counting the gamma-ray emissions it produces. ^{18}F-FDG enters cells in the same way as glucose, but it is metabolised by the cell to create a new compound (a metabolite) that remains trapped within the cell. Therefore, the concentration of the radioactive metabolite grows with time in proportion to the cell's glucose metabolic rate. In this way, injection of ^{18}F-FDG into the body allows to form images depicting local levels of glucose metabolism. ^{18}F-FDG is a valuable tool for brain imaging because the glucose metabolism is related to the regional level of neuronal activation (Figure 2.1). In recent years, ^{18}F-FDG has also become an extremely important agent for cancer imaging because malignant tumor cells normally exhibit greatly increased glucose metabolism in comparison with normal cells. Thus, malignant tumors are highlighted in ET images as bright regions against the relatively dark background of surrounding normal tissues.

2.1.2 PET analysis

Some radionuclides belong to the class of decay β^+. This process can be outlined by the following equation:

$$p \rightarrow n + e^+ + \nu$$

where a proton of the atomic nucleus is converted in a neutron with the emission of a positron and an electronic neutrino which leaves the decay zone undisturbed due to the negligible interaction probability [5]. Positrons behaviour is different: as they travel through human tissue, they loss their kinetic energy principally by Coulomb interactions with electrons. Because the rest mass of the positron is the same as the electron, positrons may undergo large direction deviations at each Coulomb interaction and they will follow a tortuous path through the tissue. When the positrons reach thermal energies, they interact with electrons by the formation of a hydrogen-like orbiting pair called positronium. Positronium is unstable and eventually decays, via annihilation, into a pair of anti-parallel 511 keV photons (emitted at 180° relative to one another). The PET analysis is based on this decay family to estimate the radionuclide distribution inside the patient body. In fact if both emitted gammas are intercepted by two different detectors, it could suppose that the annihilation happened somewhere along the line they have followed (called LOR, line of response). But if more than one atom decays in the same area, it is possible to collect intersecting LORs and, generally speaking, the higher the concentration of tracer in a specific point the larger the number of intersections. During a PET exam a large number of gamma couples is collected all around the body since the tracer diffuses in the circulatory system but, as mentioned before, areas with an higher concentration of radionuclides will appear. Applying mathematical algorithms based on the previous assumption to the data collected it is possible to recognize and reconstruct graphically these areas with a very good spatial resolution (see Figure 2.2).

For this reason a tracer meant to be used in PET analysis has the further characteristic that the radionuclide decays β^+. In the example of the ^{18}F-fluorodeoxyglucose, the fluorine isotope decays in a oxygen atom with the typical emission of a positron and a electronic neutrino as shown in the following schema:

$$^{18}_{9}\mathrm{F} \rightarrow {}^{18}_{8}\mathrm{O} + e^+ + \nu_e$$

When a gamma ray hits a crystal and its energy is converted in an electric signal, the data acquisition system starts a very fast countdown (few nanoseconds) waiting to detect the second gamma belonging to the same decay. If another signal is registered within this time window the event is saved as a coincidence and it is

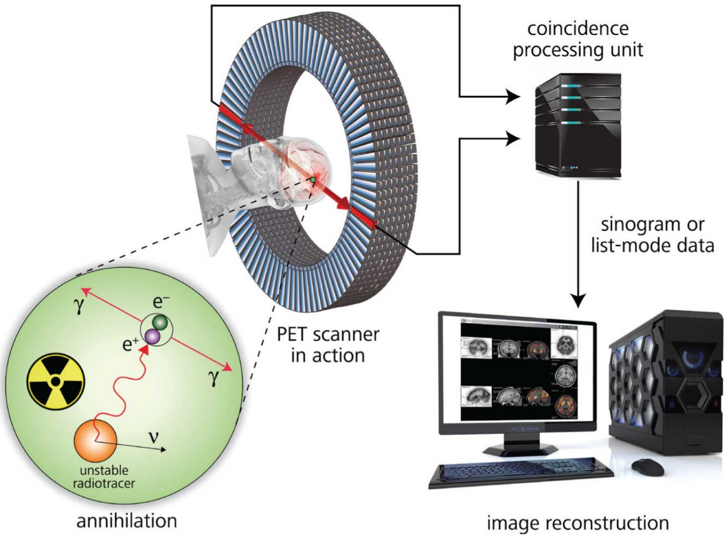

Figure 2.2: A scheme of how the PET technique works, from the decay of the radiofarmaceutical to the elaboration of the final image.

possible to create a LOR. If not, the first signal is rejected. The electric signal is proportional to the energy released in the detector by the gamma and after an acquisition cycle the system is able to create an energy spectrum with all the data collected. This spectrum shows a characteristic shape: a peak around 511 keV and an edge at lower energies (see Figure 2.3).

In fact, even if all the annihilation gammas are created with 511 keV, only some of them will convert the whole amount into a signal. Along the path from the decay position to the detector, photons can interact with the electrons of the medium they cross (patient body) and partially lose their energy (the collision will change also the direction of the gammas themselves). Moreover a photons can cross the detector without releasing all its energy. It means that, if detected, they will create a signal lower than 511 keV. Applying an energy window to these spectra it is possible to extract only gammas belonging to the photopeak and generate the coincidences LORs with them.

2.1.3 Coincidence events

Figure 2.4 illustrates three kinds of coincidence events that the device accepts:

- *true coincidences*: both gamma rays detected come from a single decay and they have not scattered in the patient;
- *scattered events*: one or both gamma rays have been scattered within the patient;

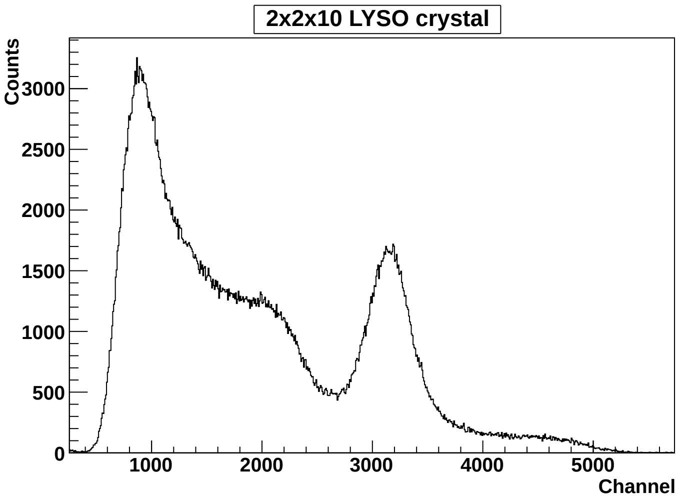

Figure 2.3: A typical photopeak and Compton edge acquired with a scintillator crystal used in a PET device.

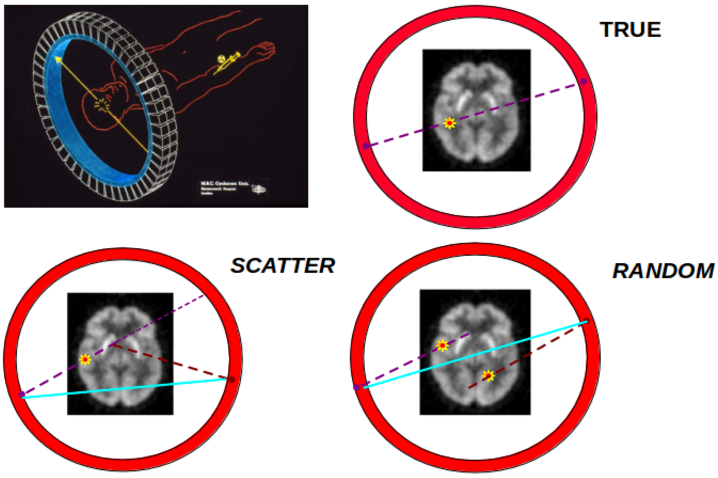

Figure 2.4: A scheme of how true, scattered and random coincidences are generated. The crystals ring array is a very common configuration in PET devices because it has simultaneously a 360° angle of view, as explained in Section 2.1.5.

Isotope	**Half Life (min)**	E_{max} **(keV)**	$Range_{max}$ **(mm)**
^{18}F	109.8	663	2.6
^{11}C	20.3	960	4.2
^{13}N	9.97	1200	5.4
^{15}O	2.03	1740	8.4
^{82}Rb	1.26	3200	17.1

Table 2.1: Table of the most common radioisotopes used in medical imaging.

- *random coincidences*: two gamma coming from two separate decays but happened simultaneously (or almost).

The goal in PET imaging is to measure and reconstruct the distribution of true coincidences while minimizing the scattered and random coincidences because they carry wrong information of the place where the decay happened. Note that both true and scattered events are referred as prompt events because they come from the decay of a single nucleus and, thus, the gamma rays are detected together. Random, or accidental, coincidences occur if two separate decays are close enough in time to look like a single decay to the system electronics. The prompt rate (trues + scatters) is related linearly to the activity in the patient. However, the randoms rate increases as the square of the activity in the patient and becomes more dominant at higher activity levels. Increasing the number of true coincidences leads to less noise in the image and an higher spatial resolution of the distribution of decay events in the reconstructed image is obtained. Since scattered events carry lower energy than true coincidence, as explained before, most of them can be easily rejected by energy spectra analysis.

2.1.4 Intrinsic spatial resolution limits

The spatial resolution of PET imaging is limited by the fundamental nature of positron annihilation [7]. Although the radial distribution of annihilation events is sharply peaked at the origin (site of positron creation), a calculation of the radius that includes 75% of all annihilation events gives a realistic comparison of the impact of the maximum positron energy on the spatial resolution of PET imaging. Table 2.1 lists the major emitters used in PET imaging, along with positron energy and range in water.

In addition to the positron range, the variation in the momentum of the positron also leads to a limitation of the spatial resolution of PET imaging. One would normally expect the annihilation gamma rays to be anti-parallel. However, the variation in momentum of the positron results in an angular uncertainty in the direction of the 511 keV photons that is approximately 4 mrad (0.23°) [6]. This is referred to as non-collinearity. A third significant factor limiting PET spatial resolution is the intrinsic spatial resolution of the detector. The resolution of a single detector is often quantified by the full width at half-maximum (FWHM) of the position spectrum obtained for a collimated point source placed before the detector at a fixed distance from it. The coincidence detector-pair resolution is normally specified as the FWHM of the point-spread function (PSF) obtained from the convolution of the two individual detector PSFs. For a detector composed of small discrete crystals, all interactions are assumed to occur at the center of individual crystals for the purpose of and image reconstruction. As a result, the PSF for such detectors is similar to a step function with a total width equal to the size of a crystal. The coincident PSF is, therefore, a triangular function whose base width is again equal to a crystal size. Thus, the FWHM of the coincident detector PSF is one-half the crystal size.

A final factor affecting PET spatial resolution is referred to as the parallax error, which results from the uncertainty of the depth of interaction (DOI) of the gamma rays in the crystal. Gamma rays may travel unknown distance in the crystal (or adjacent crystals) before being completely absorbed. As a result, if the gamma ray enters the crystal at an oblique angle, the location of the interaction will not be the same as the point of entry into the crystal; the crystal of the interaction may not even be the same as the one first entered (cross-talk event). Thus, unless the DOI within a crystal can be accurately determined, an incorrect line of response (LOR) will be assigned to this interaction because the LOR is normally assigned to a position at the front of the crystal of interaction (see Fig. 2.5). The parallax effect worsens as the source position moves radially away from the center of the scanner because a larger fraction of the gamma rays enter the crystals at oblique angles.

2.1.5 Detector design

The first element of the detection apparatus that a gamma ray strikes is a crystal material called a scintillator. The scintillator uses energy from the high-energy gamma ray to produce many optical-wavelength photons (see Chapter 3). These photons are detected by a collection of photomultiplier tubes (PMTs), devices based on the photoelectric effect. From a single photoelectron, a PMT can produce a cascade of electrons, which yields a measurable electrical current (Figure 2.6). This current is sensed by accompanying electronic, which registers the occurrence of an event. Relative readings from PMTs near the point of impact of the gamma ray are used to compute spatial coordinates of the gamma-ray event and a couple of these coordinates allow the reconstruction of a single LOR in the space. Since the PET

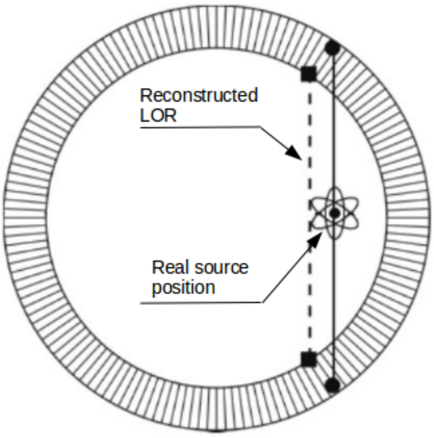

Figure 2.5: Scheme of the parallax error computed when no DOI information is collected.

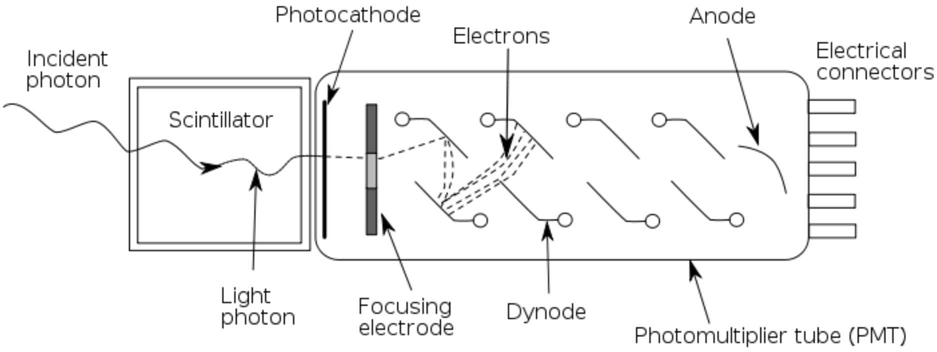

Figure 2.6: Scheme of the functioning of a photomultiplier.

technique is based on the detection couples of gammas emitted back-to-back by the source, devices show a geometry with a typical cylindrical symmetry.

Detector module designs use either large continuous crystals or arrays of discrete crystals. The first systems offer a lower price due to the lower cost of the scintillator and the use of fewer electronics channels, whereas the discrete crystal machines offer higher sensitivity due to the higher stopping power of the scintillators used (e.g., BGO, LSO, or GSO) and much higher count-rate performance. Sensitivity of a PET scanner is defined as the rate in counts per second between detected true coincidence events and a given source activity. It is one of the parameters used to compare performance of different PET machines. In either case, the detectors can be configured as full rings (more rings together to form a cylinder) that completely surround the patient or as partial rings with rotational motion to obtain the needed angular sampling. For example, designs with NaI(Tl) crystals may use six large 25-mm-thick curve plates while discrete crystal designs use BGO (25-30 mm thick), LSO

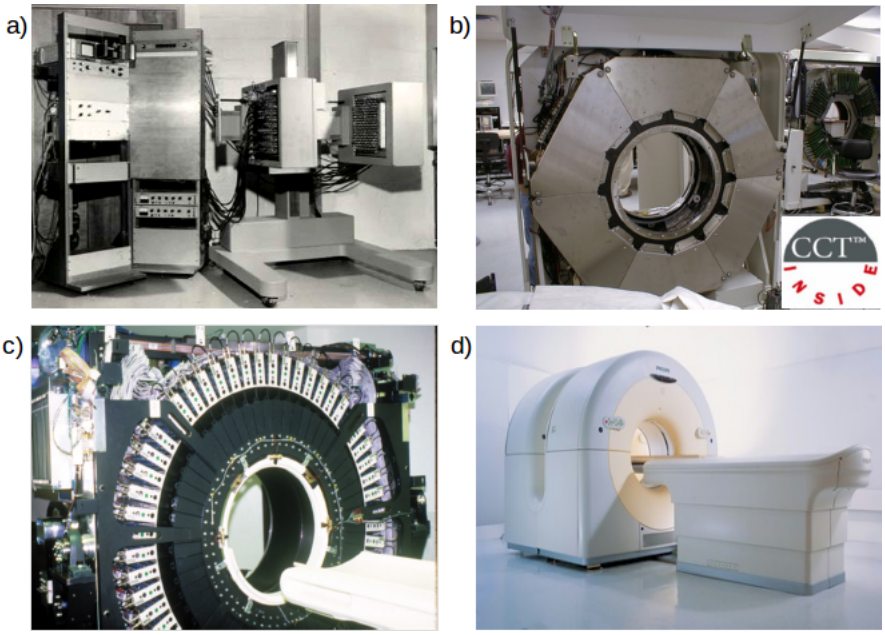

Figure 2.7: a) PC-I, the first tomographic PET imaging device. b) A continuous wide area PET system. c) Advannced GE model. d) A modern PET system for medical application.

(typically 25 mm thick) or GSO (typically 20 mm thick) arranged in full or partial rings around the patient. Because the NaI(Tl) system use continuous detectors, the axial sampling is determined by the intrinsic spatial resolution of the system and the choice in how the data are collected. These full-ring NaI(Tl) systems are operated exclusively in 3D mode (as explained below) to achieve better sensitivity. Rings in discrete crystals systems are divided in blocks of matrices where each single unit can contain for example 6×6 or 8×8 very small crystals ($6.25\times6.25\times30$ mm^3 BGO crystals or $6.7\times6.75\times25$ mm^3 LSO crystals). For these devices the spatial resolution depends on the crystal dimension itself so research facilities are developing PET devices that mount crystals with smaller and smaller sections (for spatial resolution thickness has a minor relevance). Some examples are shown in Figure 2.7.

Since each crystal needs a dedicated electronic, acquisition system complexity grows with the crystals miniaturization and sets a technological limits to the improvement of spatial resolution. Moreover block detectors generally use smaller PMTs than designs with continuous crystal so they are more expensive (due to the increased number of PMTs and electronic channels). Discrete crystals systems are equipped with removable axial collimators, allowing the systems to operate in either 2D or 3D mode. The GSO systems do not include axial collimators and only operate in 3D mode, as do the NaI(Tl) scanners.

In order to increase the acquisition rate (and inject less dose), also coincidences

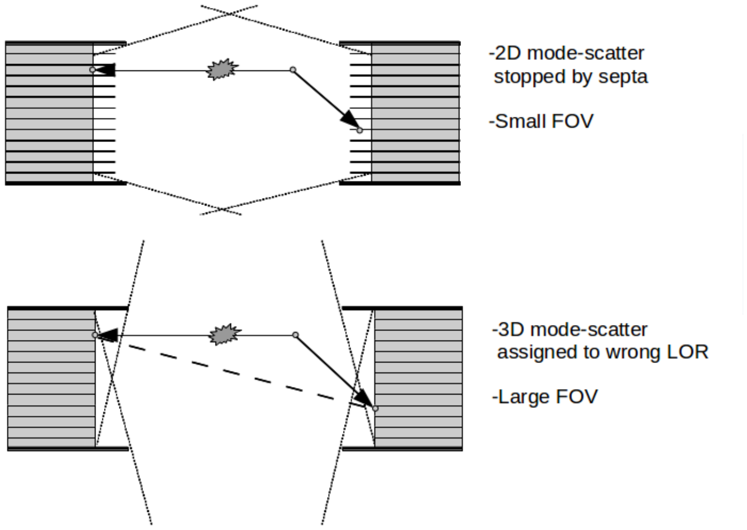

Figure 2.8: Scheme of advantages/disadvantages in using 2D and 3D mode.

detected by two scintillators with different axial depth are accepted. Axial collimators are able to absorb gammas with incident angles too far from the plane normal and different collimators lengths can be chosen to set how tight is the cut (see Figure 2.8). A system without collimators collects in what is called 3D mode. It offers an increase in sensitivity compared to 2D acquisitions. However, there are some limitations because the increased sensitivity is not uniformly distributed axially and the removal of collimation also increases the number of scattered events detected by the detector array. The removal of the collimation also allows more photons from outside the axial FOV to be detected. This increase in the number of single events detected versus the number of coincidence events detected leads to higher dead time and randoms rates.

2.1.6 Sensitivity improvements

The four major options for improving the number of coincidences read during an exam (the sensibility of the instrument) are:

- Increase the patient dose;
- Use more of the energy spectrum;
- Increase solid angle;
- Use more efficient scintillators/detectors.

Increasing the patient dose is not a practical approach because higher doses would result in higher radiation exposures for the patient moreover this would be advantageous only for fast systems not count-rate limited at high activity levels. One approach to gain sensitivity is to use more of the energy spectrum and accept events with energies below the photo peak. It means to accept scattered gammas as good signals with a consequent degradation in the images spatial resolution. The third method consists of the removal of all axial collimation (3D volume imaging) allowing in this way also coincidences with gammas intercepted by different ring arrays. A typical whole-body ring system can realize an increase in the true sensitivity by a factor of 5 but the penalty is a large increase in the acceptance of scattered photons and increased singles rates from activity outside the field of view (FOV) of the system. So this technique proves to be usefully only for dedicated PET system (as brain imaging) with small rings diameter.

Many research facilities are searching for better scintillators, but it's not easy to create materials with higher stopping power than bismuth germanate (BGO). The main advantages of new scintillators such as lutetium oxyorthosilicate (LSO), in comparison to BGO, is the combination of high light output and fast decay. BGO-based systems typically use detectors 30 mm deep, which provide approximately 90% detection efficiency for 511 keV gamma rays (therefore, 81% coincidence efficiency). Although 100% detection efficiency would improve sensitivity even further, no systems have yet been built with basic detection efficiency greater than that provided by 30-mm-deep BGO crystals. Developing of scintillation crystals will be discuss in the next chapter.

2.2 CCC projects

This thesis work was conducted in the frame of the Crystal Clear Collaboration. When I joined the research group, it was working on two different projects, ClearPEM-Sonic, a dedicated PEM device with an ultrasound elastography system, and EndoTOFPET-US, a multimodal imaging technique (PET-ultrasound) for endoscopic pancreas and prostate exams.

They can be considered the state of art in their respective fields from the point of view of the technology and I had the opportunity to participate actively to both of them, hence I think important to conclude in this chapter a brief description of the two devices.

Figure 2.9: The room were ClearPEM-Sonic have been installed at Hopital Nord. The Aixplorer is in the foreground, ClearPEM in the background.

2.2.1 ClearPEM-Sonic

ClearPEM-Sonic is a multimodal breast imaging device that combines the advantage of metabolic PET imaging of a dedicated positron emission mammograph with the morphological and structural information provided by the ultrasound system Aixplorer, developed by the SuperSonic Imagine company (see Figure 2.9). Breast cancer can be considered as the first cancer as occurrence among women (almost 40 cases per 100.000 women per year). Its mortality is 23% of all cancer cases but an early detection can greatly reduce this number [8]. Different techniques are adopted for breast cancer detection as radiography, ultrasound or magnetic resonance imaging. Anyway, these modalities present problems mainly due to breast density, since healthy tissues and cancer appear very similar in these cases. Whole-body positron emission tomography is able to provide metabolic information, but high cost and poor spatial resolution reduces its use only as support to the previous ones. ClearPEM-Sonic [9] has been designed and developed to answer these requirements.

The fulcrum of the ClearPEM module is composed by two heads holding the PET detectors [10], [11]. Each of them consists of 96 matrices of 8×4 $2\times2\times20$ mm^3 LYSO:Ce crystals with a casing of $BaSO_4$ acting as matrix structure and reflector for optical photons. It was chosen to couple each matrix with 2 Hamamatsu S8550 4×8 APD matrices obtaining an active area about 46% of the total. In this configuration each crystal presents a double readout and depth of interaction information (DOI) is collected. A 360 ° complete acquisition can be obtained thanks to the rotation of a robotic platform where the two heads are mounted on and a full 3-dimensional breast image can be reconstructed. A rail allows the movement of the heads closer to the subject maximizing the solid angle coverage while the high interaction probability provided by the high crystal density gives us a high sensitivity. For instance the global detection efficiency in the centre of the plates has been determined to be 1.5% at a plate distance of 100 mm. The correction of the parallax error, through the DOI evaluation, and the small section of the crystals installed make ClearPEM an high spatial resolution PET scanner.

An important task of this project was the realization of a merging software tool. 3D images of the region of interest (ROI) are computed independently by both acquisition systems and they can be studied indipendently by physicians. But more interesting is the overlapping of the information carried by the FDG density map and the elastographic map that can help the identification of smaller malignant lesions. To follow and register the transducer position a magnetic tracking system (by Ascencion Technologies, Burlington, Vermont, USA) was chosen. The software will follow transducer position during an ultrasound acquisition and the data collected will be computed to rotate the 3D image in the PEM reference system [12].

With due approval, a first clinical trial on 20 patients [13] was starded at Hopital-Nord, Marseille. An example that demonstrated ClearPEM potential in breast cancer diagnosis is reported in Fig. 2.10. During the preliminary exam a multifocal breast cancer was detected in this patient. Two lesions have been revealed by the whole-body PET/CT scanner, one in the left breast and the second close to the axilla. Smaller lesions around the first one can be detected only using MRI. The high sensitivity and spatial resolution that ClearPEM can achieve allow the detection of those smaller spots. Unfortunately the second cancerous focus is too close to the thoracic wall and ClearPEM is not able to scan that region since it is out of the detector field of view. Completed the first tests, the clinical was recently moved at the San Gerardo Hospital (Monza, IT) where further tests studies will be performed.

2.2.2 ENDOTOFPET-US

The aim of EndoTOFPET-US project [14] is to study two completely different kind of cancers: pancreatic carcinoma, a very aggressive disease therapy resistant, and prostatic cancer, very diffuse but easy to cure if detected in the early stages. Whole-body PET devices have a poor spatial resolution and images are affected by noise coming form adjacent organs. For this reason the collaboration is developing an

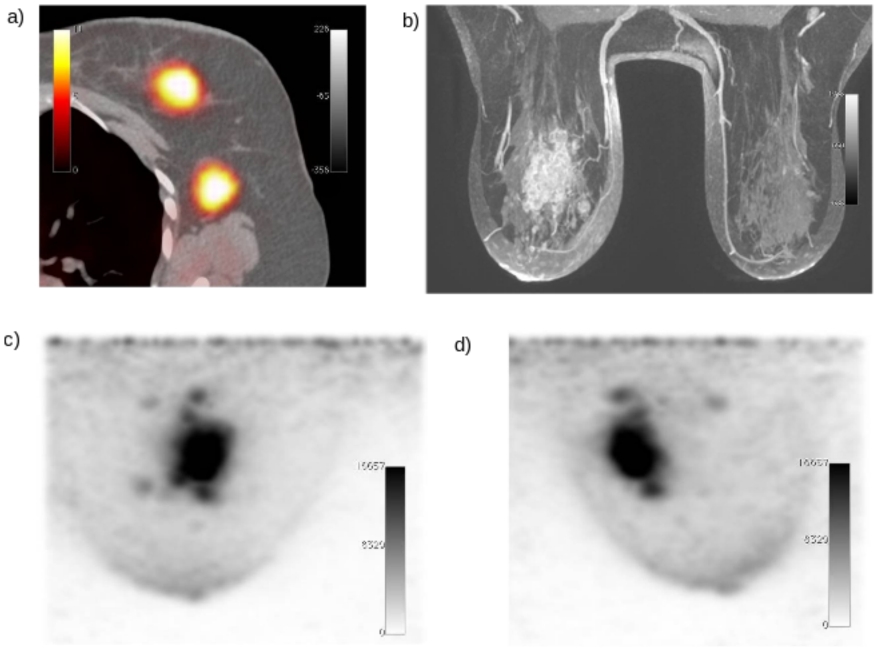

Figure 2.10: Images obtained using a Siemens Biograph 15 PET/CT (a), and using MRI (b). Figures (c) and (d) show the coronal and sagittal views respectively, of the ClearPEM images obtained with same breast.

high spatial resolution scanner composed by a PET head mounted on a commercial ultrasound endoscope and an outer PET plate to be placed outside the body (see Figure 2.11). Even if the probe is very close to the region of interest, noise from radiopharmaceuticals inside adjacent tissues can not be completely avoid because of the random and scatter coincidences. This problem should be solved using time of flight (TOF) measurements. *Time of flight* is a technique where time of detection of gammas on both the PET detectors are recorded. Using the difference of these values it is possible to calculate the origin of annihilation along the LOR:

$$\Delta x = \frac{c \cdot (t_1 - t_2)}{2}$$

Where Δx is the distance from the center of the system and c the light speed. Obviously a really good time resolution is required to be able to obtain a good estimation of the annihilation point and to be able reject scatter and random coincidences. The asymmetric configuration with a very small detector on one side is cause of a low detection efficiency. The reduced distance that the probe will have with the examined organ partially balances this effect because of the high counts rate. In order to enhance gammas detection, it was decided also to use heavy crystals with an high stopping power. All these features are possible only using advanced electronics and specific materials. The external plate is built starting from the ClearPEM

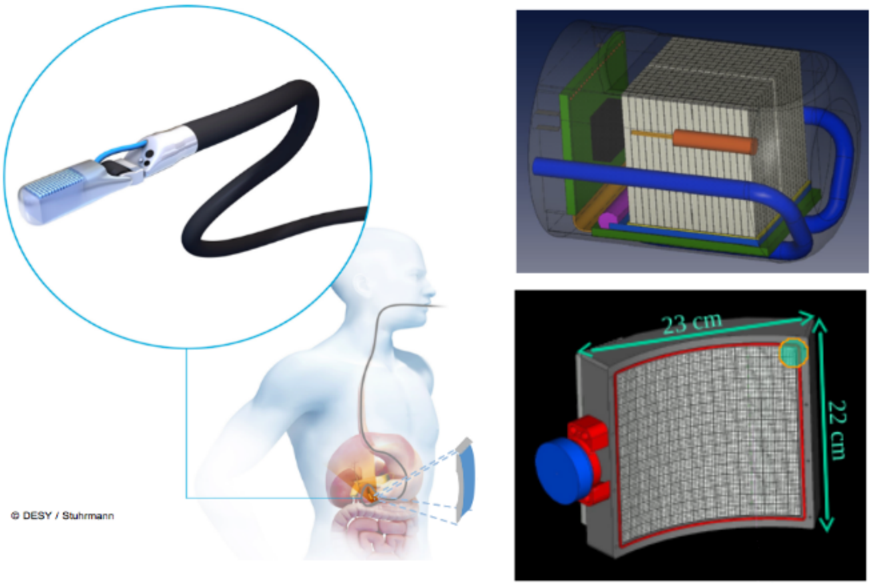

Figure 2.11: A scheme of the EndoTOFPET functioning with the details of the probe and the external plate.

project with further improvements. It is made of matrices of 4×4 LYSO:Ce crystals of $3.5\times3.5\times15$ mm^3. Each crystal matrix is coupled at the rear side to a 4×4 array analog MPPC for a plate total size of 230×230 mm^2 with 256 matrices or 4096 crystals. Cross-talk was tested for a typical matrix of the external plate and it is evaluated to be less then 5% of gamma interactions. It can be easily suppressed with a threshold setted to 30 keV The probe is a real challenge because of constraints that dimensions impose. It is made of thin ($0.71\times0.71\times15$ mm^3) LYSO:Ce crystals grouped into a matrix of 9×16 crystals. One such matrix is used for the pancreas probe, two matrices are used for the prostate probe. An EM sensor is added to track the probe position and a cooling system is required to control temperature. It is necessary to obtain a precision on probe positioning of about 0.5 mm to obtain a fine image reconstruction. For the internal probe, a digital silicon photo-multipliers (d-SiPMs) is dedicated to each crystal and coupled to it by mean of an optical light concentrator from one of the small crystal sides. Differently from standard SiPMs the collaboration is studying custom pixelized models that are able to collect 48 time values improving time resolution as Plot 2.12 shows [15]. The main goals of this project is to achieve a 200 ps time resolution and 1 mm as spatial resolution. The collaboration is working also on a dedicated image reconstruction algorithm to manage the asymmetric configuration of the EndoTOFPET scanner.

In collaboration with Aix Marseille Université and Université de Lausanne new biomarkers to be applied in EndoTOFPET exams are under investigation. For in-

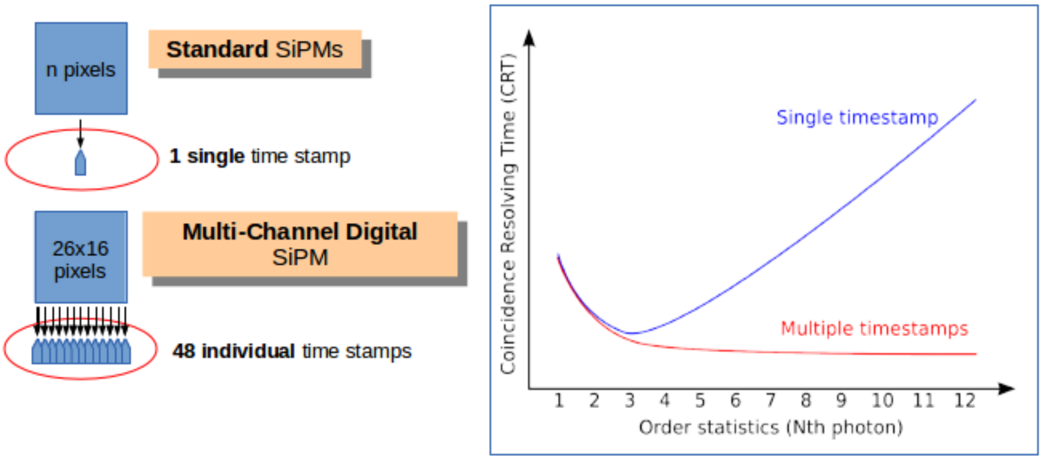

Figure 2.12: A scheme of the advantages of the experimental d-SiPMs tested by the research group.

stance, PSMA is an enzyme expressed by prostate epithelial cells that can be modified to contain ^{68}Ga becoming a very specific tracer for this cancer. Development of the EndoTOFPET scanner is ongoing, first components have been received and already tested with results encouraging the efforts of the collaboration. Pre-clinical trials are foreseen in summer 2014.

Chapter 3

SCINTILLATOR CRYSTALS

3.1 Scintillation process

Scintillation is a luminescence (flash of light) induced by ionizing radiation in transparent, dielectric media [16]. To explain the behaviour of scintillation process it is necessary to introduce the electronic band theory of a solid (see Figure 3.1). It describes the allowed ranges of energy that an electron within the solid may have and the forbidden ones. The existence of continuous bands of allowed energies can be understood starting with the atomic scale. The electrons of a single isolated atom occupy atomic orbitals, which form a discrete set of energy levels. If multiple atoms are brought together into a molecule, their atomic orbitals split into separate molecular orbitals each with a small energy difference. As more and more atoms are brought together the molecular orbitals extend larger and larger, and energy levels of the orbitals split apart to a finer and finer degree. Eventually, the collection of atoms form a giant molecule, or in other words, a solid. For this giant molecule, the energy levels are so close that they can be considered to form a continuum or *band*. *Band gaps* are essentially leftover ranges of energy not covered by any band. The most important bands and band gaps, those relevant for electronics and opto-electronics, are those with energies near the Fermi level:

- the *valence band* covers the higher energies where an electron is still considered bounded to individual atoms;
- the *conduction band* is the first range of electron energies where electrons move freely but sill within the atomic lattice of the material;
- the energies between these two zones are forbidden and they form the *band gap*. Electron can leave the valence band only if they obtain enough energy to reach the conduction band.

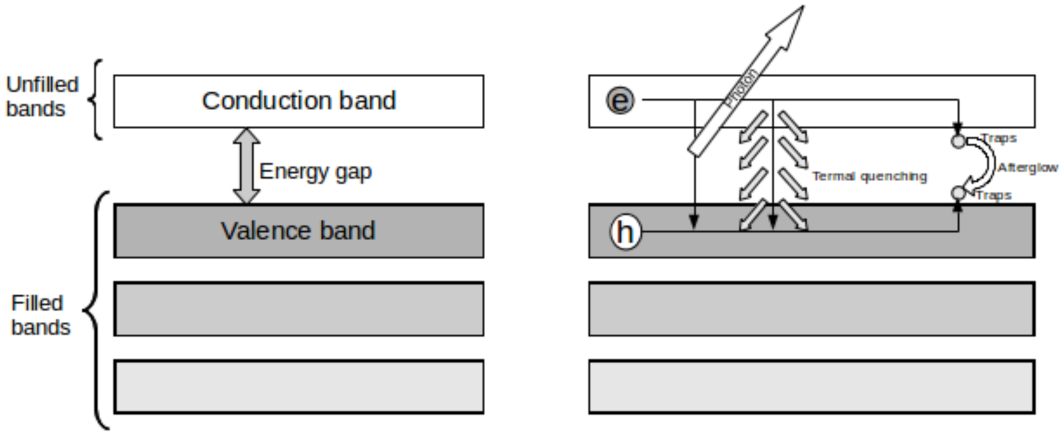

Figure 3.1: Scheme of the bands structure theory.

Material can be classified on their band gap. In insulators the energy required to an electron to jump the band gap is relevant, it becomes smaller in semiconductor (in some cases thermal energy can be enough to reach the conduction band) while in conductors the valence and conduction bands are so close to be overlapped and most energetic electrons are always free to move in the lattice. Described in a very simple way, scintillation process happens when an electron, previously excited, returns to the valence band releasing an optical photon. But contrary to the photoluminescence which results from the radiative relaxation of an excited ion, it is composed by a complex chain of phenomena.

In pure crystal, the return of the electron to the valence band with the emission of a photon is an inefficient process. Furthermore, typical gap widths are such that the resulting photon would be of an energy too high to be in the visible range. For this reason the scintillation process can take place only in a material that contains luminescent centres, i.e. atomic and lattice sites where the the transition between an excited and a lower energy state is favoured. These impurities, called activators, creates energy states within the forbidden gap through which the electron can deexcite back to the valence band. Because the energy is less than that of the full forbidden gap, this transition can now give rise to a visible photon and therefore serve as the basis of the scintillation process. The emission process is called intrinsic scintillation if the centre is of intrinsic nature, i.e. a consequence of the crystal structure. Centres of extrinsic nature are induced by voluntary doping or involuntary defects and impurities in the crystal and induce so-called extrinsic luminescence. Such a crystal is called scintillator and it can be considered as a wavelength shifter. It converts the energy (or wavelength) of a incident particle or energetic photon (UV, X-ray or gamma-ray) into a number of photon of much lower energy (or higher wavelength) in the visible or near visible range, which can be easily detect with current photo-multipliers or photo-diodes.

Scintillators can be divided into two major categories: organic and inorganic scintillators. These two groups differ both in their chemical composition as well as in the physical principles leading to light emission. In organic scintillators, the luminescence process is a consequence of transitions made by free valence electrons that occupy so-called molecular orbitals. It is thus a property of the molecular structure. On the contrary, the luminescence of inorganic scintillators is due to the electronic band structure of the crystal and thus a consequence of the crystalline structure.

During a scintillation process five main stages can be considered [17]. The first one starts with the production of primary *excitations* by interaction of ionizing particles with the material. For incident particle with very high energy, the excitations are essentially deep holes h created in inner-core bands (associated with core orbitals such as 1s electrons) and hot electrons e in the conduction band. Then, in a very short time scale (10^{-16}-10^{-14} s), a large number of secondary electronic excitations are produced through inelastic electron-electron scattering and Auger processes with creation of electrons in the conduction band and holes in core and valence bands. So at the end of this stage all the starting energy is divided in a electromagnetic shower and the multiplication of excitations is stopped. All electrons in the conduction band have an energy smaller than $2E_g$ (e-e scattering threshold) and all holes occupy the valence band if there is no core band lying above the Auger process threshold (general case). The second stage is *thermalization* of electronic excitations: hole and electron will cool their energy by coupling to the lattice vibration modes (with production of phonons) until they reach respectively the top of the valence band and the bottom of the conduction band. They can also be bound and form an exciton whose energy is in general slightly smaller than the band gap energy. The next stage is characterized by the localization of the excitations through their interaction with stable defects and impurities of the material. For example, electrons and holes can be captured by different traps or self-trapped in the crystal lattice. Excitons, self-trapped excitons, and self-trapped holes can be formed with emission of phonons. The two last steps are related with migration of relaxed excitations and radiative and/or non-radiative recombinations that lead to scintillation by different channels:

$$e + h \rightarrow h\nu \tag{3.1.1}$$

$$e + h \rightarrow ex \rightarrow h\nu \tag{3.1.2}$$

$$e + h + A \rightarrow ex + A \rightarrow A* \rightarrow A + h\nu \tag{3.1.3}$$

$$e + h + A \rightarrow A^{1+} + e \rightarrow A* \rightarrow h\nu \tag{3.1.4}$$

$$e + h + A \rightarrow (A^{1-}) * + h \rightarrow A + h\nu \tag{3.1.5}$$

$$A \rightarrow A* \rightarrow A + h\nu \tag{3.1.6}$$

where e and h are an electron and a hole, ex an exciton, A an activator ion and $h\nu$ a photon. The first two processes are the simple recombination of a free electron in the conduction band with a hole in the valence band (or deeper bands) that leads to the emission of a photon. A fast scintillation pulse (in UV energy range) is emitted if a deep hole (in bands closer to the core) recombines with en excited electron, it is the case of core-to-valence luminescence, Eq. 3.1.1. Recombinations of electron and hole sufficiently close to the band gap are more probable in particular if they can bind in the vicinity of specific atoms or lattice defects and form a so-called exciton (Eq. 3.1.2) the emission will be in the visible range. Process 3.1.3. describes the quenching of an exciton by the presence of activator ions, and subsequent excitation of the activator ion followed by the emission. Alternatively, as shown in Eq. 3.1.4 and 3.1.5, electrons or holes can be directly captured by an activator ion, a process competing with the formation of excitons. Finally, activator ions can be directly excited by ionizing radiation (see Eq. 3.1.6). The excited activator ions emit a photon when returning to their ground state.

3.2 Competitive process to scintillation

The scintillation process competes with other non-radiative phenomena that cause a loss of photons output [17]. One of these is called thermal quenching. It can be easily explained by Figure 3.2 where the coordinate Q represents the distance between the ion and the ligands while E is the energy. The two parabolas are the potential curves of the ground state and of one excited state. Both of them show a fine split of the energy levels due to the different vibrational modes. An initial equilibrium distance between the luminescent ion and the ligands increases after the electron relaxation of the excited state. The ion-ligand distance is in general larger in the excited state inducing a parabolas offset (Stoke shift) proportional to electron-phonon coupling. In intermediate and strong electrons-phonons coupling, parabolas show an intersection point that is crossed by higher vibrational levels. Electrons can reach these vibrational by thermal energy (E_q in the scheme) and a non-radiative transition may occur by a cascade of phonons instead of a photon

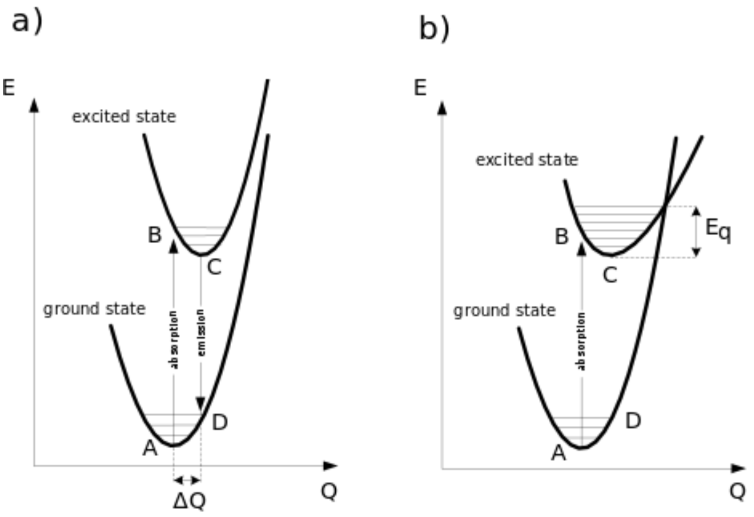

Figure 3.2: Scheme of the energy levels involved in competitive non-radiative phenomena.

emission. In some scintillators material, room temperature is high enough to enhance this phenomenon and consequently reduce scintillation efficiency. For example BGO has quantum efficiency of only 0.13 because of thermal quenching while Tl^+ and Ce^{3+}-doped scintillation crystals are almost immune. Concentration quenching is another mechanism that competes with the scintillation process. In fact interactions between luminescent centres take place by nonradiative energy transfer but their number increases with the doping material concentration in the crystal. A very good example is given by CeF_3, which has a modest light production in spite of a very high concentration of Ce^{3+} ions.

Light photons travelling in the scintillator material can be reabsorbed by a luminescent centre of the same nature that emitted the luminescence itself. In this case it is called radiative energy transfer and it does not affect light yield because sooner or later light will be remitted (we have a delay in the fluorescence decay). If the luminescent center is different a quenching phenomenon takes place and it become a very important limiting factor. Many kind of absorption centres can be present in crystals such as lattice distortions, point defects, color centres, etc.

An electron upon arriving at the impurity site can create an excited configuration whose transition to the ground state is forbidden. Such trap states then require an additional increment of energy to raise them to a higher lying state from which de-excitation to the ground state is possible. One source of this energy is thermal excitation and the resulting slow component of light is called phosphorescence. It can often be a significant source of background light or "afterglow" in scintillators.

3.3 Time response and light yield

The time shape of the light pulse emitted by the crystal can be represented by the following equation:

$$I = I_0(e^{-t/T} - e^{-t/T1}) \tag{3.3.1}$$

where T1 is the time constant describing the population of the optical levels (rise time) and T is the time constant describing their decay. A more complete formula should take into consideration that scintillating materials have two decay time: a fast (or prompt) value representing the fluorescence process and the slow (or delayed) value for phosphorescence and delayed fluorescence. While the fast component usually dominates, the relative amplitude of the two components depends on the scintillating material. Times of approximately half a nanosecond are required to populate the levels from which the prompt fluorescence light arises. For the very fast scintillators, the decay time from these levels in only 3 or 5 time grater, even if it can be even one or two order of magnitude different for slower material.

The number of electronic excitation N_{eh}, which are potentially available in the scintillation process, is expressed by:

$$N_{eh} = E_{inc}/E_{eh} \tag{3.3.2}$$

Where E_{inc} is the energy deposited by the ionizing particle and E_{eh} the average energy required to produce a thermalized e-h pair. E_{eh} is not really equal to the band gap but shows values two-three times E_{gap}. The light production of a scintillator crystal is called light yield and can be calculated by:

$$Y = N_{eh} \cdot S \cdot Q \tag{3.3.3}$$

with S as the efficiency of the energy transfer of thermalized pairs to the excited states of luminescent centres and Q is the luminescence quantum yield. These three parameters represent temporally the sequence of the three processes. As mentioned before quenching process reduces light yield as its concurrent process but its worse effect is reducing the linear response of light yield with energy deposited by the ionizing particle. In Section 5.6.1 the method I use to calculate crystals light yield will be explained.

3.4 Required properties in scintillator crystals

Scintillator crystals production uses several chemical compositions, each showing different responses under the same ionizing particles. Crystals are chosen depending on the aim of their use in order to fit with their characteristics and also PET imaging devices require scintillators with particular features, as listed below:

- stopping power: materials with high atomic number and density have an higher probability to stop gamma rays (high conversion efficiency) then "light" materials. It increases the number of detected signals, in this way a smaller crystal is able to obtain the same result of a sample bigger but with less stopping power. At the same time a smaller crystal achieves a better spatial resolution and a reduced the DOI influence for the reasons expressed in Chapter 2. BGO and Lutetium-based crystals are favoured in stopping 511 keV gamma rays;
- light yield: a high light yield is also mandatory to improve the energy resolution, which is essentially limited by photo statistics and electronic noise. In PET imaging a well defined photo-peak allows to reject a more correct number of Compton events (see previously) and to increase the image quality. At the same time light yield must behave linearly with particle energy deposition that can be unequivocally convert in an electric pulse;
- scintillation decay time: a fast scintillator response is required to keep a short dead time that is an higher acquisition rate. Moreover it is possible to reduce the gate time window that brings to a minor random acceptance.

All these properties can not be combine easily in a single crystal. For a long period NaI was very used in medical imaging because its considerable light yield and its easy and cheap production. But its low stopping power, long decay time and the not practical hygroscopy urged scientists to look for other materials. BGO crystals have been developed and introduced in PET devices to compensate for NaI weaknesses. As shown in Table 3.1 BGO has a very high stopping power and conversion efficiency. Unfortunately this material shows a small light yield and a not really fast decay time.

Recently a new material seems to summarized quite well all the properties required: Cerium doped lutetium orthosilicate or LSO:Ce and its variation LYSO:Ce where yttrium is used together with lutetium ion. More and more PET scanners are equipped with LSO and LYSO crystals since they are almost 10 times faster then BGO with a higher light yield but a similar density. In Table 3.1 the most important parameters that characterized a scintillator are shown.

	$NaI(Tl)$	BGO	LSO	GSO	$LYSO$	$LaBr_3$
Density (g/cm^3)	3.7	7.13	7.4	6.71	7.1	5.3
Effective Z	51		66	60	64	47
Abs. length 511 keV (cm)	3.0	1.04	1.15	1.42	1.12	2.13
Scint. efficiency (ph/keV)	60	9	25	8	32	61
Scint. efficiency (%)	100	15	75	20	14	175
Energy resolution (%)	7.8	12	9.1	7.91	7.1	3.3
Decay constant (ns)	230	300	42	60	48	35
Hygroscopic	Y	N	N	N	N	N

Table 3.1: Properties table of the most common scintillation materials.

3.5 Anisotropic crystals

In this chapter anisotropy in crystals will be briefly explained. This topic is extensively explained in [18] where more details of Maxwell equations and light transmission in materials are also covered.

3.5.1 Anisotropy and optical axes

An anisotropic medium is defined as a material whose electrical excitations depend on the direction of electric field. In general the vector **D** will then no longer be in the direction of vector **E** (cit Optics of crystals). It is possible to assume that each component of **D** is linearly related to the components of **E**:

$$\begin{cases} D_x = \epsilon_{xx}E_x + \epsilon_{xy}E_y + \epsilon_{xz}E_z \\ D_y = \epsilon_{yx}E_x + \epsilon_{yy}E_y + \epsilon_{yz}E_z \\ D_z = \epsilon_{zx}E_x + \epsilon_{zy}E_y + \epsilon_{zz}E_z \end{cases} \tag{3.5.1}$$

The quantities ϵ_{xx}, ϵ_{xy}, ... are supposed constant in the medium and they constitute the dielectric tensor. The principle of the conservation of energy requires this tensor to be symmetric so it has only six instead of nine independent components. The electric energy w_e can be expressed by:

$$w_e = \frac{1}{8\pi}\mathbf{E}\cdot\mathbf{D} = \frac{1}{8\pi}\sum_{kl} E_k\epsilon_{kl}E_l \tag{3.5.2}$$

and since we have only 6 terms ϵ_{kl}, we can write

$$w_e 8\pi = \epsilon_{xx}{E_x}^2 + \epsilon_{yy}{E_y}^2 + \epsilon_{zz}{E_z}^2 + 2\epsilon_{yz}E_yE_z + 2\epsilon_{xz}E_xE_z + 2\epsilon_{xy}E_xE_y \tag{3.5.3}$$

where x, y and z where used instead of corresponding **E** components. Both terms of the equation must be positive since on the left we have an energy and in this way we obtain the equation of an ellipsoid. It can be always transformed to its principal axes and it is possible to find a coordinate system in the crystal such that the equation of the ellipsoid is in a simpler form:

$$\epsilon_x {E_x}^2 + \epsilon_y {E_y}^2 + \epsilon_z {E_z}^2 = constant \tag{3.5.4}$$

In this system of principal dielectric axes the material equations and the expression for the electrical energy take the simple forms:

$$\begin{gathered} D_k = \epsilon_k E_k \qquad (\text{k = x, y, z}) \\ w_e = \frac{1}{8\pi}\left(\frac{D_x^2}{\epsilon_x} + \frac{D_y^2}{\epsilon_y} + \frac{D_z^2}{\epsilon_z}\right) \end{gathered} \tag{3.5.5}$$

ϵ_x, ϵ_y and ϵ_z are called the principal dielectric constants. They are a constant in the material but they could have a dependency on the frequency (and consequently the six terms of the dielectric tensor). In the rest of the chapter we will consider only monochromatic waves in order to have fixed values.

Starting from a Maxwell equation applied to a region of space which does not contain currents it is possible to obtain the following relation:

$$\mathbf{D} = \frac{n^2}{\mu}[\mathbf{E} - \mathbf{s}(\mathbf{s} \cdot \mathbf{E})] = \frac{n^2}{\mu}\mathbf{E}_\perp \tag{3.5.6}$$

Where $\mathbf{E}_\perp$ is the **E** component perpendicular to **s**, the direction of the unit wave normal and **t** is the unit vector in the direction of the ray vector **S**. It shows that in a crystal the energy is not in general propagated in the direction of the wave normal. Moreover **E**, **D** and **s** must be coplanar and orthogonal to **H** and **B** as shown in Figure 3.3.

Applying this result to Equation 3.5.5 we obtain for each component

$$\mu\epsilon_k E_k = n^2[E_k - s_k(\mathbf{E} \cdot \mathbf{s})], \qquad (\text{k = x, y, z}) \tag{3.5.7}$$

These are three homogeneous linear equations in E_x, E_y, E_z, that can be satisfied by non-zero values of these components only if the associated determinant vanishes. This implies that a certain relation must be satisfied by the refractive index n, the vector **s** and principal dielectric constants. This relation can be derived by writing Equation 3.5.7 in the form

$$E_k = \frac{n^2 s_k(\mathbf{E} \cdot \mathbf{s})}{n^2 - \mu\epsilon_k} \tag{3.5.8}$$

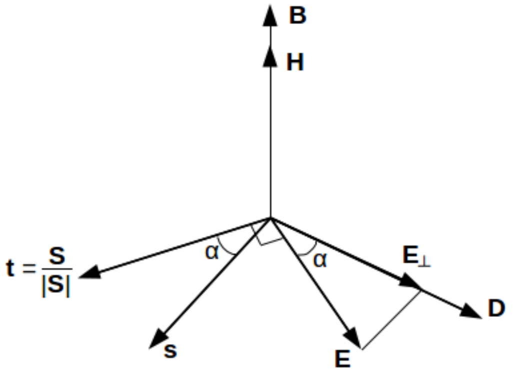

Figure 3.3: Scheme of the displacement of the wave normal, of the field vectors and of the energy in an electrically anisotropic medium.

Adding the three components with the suitable modifications it is possible to obtain the formula:

$$\frac{s_x^2}{(\frac{1}{n^2}+\frac{1}{\mu\epsilon_x})}+\frac{s_y^2}{(\frac{1}{n^2}+\frac{1}{\mu\epsilon_y})}+\frac{s_z^2}{(\frac{1}{n^2}+\frac{1}{\mu\epsilon_z})}=0 \tag{3.5.9}$$

and introducing the phase velocity v_p (the velocity of the wave in the direction of the wave normal)

$$\frac{s_x^2}{v_p^2-v_x^2}+\frac{s_y^2}{v_p^2-v_y^2}+\frac{s_z^2}{v_p^2-v_z^2}=0 \tag{3.5.10}$$

using:

$$v_x=\frac{c}{\sqrt{\mu\epsilon_x}}, \qquad v_y=\frac{c}{\sqrt{\mu\epsilon_y}} \qquad v_z=\frac{c}{\sqrt{\mu\epsilon_z}} \tag{3.5.11}$$

This is a quadratic equation in v_p^2 as can be seen by multiplying Equation 3.5.10 by the product of the denominators. Thus for every direction **s** there are two phase velocities v_p. The two values $\pm v_p$ corresponding to a value v_p^2 are counted as one since the negative value evidently belongs to the opposite direction of propagation -**s**. We have the important result that the structure of an anisotropic medium permits two monochromatic plane waves with two different linear polarizations and two different velocities to propagate in any given direction. From Equation 3.5.5 we have:

$$\frac{D_x^2}{\epsilon_x}+\frac{D_y^2}{\epsilon_y}+\frac{D_z^2}{\epsilon_z}=8\pi w_e \qquad or \qquad \frac{x^2}{\epsilon_x}+\frac{y^2}{\epsilon_y}+\frac{z^2}{\epsilon_z}=1 \tag{3.5.12}$$

if we use x, y and z in place of $D_x/\sqrt{C}$, $D_y/\sqrt{C}$ and $D_z/\sqrt{C}$. This equation represent an ellipsoid, the semi-axes of which are equal to the square roots of the principal dielectric constants and coincide in directions with the principal dielectric

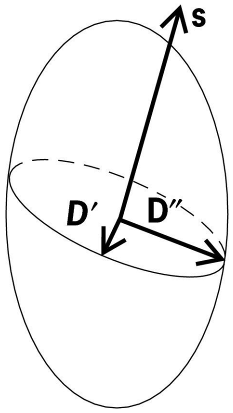

Figure 3.4: The ellipsoid of the wave normals. Construction of the directions of vibrations of the **D** vectors belonging to a wave normal **s**.

axes. We call this ellipsoid of wave normal (see Figure 3.4) and it can be used to find both phase velocities v_p. We draw a plane through the origin at right angles to **s**. The curve of intersection of this plane with the ellipsoid is an ellipse; the principal semi-axes of this ellipse are proportional to the reciprocals $1/v_p$ of the phase velocities and their directions coincide with the corresponding directions of vibrations of the vector D. Trying to determine the two semi-axes of the ellipse we find again

$$\mu D_k = n^2[E_k - s_k(\mathbf{E} \cdot \mathbf{s})] \qquad (\mathrm{k = x,\ y,\ z}) \tag{3.5.13}$$

Thus we find that the roots of the determinantal equation for $n = c/v_p$ are proportional to the lengths r of the semi-axes of the elliptical section at right angles to **s**, and, moreover, that the possible directions of the vector **D** coincide with the directions of these axes. Since the axes of an ellipse are perpendicular to each other, we obtain the important result that the directions of vibrations of the two vectors **D** corresponding to a given direction of propagation **s** are perpendicular to each other and **s**, **D'** and **D"** form an orthogonal triplet.

It is known that an ellipsoid has two circular sections C_1 and C_2 passing through the center and that the normals N_1 and N_2 to these sections are coplanar with the longest and shortest principal axes (z and x) of the ellipsoid. These two directions N_1 and N_2 are called the optic axes and along them there is only one velocity of propagation: **D** can then take any direction perpendicular to **s**.

3.5.2 Optical classification

A classification based on optical properties can be applied to crystals:

- group 1: Crystals in which three crystallographically-equivalent, mutually-orthogonal directions may be chosen. The crystal is optically isotropic and $\epsilon_x = \epsilon_y = \epsilon_z$;

- group 2: Crystals not belonging to group 1 in which two or more crystallographically-equivalent directions may be chosen in one plane. One dielectric principal axis must coincide with this distinguished direction. Crystals are said to be optically uniaxial and $\epsilon_x = \epsilon_y \neq \epsilon_z$;

- group 3: Crystals in which two crystallographically-equivalent directions can not be chosen. Here $\epsilon_x \neq \epsilon_y \neq \epsilon_z$. Crystals of this group are said to be optically biaxial.

3.5.3 Light propagation in uniaxial crystals

If we place the optical axis in the z direction (i.e. $v_x = v_y$), Equation 3.5.10 becomes

$$\begin{aligned} (v_p^2 - v_o^2)[(v_p^2 - v_e^2)\sin\theta^2 + (v_p^2 - v_o^2)\cos\theta^2] = 0 \qquad &\mathit{with} \\ s_x^2 + s_y^2 = \sin\theta^2, \qquad s_z^2 = \cos\theta^2 & \end{aligned} \tag{3.5.14}$$

θ is the angle between the z axis and wave normal s. The roots of this equation are given by:

$$\begin{cases} v_p'^2 = v_o^2 \\ v_p''^2 = v_o^2\cos\theta^2 + v_e^2\sin\theta^2 \end{cases} \tag{3.5.15}$$

It shows that both shells of the normal surface are a sphere of radius $v_p' = v_o$ and a surface of revolution, an ovaloid. Thus one of the two waves that correspond to any particular wave-normal direction is an ordinary wave with a velocity depending on the angle between the direction of the wave normal and the optic axis. The two velocities are only equal when $\theta = 0$, i.e. when the wave normal is in the direction of the optic axis. The vector **D** of the ordinary wave (**D'** in Figure 3.4) vibrates at right angles to the principal plane, the vector of the extraordinary wave (**D"**) is in this plane.

Now consider a plane wave incident from vacuum on a plane surface Σ of an anisotropic medium. It will give rise to a transmitted and a reflected field. Let **s** be the unit wave normal of the incident wave and **s'** that of the transmitted wave. The continuity of the field across the boundary demands that for any point r on the plane Σ and for all times t,

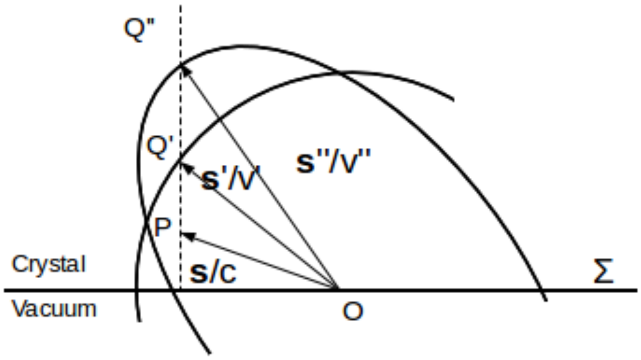

Figure 3.5: Double refraction: construction for permissible wave normals.

$$\begin{aligned} t - \frac{\mathbf{r}\cdot\mathbf{s}}{c} &= t - \frac{\mathbf{r}\cdot\mathbf{s'}}{v'} \\ \mathbf{r}\cdot(\frac{\mathbf{s'}}{v'} - \frac{\mathbf{s}}{c}) &= 0 \end{aligned} \tag{3.5.16}$$

hence the vectors $\mathbf{s'}/v' - \mathbf{s}/c$ must be perpendicular to the boundary. In Figure 3.5 it is possible to see that this request is obtained if **s’**/v’ end point Q’ must be on the normal to Σ through the end point P of the vector **s**/c. In general the normal to Σ cuts the inverse surface in four points, two of which lie on the same side of the boundary as the crystal. Hence there are two such points and therefore two possible wave-normals directions so that in general each incident wave will give rise to two refracted waves. This is the phenomenon of birefringence or double refraction. Calcite is a good example of this optical effect. The two refracted rays lie in the plane of incidence.

$$\frac{\sin\theta_i}{\sin\theta_t'} = \frac{c}{v'} \qquad \frac{\sin\theta_i}{\sin\theta_t''} = \frac{c}{v''} \tag{3.5.17}$$

Where θ_i, θ_t' and θ_t'' are the angles which the incident and the two transmitted waves make with the axis. Each of the transmitted waves obeys the same law of refraction as in the case of isotropic media. However, the velocity v now depends on θ_t, so that the determination of the direction of propagation in the crystal is more complicated. In a uniaxial crystal one sheet of the inverse wave-normal surface is a sphere, so that the phase velocity of one the transmitted waves is independent of θ_t, this being an ordinary wave. In the case of normal incident ($\theta_i = 0$) one has $\theta_t' = \theta_t'' = 0$ and both wave normals in the crystal coincide and are in the direction of the normal to Σ.

Chapter 4

MONTE CARLO SIMULATION SOFTWARE

4.1 Introduction: Monte Carlo simulations

Monte Carlo methods include a large number of computational algorithms that use the repeated extraction of random numbers to obtain numerical results. They are often used in physical and mathematical problems and generally speaking when the solution of a problem depends on a great number of variables. If their values or probability distributions are known, it is possible to weight the random extraction and fit the algorithm to the specific case. For instance, systems with many coupled degrees of freedom are fluids, strongly coupled solids, particles interactions physics and cellular structures. Probably the best example to mention goes back to 1946 when physicists at Los Alamos Scientific Laboratory were working on radiation shielding for neutrons. One of the people of the collaboration was Stanislaw Ulam who had the idea to solve this problem applying the Monte Carlo Method. From his memories:

"The first thoughts and attempts I made to practice were suggested by a question which occurred to me in 1946 as I was convalescing from an illness and playing solitaires. The question was what are the chances that a Canfield solitaire laid out with 52 cards will come out successfully? After spending a lot of time trying to estimate them by pure combinatorial calculations, I wondered whether a more practical method than "abstract thinking" might not be to lay it out say one hundred times and simply observe and count the number of successful plays. This was already possible to envisage with the beginning of the new era of fast computers, and I immediately thought of problems of neutron diffusion and other questions of mathematical physics, and more generally how to change processes described by certain differential equations into an equivalent form interpretable as a succession of random operations. Later I described the idea to John von Neumann, and we began to plan actual calculations.” [19]

This project required a code name since it was secret and Von Neumann chose the name Monte Carlo referring to the Monte Carlo Casino in Monaco where Ulam’s uncle would borrow money to gamble [20].

The Monte Carlo simulations are a powerful instrument to obtain information about complex systems but their are possible only with the support of a computing tools. Generally a simulation requires the description of the environment and the material, the starting conditions, physics laws, probability density functions of the physics process involved. All these elements can be inserted with more or less details but the computational power needed can grow very fast if too many variables are introduced. Only the developing of faster and faster computers and of grid computing has allowed the diffusion of Monte Carlo simulations.

Some of the modern particles physics experiments require an incredible effort in time and funds to be completed. The choice of materials, geometries and energies involved become crucial for the final apparatus response and it’s really hard to do modifications while the building is in progress or the experiment is already operative, at least without further costs. Monte Carlo simulations become essential in this sector, thanks to their ability to predict particles behaviour under defined conditions and they are greatly used during experiment design phase or during their upgrades. These software are used also during operative phase because the physics models applied in the algorithms have to be compared with the new results collected by the devices.

Several software were created to handle Monte Carlo simulations in particles physics and to extract all the information required by the final users. Some software are developed for specific physics like neutrons, high energies or optics, others are more generic and they include as more models as possible. Physics Monte Carlo simulations can be applied also with smaller devices as in SPECT and PET medical imaging where particles interaction with matter is fundamental for the quality of the images (see Section 2.1). ClearPEM is an example where the design phase of the scanner have been supported by simulations response. EndoTOFPET-US collaboration has decided to apply the same method for the development of the scanner but it required first to run tests in order to decide which simulation software to be used. Two software were chosen to be tested:

- *SLitrani*: very specific software to handle optical photons production and ray tracing. It was considered because of the physics behind scintillation crystals used in PET scanners;

- *Geant4*: a software developed for the simulation of several models from high energy physics to optical photons. Widely used in physics community.

A part of this Thesis work was to compare SLitrani (**SL**) and Geant4 (**G4**) using from simple to advanced simulations and to understand from their results how to use them in the frame of EndoTOFPET-US collaboration.

4.2 Geant4

GEANT4 is a software to simulate the interaction of particles with matter. It is written in C++ with an object oriented structured. The physics models it uses are very exhaustive and they cover all kind of processes as electromagnetic, hadronic or optical processes. It is possible to simulate a large set of particles with energies from few eV to TeV while materials, volumes and geometries can be well described to reproduce the experimental set-up in a very realistic way. From an interactive point of view, it is possible to extract all kind of parameters regarding the life of a particle during a simulation and simulating a large number of interactions it is possible to obtain a statistic of particles behaviour under the conditions simulated [21].

There are some limitations in this software since in some cases the models are not able to cover all the wide range of energies and the libraries where the physics parameters values are stored are not complete or the level of precision is not really accurate. Behind this project a large community of developers and users keeps working, correcting and upgrading the software. The first production release was finished in 1998 while in 1999 a Geant4 Collaboration was established. A complete manual of Geant4 can be found on its main site [22] while in this work a more detailed description will be provided only for some specific processes.

4.3 SLitrani

SLitrani is a simulation software dedicated to optical photons [23] . It was developed for set-ups used in high-energy experiments and in particular in CMS. It is able to follow the production, emission, propagation and detection of particles inside volumes and geometries reproducible with ROOT libraries [24]. Focusing on light ray tracing it includes managing of anisotropic materials, a feature that some scintillator crystals show. Also surface treatments, wrapping and boundary processes are taken into consideration and developed with particular attention. A graphical interface is used to show results by mean of ROOT histograms providing different information about photons generated and those that have reached detectors. Initially developed by F.X. Gentit, it has found other developers and several users around the world as it was uploaded on the web [25]. One of the limits of this software is that the specificity in optics is not well balanced in others physics models where imprecisions are encountered.

4.4 Physics behind software

In this work it was studied with particular attention how the simulators manage all the processes regarding optical photons and ray tracing in scintillator crystals. In the following sections I will briefly explain the methods used by G4 and SL to simulate these processes to better understand the simulations results that will be shown in the following chapter.

Absorption length

When the user want to simulate the presence of a volume, for instance the scintillator crystal, both G4 and SL require that a material must be characterized and linked to the volume itself. In this way the software is able to apply the physical properties of the medium to the particles interacting with it. The parameter related to the absorption probability is one of those to be defined. Its value is strictly related to the wave length of the photon crossing the medium and both codes require couples of values *absorption length-wave length* to simulate this dependency. If a photons with none of the length inserted is generated, the software interpolates the data in order to obtain the missing absorption value.

Boundary processes

The electric signal that can be created by a scintillator crystal used as particles detector depends on the number of optical photons that can be gathered from an edge of the crystal itself (Section 2.1.5). In turn this number is strictly connected to the crystal surface treatment. In fact crystal surfaces can be polished, depolished or covered with reflecting materials to change the probability that a photon is refracted outside the crystal and then lost. Both G4 and SL have a dedicated library to manage processes that happen at the volumes boundary. Using these functions it was possible to simulate different kinds of crystal surfaces, schematically represented in Figure 4.1:

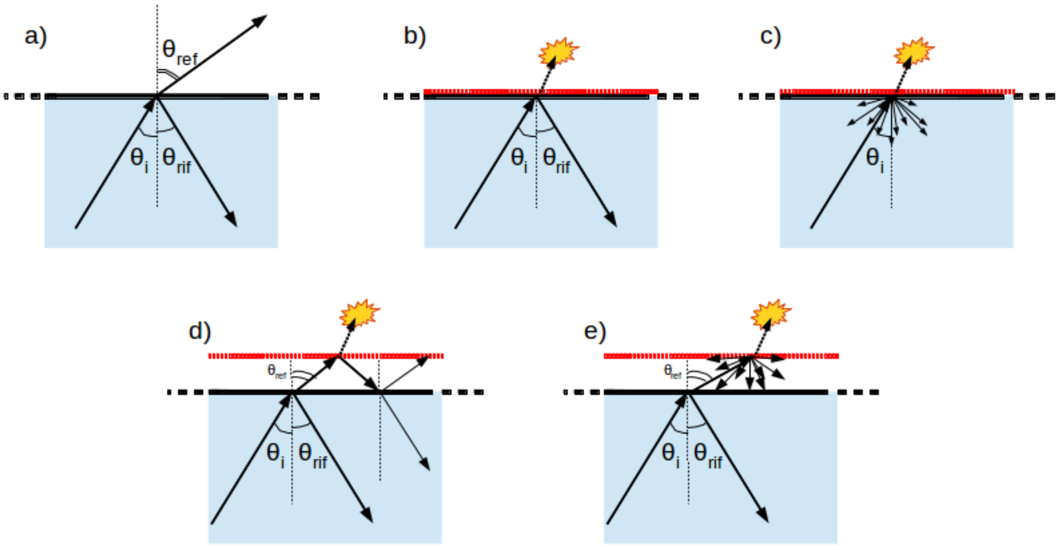

Figure 4.1: Surface treatments simulated. a) polished crystal, b) polished crystal with specular coating, c) polished crystal with diffusive coating, d) polished crystal with specular wrapping and e) polished crystal with diffusive wrapping.

- polished crystal;
- polished crystal with specular coating;
- polished crystal with diffusive coating;
- polished crystal with specular wrapping;
- polished crystal with diffusive wrapping.

G4 and SL behave almost in the same way regarding these surfaces. A polished crystal is intended as a crystal without any surface treatment where the Fresnel Law is applied to the photon reaching the surface in order to calculate the probability to be reflected or refracted. Then by the Snell Law the new angle is calculated. The refraction indices of the two media are involved in both formulas. The reflection for polished surfaces is considered as completely specular. Two different treatments can be apply to the crystal surfaces: coating and wrapping and in both cases it is possible to activate a specular reflection or a diffusive one obtaining four combinations. For coating is intended a layer of a particular material in contact with the crystal like a sort of paint, completely opaque to light but with an own refraction index (composed by a real and an imaginary part). A photon reaching the border can be reflected or absorbed with a probability depending on the incidence angle and on the indices of the crystal and coating. This could bring to a more efficiently photon collection because less photons are lost leaving the scintillator medium. Wrapping is a similar treatment but a very thin layer of air is present between the crystal and the material added to the surface. A photon reaching an edge of the crystal finds a polished surface and the two above formula are applied. Crystal and air refraction indices are used. If the photon is refracted, it finds the wrapping medium and the same procedure as the coated surface is applied but air refraction index must be used. Wrapping maximizes the probability for a photon to encounter a total reflection on the crystal surface and if refraction happens a further probability to be bumped in the crystal again is present.

Surface depolishing

Geant4 and SLitrani can simulate depolishing on crystal but while G4 is able to be coupled with wrapping and coating, for SL only the first treatment is possible. In polished crystals each side has a unique normal surface. On the other hand for depolishing treatment a new normal is calculated for each photon reaching the surface as if it hit a facelet. The new normal angle is obtained by a random extraction, based on a probability density function depending on the software used:

- in SLitrani the normal to the surface at the point hit by the photon is randomly tilted (with respect to the true normal of the surface) by an angle θ. It is generated randomly according to a distribution $sin(\theta)d\theta d\phi$, between 0 and a value of theta depending on the user;
- Geant4 assumes that the probability of micro-facet normals populating the annulus of solid angle $sin(a)da$ will be proportional to a Gaussian with a standard deviation defined by the user.

When the new normal is obtained, the incident angle is calculated with all the consequences on the related formula (Snell + Fresnel Law).

Anisotropy in crystals

SLitrani is able to simulate anisotropic materials unlike Geant4. In order to configure anisotropic crystals the software requires a more complex description of the medium: the refraction index has to be replaced by a dielectric tensor, as the one reported in Eq. 3.5.1. In the reference system of the *three optical axis*, it is represented by a diagonal matrix and only three values are required. Also absorption length is now described by three parameters, each one referring to one optical axis. Eventually a rotation matrix is required to couple the *World Coordinate System*, the coordinate system of the TOP volume, to the *system of the 3 optical axis.* If an uniaxial crystal has to be simulated, only two dielectric values and two absorption lengths are needed. They depend on the photon wavelength so a $f(\lambda_{ph})$ or $f(E_{ph})$ is required for each value.

Chapter 5

LIGHT TRACING: SIMULATIONS AND MEASUREMENTS

This work started analysing simple cases of photon tracing in crystals in order to check the agreement between different simulation software. For these tests, photons source are placed inside volumes made of uniform and isotropic medium where few physics processes are activated. The possible processes allowed for optical photons were the propagation, the absorption and the interaction with one of the crystal surfaces. The Student's t-test was used to check the compatibility of SLitrani (SL) and Geant4 (G4).

5.1 Absorption length

The absorption by a material was tested by placing a optical photons beam source with fixed energy inside a LSO volume big enough to absorb all emitted photons. The distance covered by each photon before absorption was registered and inserted in a histogram. Fitting the histogram with an exponential function I obtained the absorption length. Simulation were run 20 times and applied a Student's t-test to the results in order to check compatibility between SL and G4. This procedure was applied with different absorption lengths and different photon energies, even with those not directly coupled with an absorption value, obtaining a perfect agreement as shown in the Histogram 5.1. Table (5.1) and the ones of this chapter reports the *p-value* calculated from the Student's t-test and a column with probability level for which the discrepancy between the two results is only due to statistical variation .

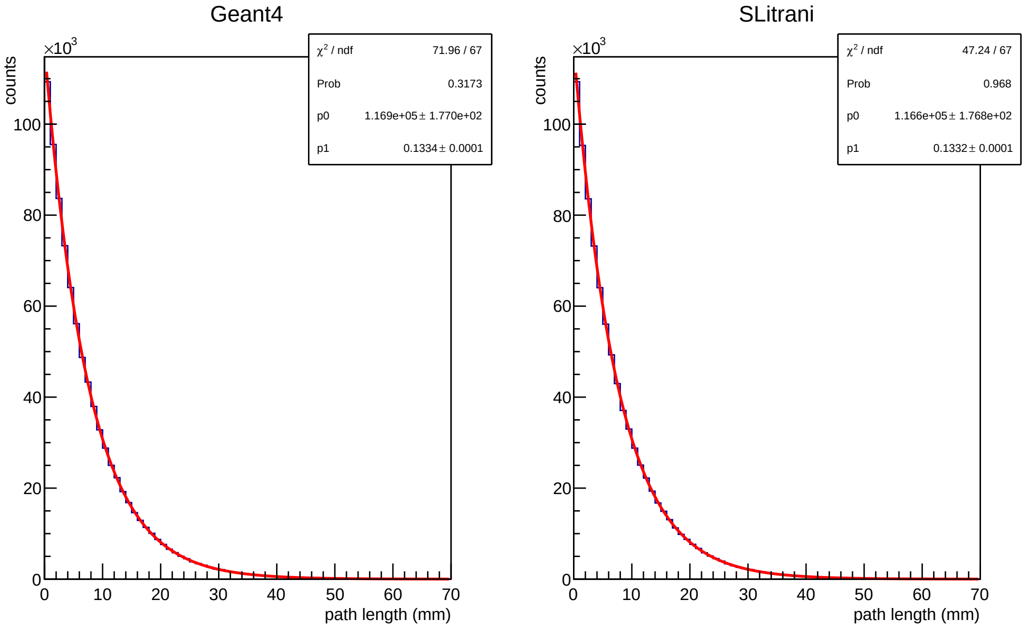

Figure 5.1: Example of one of the 20 histograms obtained collecting the lengths travelled by photons in a LSO crystal. An exponential fit was applied. Geant4 simulation on the left and SLitrani simulation on the right.

Abs. Length (mm)	**Energy (eV)**	**p-value**	**Prob.**
138	2.95	0.354	$p < 1$
120	1.84	0.335	$p < 1$
75.0	3.59	0.784	$p < 0.5$

Table 5.1: Student's t-test results applying different absorption lengths-energies couples for the LSO crystal.

Treatment	p-value	Prob.
polished crystal	0.857	$p < 0.5$
specular coating	0.813	$p < 0.5$
specular wrapping	0.883	$p < 0.4$
diffusive coating	5.381	$p < 0.001$
diffusive wrapping	2.873	$p < 0.01$

Table 5.2: Student's t-test results and significance level obtained applying different surface treatments to the boundary surface LSO-air.

5.2 Boundary interaction

G4 and SL compatibility on surface treatment was checked using a simple simulation. The configuration was composed by a monochromatic point source inserted in a volume of LSO. Optical photons were generated not isotropically but directed with a specific angle towards one of its surfaces. As explained in Section 4.4, different crystal surfaces treatments can be applied:

- polished crystal;
- polished crystal with specular coating;
- polished crystal with diffusive coating;
- polished crystal with specular wrapping;
- polished crystal with diffusive wrapping.

These treatments were sequentially simulated and the source was rotated to test dependency on the incident angle. Photons not absorbed before reaching the surface could be either reflected back inside the crystal, refracted (naked polished crystal) or absorbed by the surface material (other four cases). For each angle and each treatment a group of photons was emitted and the ratio between the reflected particles and the ones reaching the surface before boundary interaction was registered. This process was repeated 20 times for both SL and G4 and an average value from each couple angle-treatment was obtained. Calculating the corresponding RMS, Student's t-test was computed. Results of different angles but same surface treatment were averaged (plots in Figure 5.2, 5.3 and 5.4) and a compatibility single value was obtained as shown in Table 5.2.

The results show a good compatibility between the simulations for every kind of surface except for the ones with a diffusive coating and wrapping. The reason is a different software approach to this kind of surface:

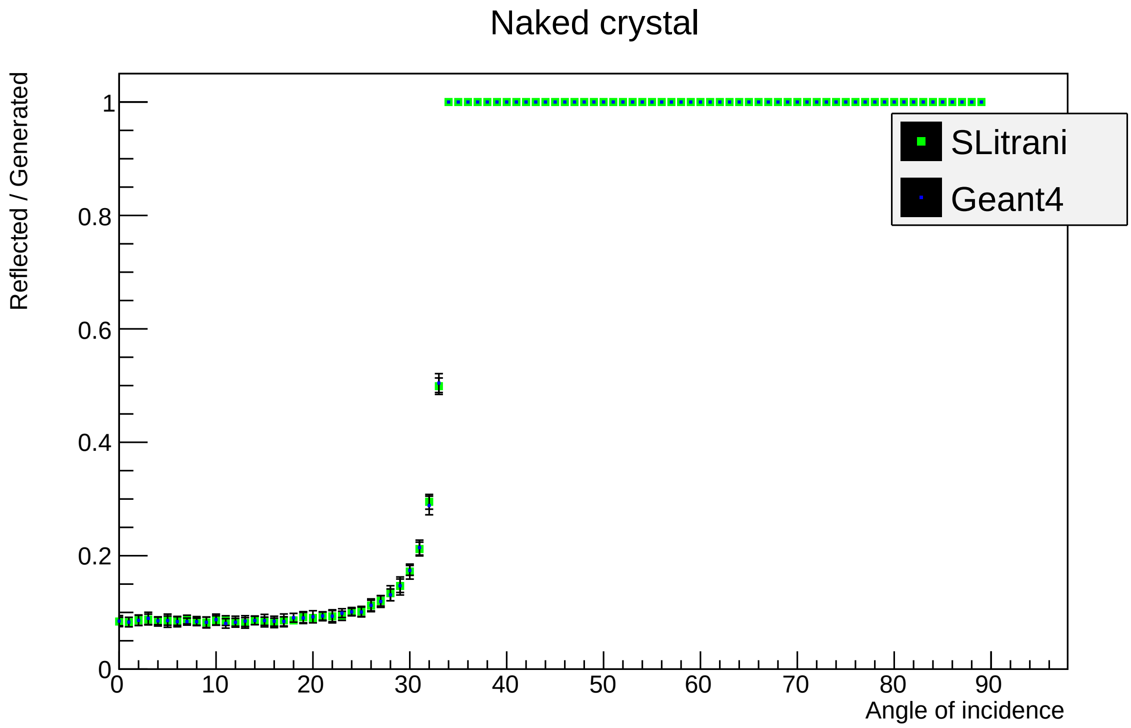

Figure 5.2: Reflectivity comparison between G4 and SL with polished crystals.

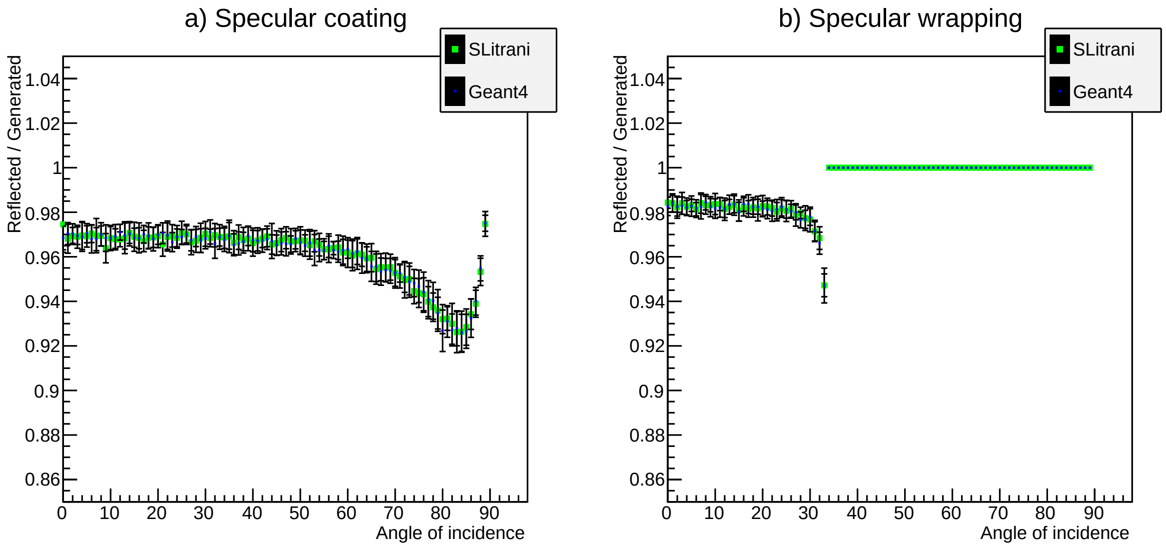

Figure 5.3: Reflectivity comparison between G4 and SL applying a specular coating (a) and a specular wrapping (b) on polished crystals.

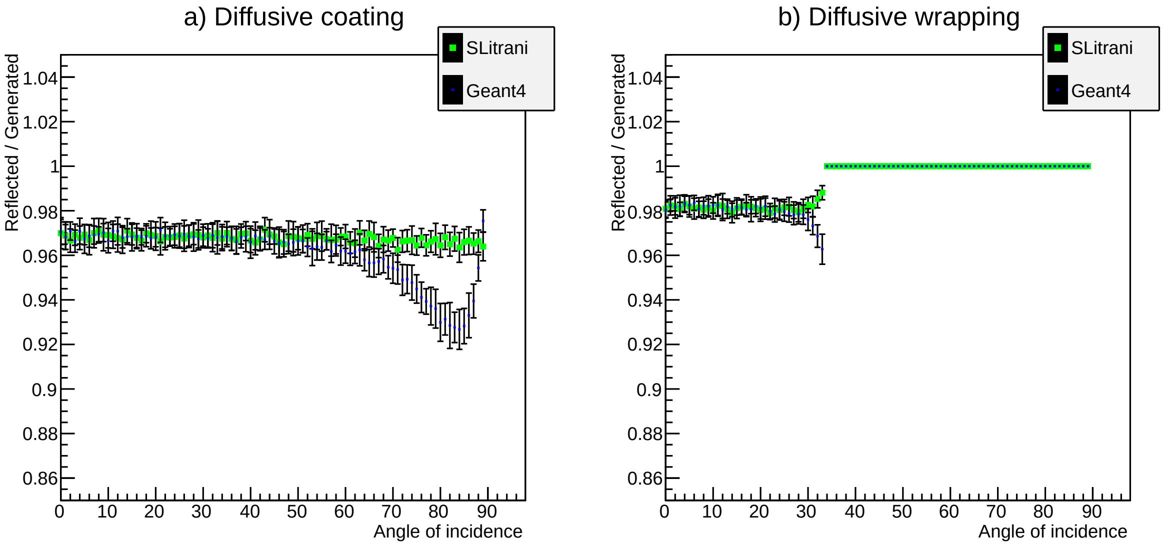

Figure 5.4: Reflectivity comparison between G4 and SL applying a diffusive coating (a) and a diffusive wrapping (b) on polished crystals.

- in Geant4 reflectivity on a surface is calculated considering the incident angle of the photon on the plain surface, then, if reflection happens, a new angle is extracted randomly from an isotropic distribution;

- in SLitrani when the photon reaches the diffusive surface a new normal is extracted from a probability distribution, as if the surface was composed by micro-facelets with different orientations. The incident angle is re-calculated on this new surface and the reflectivity formula is applied. If reflection takes place the photon is scattered with a reflection angle specular to the new incident angle. The distribution used for the calculation of the facelet normal has a supplementary factor $\cos(\theta)$ with respect to a totally isotropic distribution $\sin(\theta)\mathrm{d}\theta\mathrm{d}\sigma$ in order to slightly favour the direction normal to the original diffusing surface.

This difference can be seen in Geant4 results in Plots 5.3.a and 5.4.a. They are similar since absorption probability is calculated before the tilting of the normal to the surface. In this way photons with same incident direction have a same reflectivity value and, only after this test, they are reflected with different angles. On the contrary SLitrani shows a different behaviour in Plot 5.3.a and 5.4.a. In this second plot at higher angles the extraction of a new surface normal shifts the incident angles to lower values where reflectivity is about 0.97 instead of values between 0.96 and 0.92 as it is possible to see in the last part of Plot 5.3.a.

Geant4 results are different between Plot 5.3.b and 5.4.b because of the different probability for an optical photon to leave the air layer after the reflection on the wrapping. In fact photons reaching the diffusive wrapping surface with small angles are averagely scattered with bigger angles. That means an higher probability to be reflected by the surface air-crystal instead to re-enter in the crystal. In this way a new reflectivity test is run and the probability to be absorbed increases. With a specular wrapping small incident angle on the external surface means small incident angle on the air-crystal layer and consequently an higher probability to enter in the crystal. In fact Geant4 Plot 5.3.b shows slighter reflectivity values at small angles than Plot 5.4.b. At the opposite, at bigger incident angles a photon reflected by a diffusive wrapping is reflected with smaller angles with an higher probability to leave the air layer then a specular wrapping. Looking at high angles in the results, Geant4 Plot 5.4.b shows higher reflectivity value then Plot 5.3.b.

5.3 Photon extraction efficiency

G4 and SL were tested also on photon extraction efficiency from scintillator crystals. This parameter shows the probability for an optical photon (generated randomly inside the bulk and with a random orientation) to escape from a chosen side of the crystal. The simulation is based on LSO crystals where five of the six sides can be modified with one of the previous surface configurations while the last one was left completely polished. Photons escaping from this surface were counted and extraction efficiency was obtained normalizing to the number of total photons generated.

For each surface treatment different crystal dimensions were simulated (details in Table 5.3). In order to test the software compatibility the same statistical approach as before was taken. That means:

- for both SL and G4, 20 simulations were run for each crystal dimension and for each surface treatment and 20 extraction efficiency values were obtained;
- values belonging to the same combination were averaged and RMS was calculated;
- Student's t-test was applied to each configuration pair and averaged with the values obtained from different crystal dimensions but same surface treatment.

At the end of this procedure, five compatibility values can be checked, one per surface treatment (see Table 5.4). In Plots 5.5, 5.6 and 5.7 values are reported following the numeration of Table 5.4.

	x (mm)	y (mm)	z (mm)
1	0.75	0.75	20.0
2	1.45	1.35	20.0
3	2.25	2.25	20.0
4	2.50	2.20	20.0
5	2.90	2.65	20.0
6	4.20	4.20	20.0
7	5.20	4.25	20.0
8	5.60	4.25	20.0
9	5.20	5.20	20.0
10	10.0	10.0	20.0
11	20.0	10.0	20.0
12	20.0	20.0	20.0
13	30.0	30.0	20.0
14	40.0	40.0	20.0

Table 5.3: Dimensions of crystals simulated for the light output comparison by SL and G4.

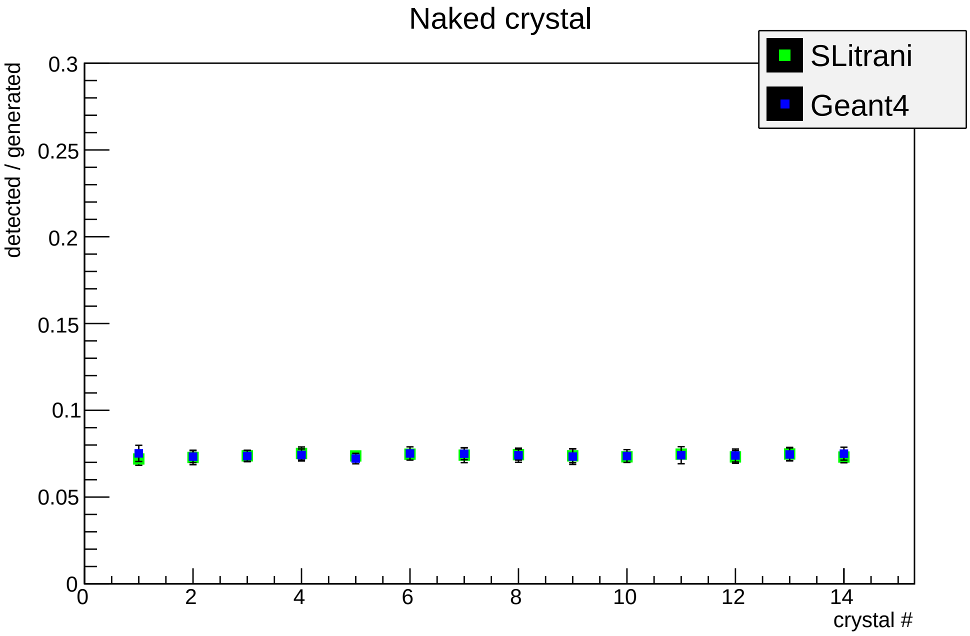

Figure 5.5: Light output comparison between G4 and SL with naked crystals of several dimensions. Photons are collected at the exit of the extraction surface.

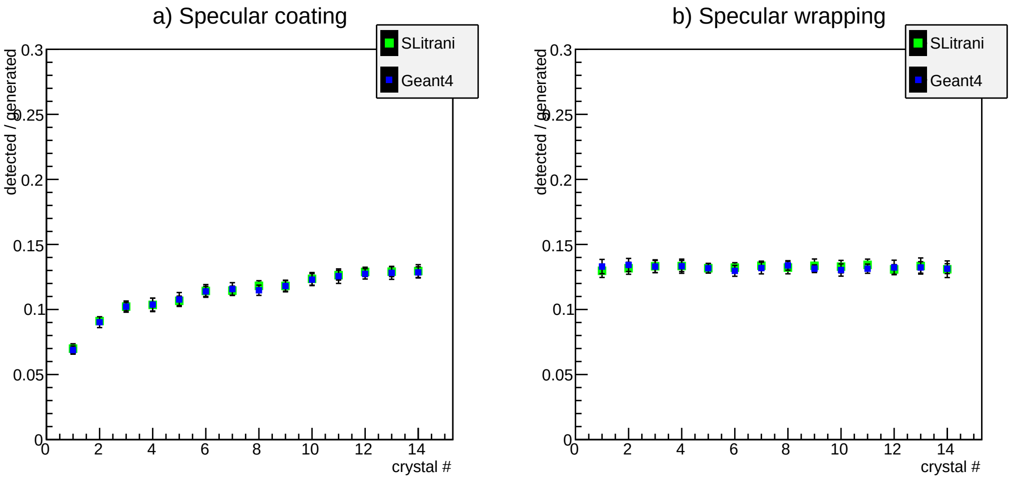

Figure 5.6: Light output comparison between G4 and SL applying a specular coating (a) and a specular wrapping (b) on polished crystals. Photons are collected at the exit of the extraction surface.

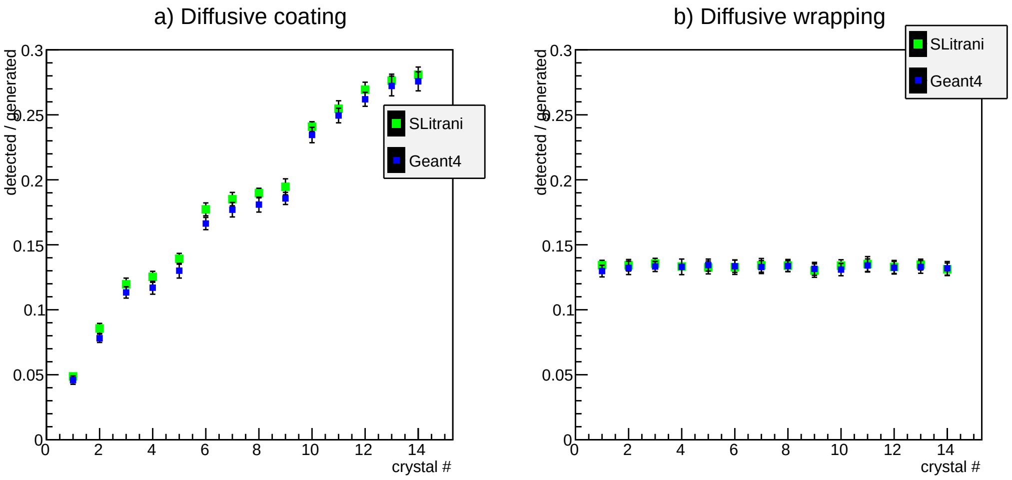

Figure 5.7: Light output comparison between G4 and SL applying a diffusive coating (a) and a diffusive wrapping (b) on polished crystals. Photons are collected at the exit of the extraction surface.

Treatment	p-value	Prob.
polished crystal	0.821	$p < 0.5$
specular coating	0.852	$p < 0.5$
specular wrapping	0.713	$p < 0.5$
diffusive coating	2.198	$p < 0.05$
diffusive wrapping	1.1135	$p < 0.3$

Table 5.4: Student's t-test results and significance level obtained applying different surface treatments to several crystal dimension. Photon are collected as soon as they cross the exiting surface.

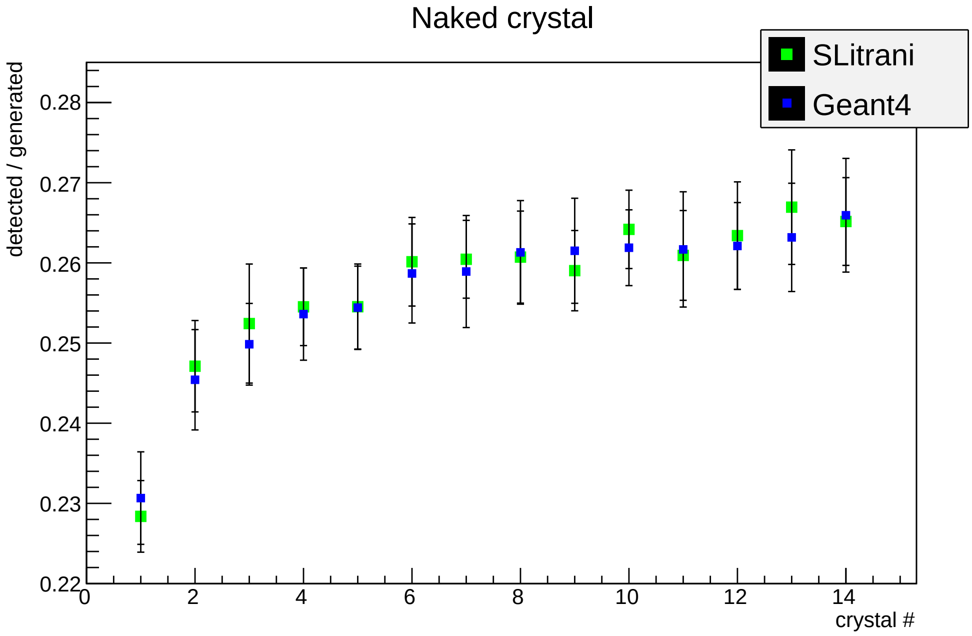

Figure 5.8: Light output comparison between G4 and SL with naked crystals of several dimensions. Photons are collected when they exit from the extraction surface, cross the coupling medium and reach the sensor volume.

If the simulated photon extraction efficiency has to be compared with values measured in lab, it is necessary to take into consideration that an optical photon exiting the crystal is not automatically counted by the photodetector. In fact it can bounce on the glassed lens of the instrument and moreover if a refraction takes place, a detection efficiency must be considered. Moreover in the experimental procedure, optical grease is applied to couple the crystal surface with the PMT lens. To simulate this configuration, a very thin volume was placed in front of the gathering side of the crystal. It was made by a fake material completely transparent to optical photons but with a refraction index similar to glass. A thin layer of grease was placed between the crystal and the photodetector using the same procedure of a transparent volume with grease refraction index. Only the ratio of the photons entering in the sensor volume (a refraction inside its volume has to take place) was evaluated as the extraction efficiency value. In this configuration a new comparison was made using the same statistical approach. Results are shown in Plots 5.8, 5.9 and 5.10.

SL and G4 show a difference in the photon extraction efficiency compared to the previous configuration, more evident in small crystals. On the contrary the comparison between SL and G4 shows the same results as the case without the detector: good matching for all the surface configurations except for polished crystal

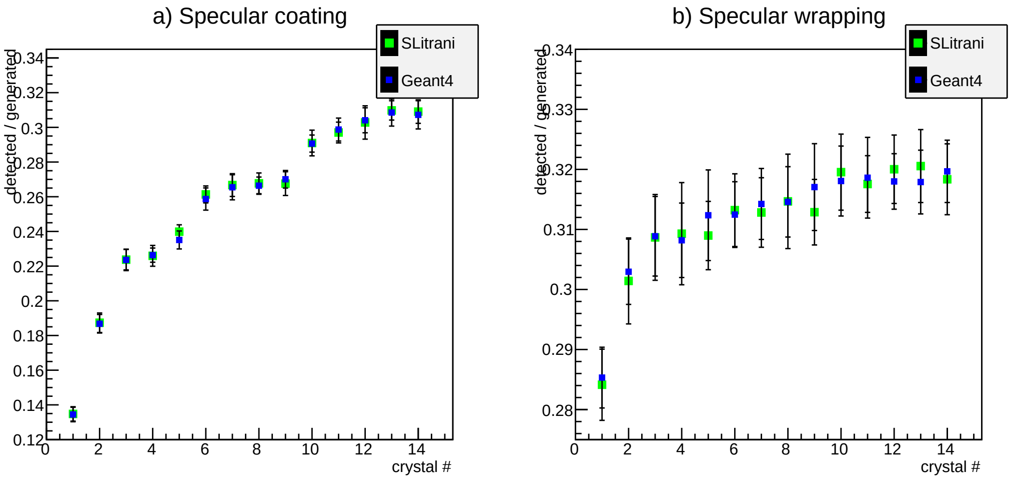

Figure 5.9: Light output comparison between G4 and SL applying a specular coating (a) and a specular wrapping (b) on polished crystals. Photons are collected when they exit from the extraction surface, cross the coupling medium and reach the sensor volume.

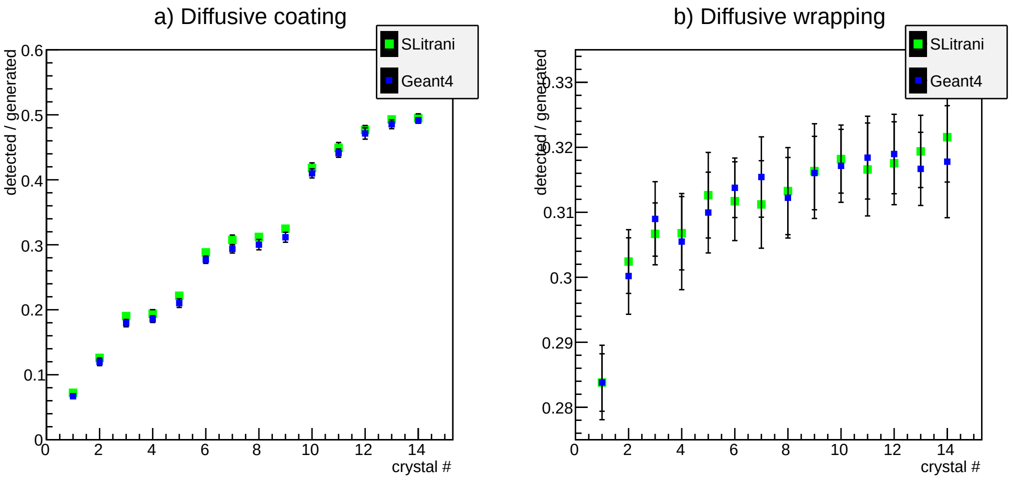

Figure 5.10: Light output comparison between G4 and SL applying a diffusive coating (a) and a diffusive wrapping (b) on polished crystals.Photons are collected when they exit from the extraction surface, cross the coupling medium and reach the sensor volume.

Treatment	**p-value**	**Prob.**
polished crystal	0.837	$p < 0.5$
specular coating	0.848	$p < 0.5$
specular wrapping	0.743	$p < 0.5$
diffusive coating	2.222	$p < 0.05$
diffusive wrapping	1.130	$p < 0.3$

Table 5.5: Student's t-test results and significance level obtained applying different surface treatments to several crystal dimension. A coupling medium and a sensor volume are placed in front of the extraction surface to collect exiting photons.

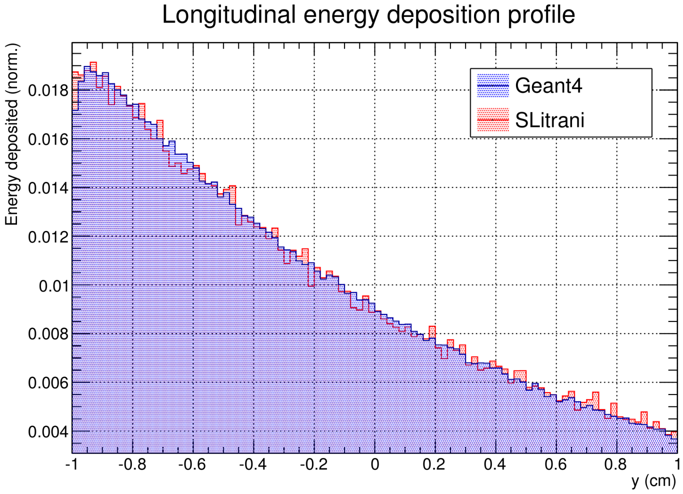

Figure 5.11: Energy deposition profile along a LSO crystal with a 511 keV source applied.

with diffusive coating.

5.4 Secondary particles emission

When the interaction of gamma particles with crystals is simulated, a more complex physics is involved. An example, we are interested in, is the interaction of a gamma with a crystal and the starting of the scintillation process. A gamma particle, with energy below pair production threshold, can lose its energy by Compton scatter and photoelectric effect creating electrons free to move in the crystal lattice. Their energy is lost partly in the scintillation processes where optical photons are generated. Geant4 is able to simulate all these processes from gammas to final optical photons using complex models. SLitrani on the other hand is not able to follow secondary particles and physics regarding gammas is reproduced with a simple model. To test these differences I have simulated a 511 keV gamma source aiming to a 2×2×20 mm^3 LSO crystal. Gamma energy deposition intensity and position was registered for both the software. The results, in Fig. 5.11, show the energy deposited as a function of the crystal length.

A perfect agreement is obtained between SL and G4. The situation is different on the transversal profile due to the lack of secondary particles emission in SLitrani as it is shown in Figure 5.12.

The main difference concerning the optical part is the production of Cerenkov photons by secondary charged particles. Simulating 511 keV gammas interacting with a LSO crystal where light yield is fixed to 50000 ph/MeV, it is possible to collect between 1000 and 10000 photons depending on the crystal surface treatment.

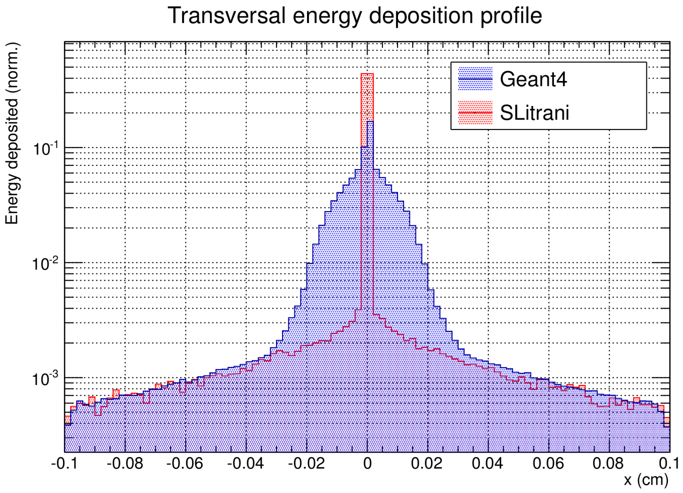

Figure 5.12: Trasversal energy deposition profile along a LSO crystal with a 511 keV source applied.

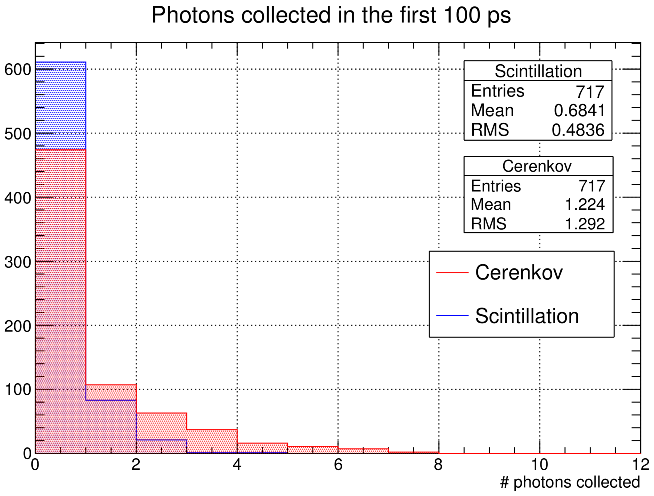

Figure 5.13: Number of optical photons collected in the first 100 ps after the gamma interaction with crystal.

Under this configuration secondary electrons simulated by Geant4 produce only few tens of Cerenkov photons and only few units are collected. Therefore from the quantity point of view they are irrelevant but if acquisition time is considered the situation is quite different. Cerenkov photons are produced promptly and in the first 100 ps they are more than scintillation photons. In timing application (for example when it is necessary to measure time of flight) their absence may bring to important differences. Figure 5.13 shows this comparison between Geant4 and SLitrani.

5.5 Anisotropic crystals

SLitrani is able to simulate anisotropic crystals, differently from Geant4. The anisotropy appears in some scintillator crystals used in physics experiments. For instance because of its high density and fast decay time, lead tungstate ($PbWO_4$) crystal was chosen by the CMS collaboration at the large hadronic collider (LHC) to construct the electromagnetic calorimeter ECAL. $PbWO_4$ shows a strong anisotropy and it can be a good candidate for the study of this feature. Unfortunately its light yield is very low compared to other crystals normally used in medical physics (as example 100 ph/MeV for lead tungstate vs 9000 in BGO or 32000 for LYSO crystals) [17]. This disadvantage is avoided because $PbWO_4$ is adopted in high energy physics experiment where the particles energy is several orders of magnitude bigger than radio-sources used in medical application.

To quantify the effect of anisotropy in a ray tracing simulation, $PbWO_4$ was chosen because its optical characteristics are well know in literature. Two configuration were prepared in SLitrani:

- with anisotropic features: the ordinary and extraordinary refraction indexes from [26] were applied to calculate the two values required to described the dielectric tensor (see Section 3.5.1) of a uniaxial negative crystal ($n_e < n_o$). Two values of the absorption length are provided;
- with isotropic features: values of the ordinary and extraordinary axes are used to calculate an average configuration.

Anisotropy can be simulated only in naked or wrapped crystals due to software issues. Table 5.5 shows a very good agreement between G4 and SL for this kind of configurations and, for our purposes, SLitrani results with isotropic configuration can be considered fully compatible with Geant4 ones. Anisotropy was tested in both configurations, on crystals of a 2x2 cm^2 section and a length from 1.9 to 1.4 cm (dimensions have been chosen based on LY measurement on $PbWO_4$ crystals of

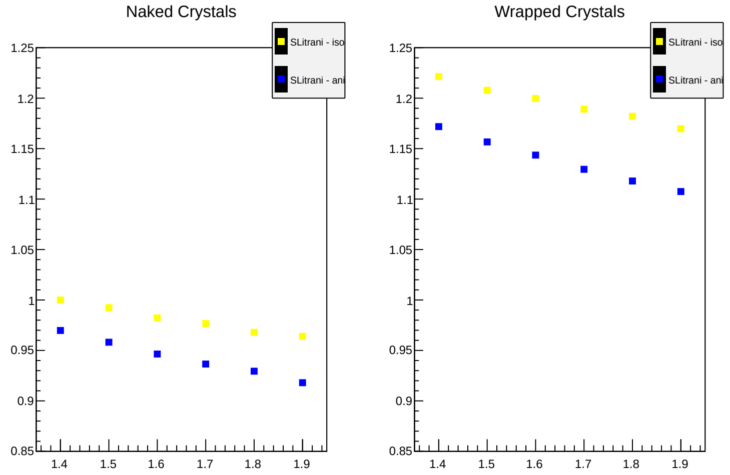

Figure 5.14: Photon extraction efficiency of $PbWO_4$ crystal in isotropic (yellow) and anisotropic (blue) configuration. Two test run: naked and wrapped crystal. Values are normalized to the first isotropic sample.

Section 5.6.3). Optical grease is simulated as coupling material between the crystal and the sensor lens. For this test a gamma source was placed outside the crystal instead of generating optical photons inside the scintillator volume.

Results are normalized on the value obtained with the isotropic naked 1.4 cm long crystal. Values show a difference of about 3-4% between isotropic and anisotropic configuration with naked crystal. It becomes a little higher with wrapped crystals but still less then 5%. Compared to common errors of real light yield measurements on scintillator crystals (see next section), this discrepancy is almost negligible and very difficult to detect. On the other hand, transmission and absorption measurements are more accurate and, if a simulated result is required, it could be necessary to activate anisotropy in crystals. For the kind of simulations we intend to run, this feature is not necessary. The minimal advantage in precision we obtain with anisotropy is completely overtaken by the lack of secondary particles that SLitrani is not able to simulate. This is not the only reason that will bring us to prefer G4 as simulation software for our collaboration, as it will be explained in Section 5.7.

5.6 Light yield measurements

5.6.1 Procedure

Light yield refers to the ability of a crystal to convert the energy released by a particle crossing the crystal bulk in a proportional number of optical photons (see Section 3.3). Even using particle of known energy and collecting all the photons exiting the

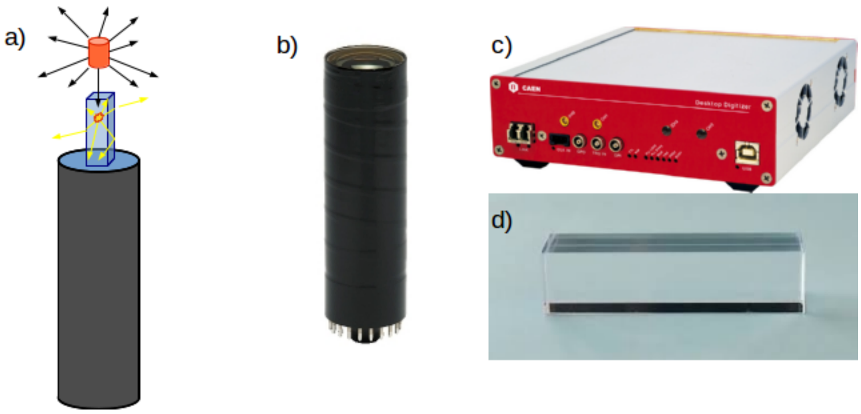

Figure 5.15: a) Scheme of the experimental set-up. b) R2095 Hamamatsu photomultiplier, c) DT5720A Caen analog digital converter and d) a LYSO crystal.

crystal, light yield is not easy to evaluate because of the competitive processes to scintillation that occur (Section 3.2) and the self-absorption inside the volume. The number of optical photons collected by the sensor will be lower then the real number of those produced. This is why the light yield value of a specific crystal (i.e.depending on material and volume dimension) is preferred to the intrinsic light yield value that depends only on the chemical composition. A light yield measurement was conducted at CERN, in the Crystal Clear Collaboration laboratories, on $PbWO_4$ and LYSO crystals. The equipment used for this measurement was composed of:

- Cesium-137 source with cylindrical shape (2 mm radius and 1 cm length);
- N-126 power supply of *CAEN* company;
- XP2020Q photomultiplier from *Photonis* for $PbWO_4$ measurements and R2059 from *Hamamatsu* for LYSO crystals;
- attenuator from 0 to 44.5 dB with impedance of 50 Ω;
- desktop digitizer DT5720A from *CAEN*.

The photomultiplier was placed vertically and each sample placed directly in contact with the lens on the extraction face chosen. In some cases, between the crystal and the glass, a layer of optical grease (refraction index 1.45) was applied to increase the coupling between the two materials and to obtain an higher extraction of photons. An holder was used to keep the source above the middle of the upper crystal side and at a distance of about 10 mm from it. The whole set-up was inserted in a black box to shield both crystal and phototube from external light.

To calculate the value of the light yield this formula was applied for each crystal after an acquisition long enough to acquire a good statistics for the discrimination of the photo peak:

$$LY = \frac{ch_{pp} \cdot Q_{bin} \cdot attenuation}{q_e \cdot G \cdot QE \cdot E_\gamma} \tag{5.6.1}$$

Where:

- ch_{pp}: ADC channel where photopeak mean value falls;
- Q_{bin}: Coulomb per bin conversion in the ADC histogram;
- $attenuation$: phototube output attenuation in use during the measurement;
- q_e: electron charge;
- G: PMT gain;
- QE: Quantum efficiency of the PMT (dependent on the crystal emission spectrum);
- E_γ: energy of the gamma crossing the crystal.

The parameter ch_{pp} was obtained from the spectra collected, Q_{bin} and $attenuation$ were properly set and fixed before a series of acquisitions while E_γ is known. The photomultiplier gain, on other hand, is more difficult to obtain. For the XP2020Q model, it was applied the reverse of Equation 5.6.1 with a crystal where the LY was already measured. For this specific task it was measured a reference 1×2×2 mm^3 LSO crystal and from the channel corresponding the photopeak mean value I have extracted the PMT gain. For model R2059 a reference measurements was not available and gain was calculated from the single electron measurements. An acquisition started just applying a cover to the PMT without any source or crystal. In this configuration the only visible signal is generated by those electrons that leave the photocathode by thermal agitation. It is extremely rare that two electrons are detected at the same time and moreover the gate window can be reduced to few nanosecond to avoid multiple counts. So the spectrum will show a peak created by the "detection" of single electrons and the mean value will be at:

$$ch_{pp} = \frac{1_e \cdot G \cdot q_e}{Q_{bin}} \tag{5.6.2}$$

from which it is possible to obtain the PMT gain since all other values are known.

It is important to consider that PMTs usually required a pre-heating time before reaching a stable running condition. Within this period, gain can drift. For instance,

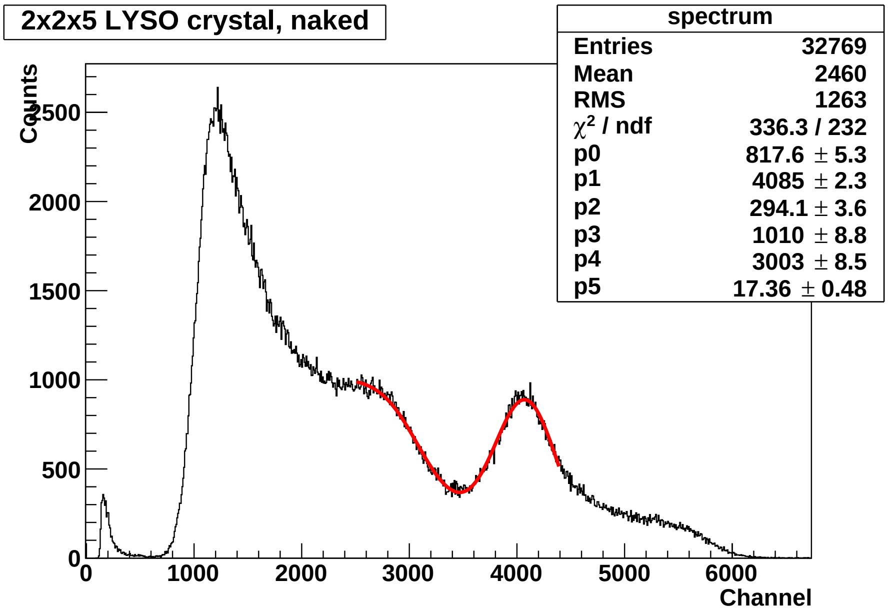

Figure 5.16: Spectrum obtained with a 300 sec. long acquisition of the light output of a 2×2×5 mm^3 LYSO crystal. The red line shows the fit applied to the photopeak and to the Compton edge.

the model used with $PbWO_4$ crystals was turned on and a 20 minutes long acquisition was run, divided in spectra of one minute step. With this method it was possible to follow the drifting of the photo peak mean position and, more important, evaluate when the photomultiplier would have reached a stable configuration. At this point a real measurement can begin, gain value can be calculated and applied to the previous formula. An example of the spectra obtained by this experimental setup can be see in Figure 5.16 from which the LY of a 2×2×5 mm^3 LYSO crystal was measured. The plot shows also the fit applied to find the photopeak value. The function chosen consists of a Gaussian curve for the photopeak and a Fermi function for the Compton edge to take into consideration the overlap of the two components:

$$y = a \cdot e^{(-(x-b)^2/(2\cdot c^2))} + d/\sqrt{1+(x/f)^g} \tag{5.6.3}$$

Before starting a light yield measurement it is necessary to tune the parameters of the acquisition system. In the DAQ system used in this campaign of measurements it was possible to set acquisition time gate, trigger threshold, gate offset, pre-trigger, coulomb per channel conversion. Values were chosen monitoring the acquisition response on the oscilloscope as it is possible to see in Figure 5.17. For example gate is chosen long enough to include the whole signal and usually a window ten times long the fast decay constant (see Section 3.3) is chosen. On the other hand, it can not be to long because multiple counts can be included in the same time window

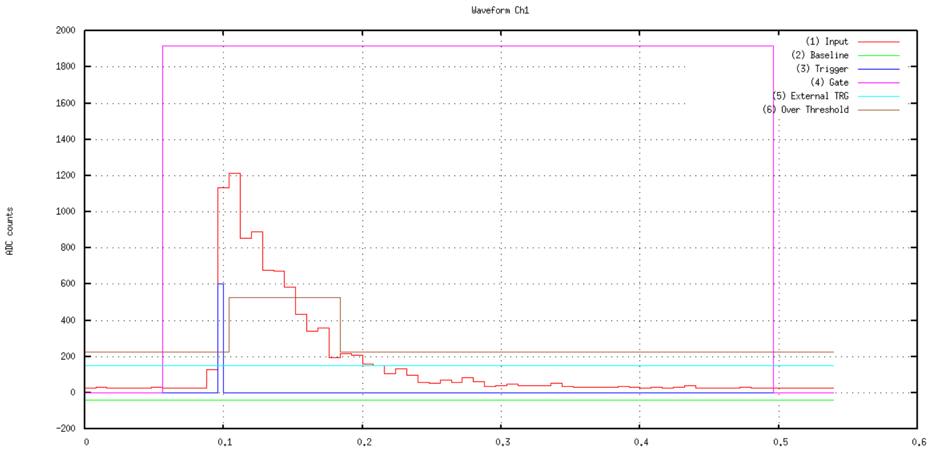

Figure 5.17: An example of a signal profile obtained during measurements of LYSO crystals.

and acquisition rate becomes lower and lower.

5.6.2 LYSO crystals

A first series of measurements was run in our laboratories on completely polished LYSO crystals. They consist of two sets of 2×2 mm^2 section and two with 3×3 mm^2 section with different lengths, from 5 to 30 mm with steps of 5 mm. These crystals have dimensions typical for PET devices and the LY measurements are really difficult on such small crystals in particular when surface treatments have to be applied. A 5% error on LY values has been estimated due to the PMT instability and to errors in the measuring procedure as bad coupling between extraction surface and PMT lens, small bubbles in the grease layer or light leaks in the wrapping. LY was measured with the method described in the previous paragraph using initially naked crystal.

First plot of Figure 5.18 shows the results obtained and reported in Table 5.6. A longer crystal has a bigger stopping power but optical photons have more probability to be absorbed or to leave the crystal by lateral or back sides before reaching the extraction surface. This effect is clearly visible in the plot where values are reported based on crystal length. Crystals, produced by Crystal Photonics, Inc., should have the same optical characteristics since they were cut starting from the same block. Results show that samples of the same dimensions (section and length) have a compatible LY. Also the difference between the 2×2 and 3×3 mm^2 sets are very small and they can be considered equals (even if longer crystals show a bigger discrepancy). A second set of measurement was acquired applying a wrapping made of Teflon on the 2×2 mm^2 section crystals. Four layers of Teflon were applied to all of the crystal

	2×2 mm^2	3×3 mm^2
Length (mm)	**LY (ph/MeV)**	**LY (ph/MeV)**
5	6803	6169
5	6741	6348
10	5382	5235
10	5319	5017
15	4575	4593
15	4598	4578
20	4207	4103
20	4182	4030
25	4250	3961
25	4252	3901
30	4051	3703
30	3986	3685

Table 5.6: LY values for the 2×2 mm^2 and 3×3 mm^2 series with naked crystals.

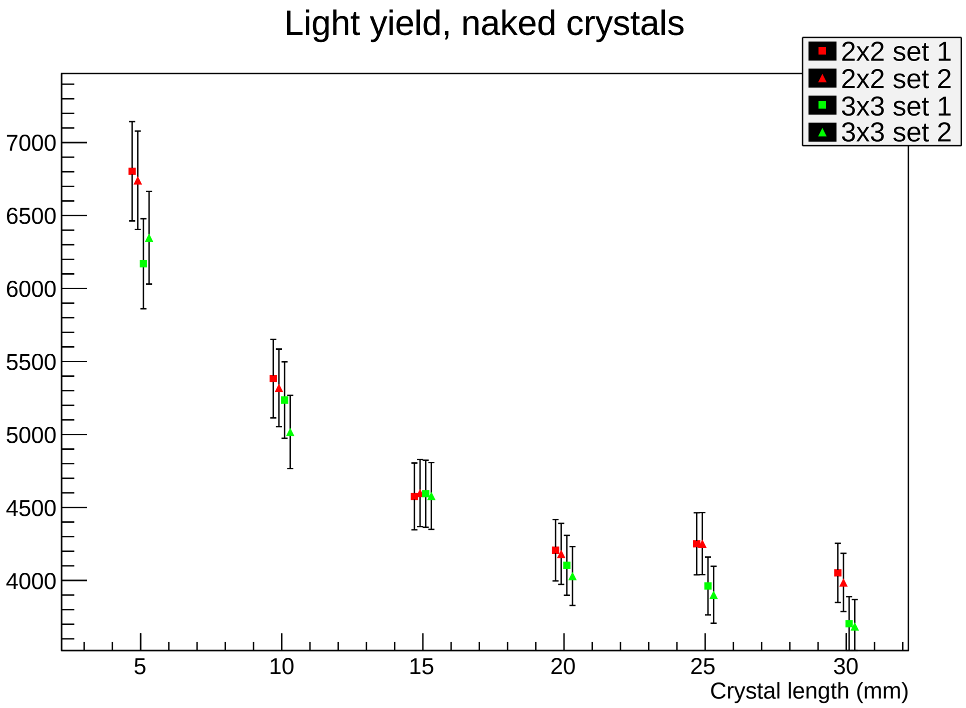

Figure 5.18: Plot of the LY values for the 2×2 mm^2 and 3×3 mm^2 series with naked crystals.

Length (mm)	**LY (ph/MeV)**
5	15334
5	13993
10	12742
10	11628
15	9016
15	9385
20	7792
20	9016
25	8889
25	8647
30	7455
30	7805

Table 5.7: LY values for the 2×2 mm^2 series with wrapped crystals by Teflon.

surfaces except for the extraction one. As explained, wrapping is able to increase final LY reducing the number of photons that exit from the lateral surfaces. Results are reported in Table 5.7 and shown in Plot 5.19.

Thanks to this method LY values have been increased of about 100% with respect to naked crystals. The wrapping procedure is not mechanized and some errors in the application of the Teflon on crystal surface could be introduced. This explain the increase of the spread between different crystals with the same size.

Finally a set of measurements was conducted applying optical grease (refraction index 1.45) to crystals. A small layer was inserted between the PMT lens and the extraction face of the crystal in order to improve the efficiency of the optical coupling and so the possibility for photons to leave LYSO. This procedure was repeated for all the crystals. Results are shown in Table 5.8 and Plot 5.20.

LY values show an increase of about 200% with respect to the naked crystals for all the sections and crystal lengths. A good compatibility is present between crystals of the same length. Grease is manually applied to crystals and also this procedure is affected to errors with the introduction of small bubbles and dis-uniformities.

I have tried to simulate these measurements applying the same geometry set-up used for the photon extraction efficiency, Section 5.3, but instead of generating optical photons in the crystals, a gamma source was applied. The source was placed outside the crystal with gammas directed perpendicularly to the surface opposite to the detector. This is not the real situation since the source is not emitting isotropically but it allows to reduce the computing time. In fact gammas hitting the crystal with a non-right angle have lower probability of releasing all their energy

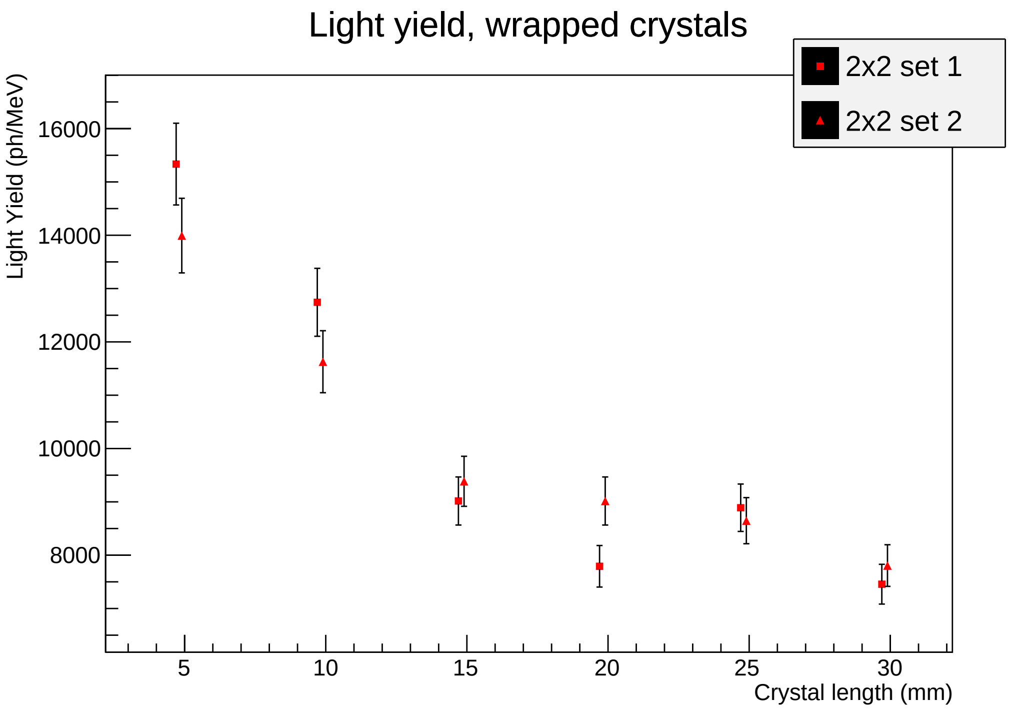

Figure 5.19: Chart of the LY values for the 2×2 mm^2 series with wrapped crystals.

	2×2 mm^2	3×3 mm^2
Length (mm)	**LY (ph/MeV)**	**LY (ph/MeV)**
5	19603	17829
5	19559	18362
10	17091	17759
10	17590	16688
15	16139	16671
15	15500	15387
20	14289	14512
20	13910	15035
25	13960	13960
25	15114	14010
30	13594	13155
30	13660	12553

Table 5.8: LY values for the 2×2 mm^2 and 3×3 mm^2 series with grease applied to crystals.

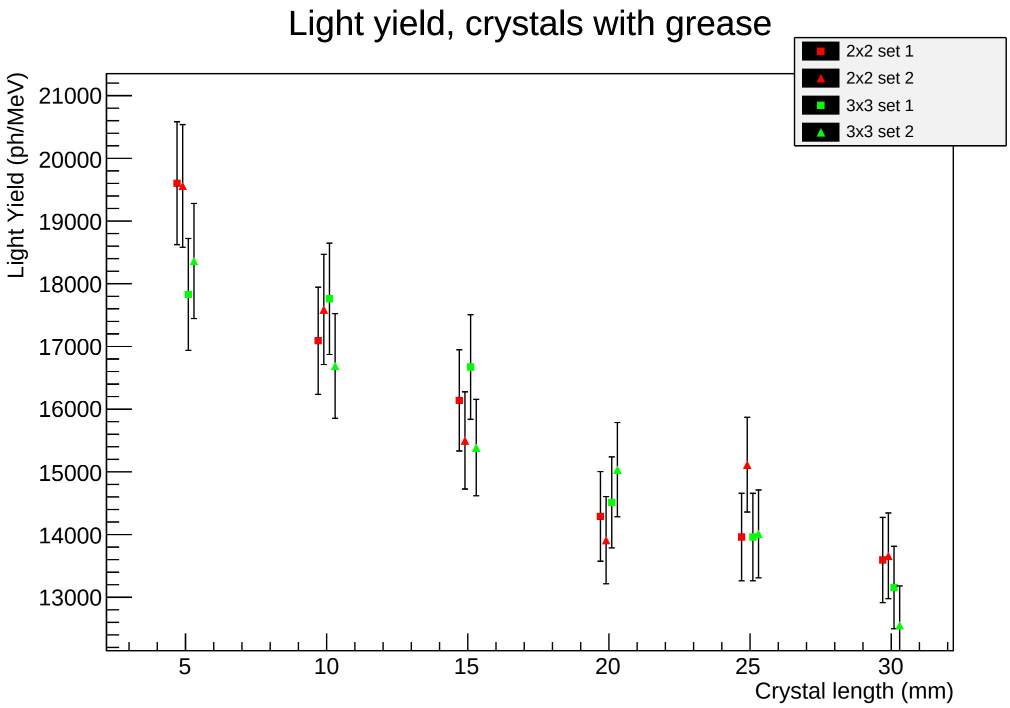

Figure 5.20: Chart of the LY values for the 2×2 mm^2 and 3×3 mm^2 series with grease applied to crystals.

and they will not contribute to the photopeak. Gamma energy is converted by the software in a number of optical photons depending on the light yield value chosen for the scintillator material simulated.

Both sets of 2×2 mm^2 and 3×3 mm^2 LYSO crystals are simulated in three configuration:

- naked crystal without optical grease;
- naked crystal with optical grease;
- crystal wrapped by Teflon without optical grease.

The number of optical photons extracted from each gamma is collected and a spectrum, very similar to the one obtained during measurements, is created. From this histogram the photopeak mean value can be calculated. The aim of this work is to evaluate the light output gain that can be obtained applying different surface treatments and compare LY of different crystal geometries. Hence it is not necessary to calculate absolute values applying Equation 5.6.1, but photopeak mean values can be directly compared using a normalization parameter.

For example, in Figure 5.21 values are calculated dividing the LY of each crystal, extracted from the simulation, by the 2×2×5 mm^3 crystal value of the same surface

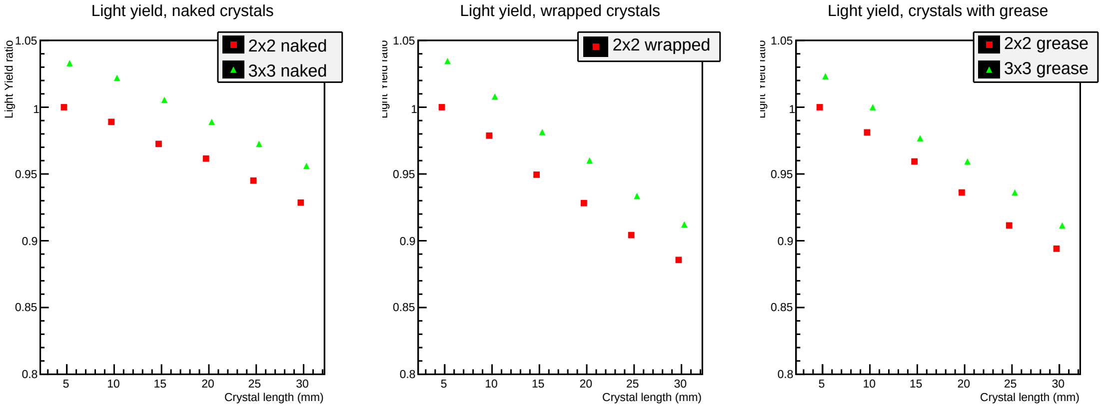

Figure 5.21: Plots of the LY ratios extracted from the **simulations** of the 2×2 mm^2 and 3×3 mm^2 series with naked (left), wrapped (center) and greased crystals (right). Ratios are calculated using the correspondent 2×2×5 mm^3 crystal value as normalization.

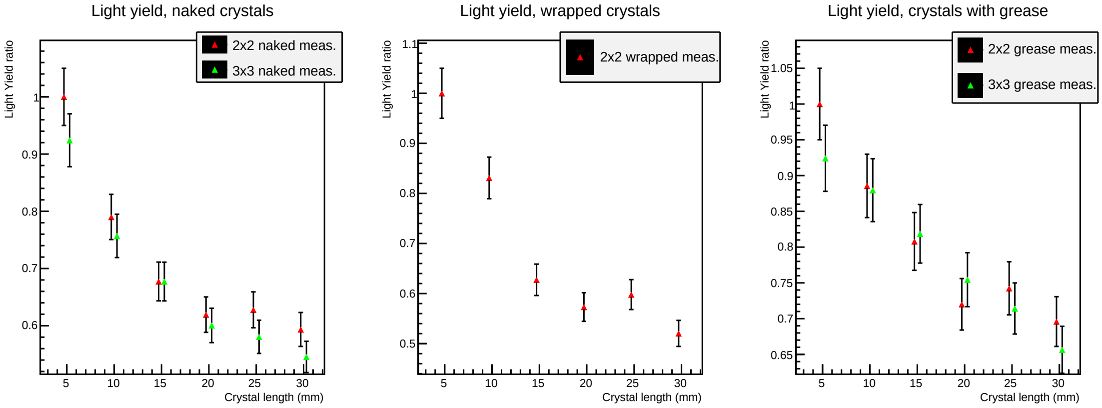

Figure 5.22: Plots of the LY ratios extracted from the **measurements** of the 2×2 mm^2 and 3×3 mm^2 series with naked (left), wrapped (center) and greased crystals (right). Ratios are calculated using the correspondent 2×2×5 mm^3 crystal value as normalization.

treatment. Naked, wrapped and crystals with grease application are reported in the left, center and right plot. In Figures 5.22 LY values obtained by the crystals measurements in laboratory are re-elaborate to have the same representation and make a comparison easier.

Some consideration can be done:

- if the LY of each crystal wrapped or with grease application is divided by the value of the equivalent naked crystal, it is possible to obtain the LY gain due to the treatment applied. Averaging values of the same sets a comparison between measurements and simulations can be performed. For what regards wrapped crystals, simulations shows a ratio of about 2.02 (that means a gain of 102%). A value of 2.07±0.16 can be extracted from LY measured in the laboratory. The ratio of the optical photons output for simulated crystals with

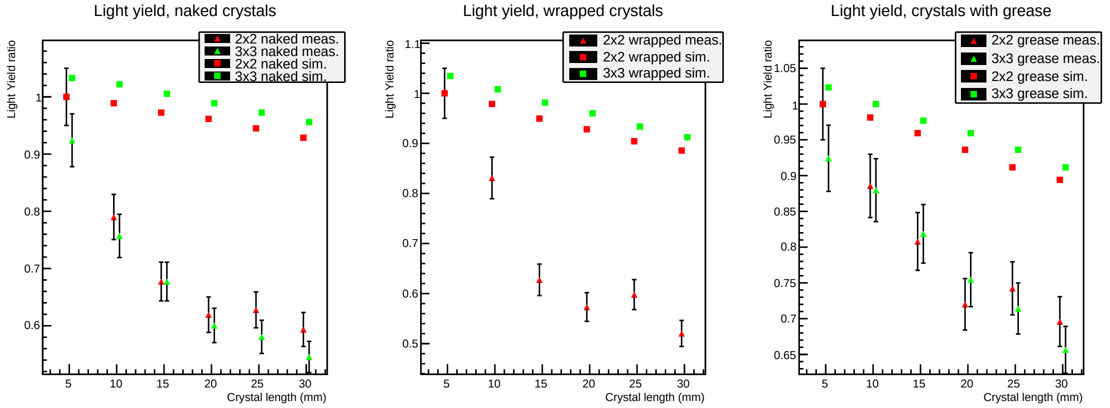

Figure 5.23: Comparison of the LY ratios extracted from the **measurements** and from the **simulations** of the 2×2 mm^2 and 3×3 mm^2 series with naked (left), wrapped (center) and greased crystals (right). Ratios are calculated using the correspondent 2×2×5 mm^3 crystal value as normalization.

grease is about 3.69 if compared to naked crystals. While the value obtained from measurements on real crystals is 3.34±0.25;

- simulations show that crystal length (2×2 or 3×3 mm^2) affects LY values in minor way with respect to what is measured on real crystals. Differences are about few percentage points compared to a loss of almost 50% between the longest and the shortest crystals. A direct comparison between normalized LY value of both simulations and real measurements is shown in Figure 5.23.

This results shows that the Monte Carlo software is able to reproduce with good agreement the increase of the photons extraction efficiency that crystals treatments as wrapping or grease application give. Unexpectedly it appears more difficult to simulate the optical photons loss as they move inside crystal bulk. A reason can be found in the structure imperfections that affect real crystals. Optical photons can be diffuse by these centres increasing the path length they follow inside the crystal. That means an higher probability to be absorbed before reaching one of the surfaces. Of course this process is magnified in longer crystals. In the same way imperfection and cracks on the surfaces where crystals were cut can diffuse optical photons or absorb them. To test these effects I run a first simulation where the photons hitting one of the crystal surfaces have a very small probability to be absorbed. In Figure 5.24 the results obtained with a 3% absorption probability are compared with LY measurements.

A similar test was conducted using a surface with a small diffusive component. In this case when a photon is reflected back into the crystal it may be scattered with a random angle instead of a specular one. Figure 5.25 shows the values obtained

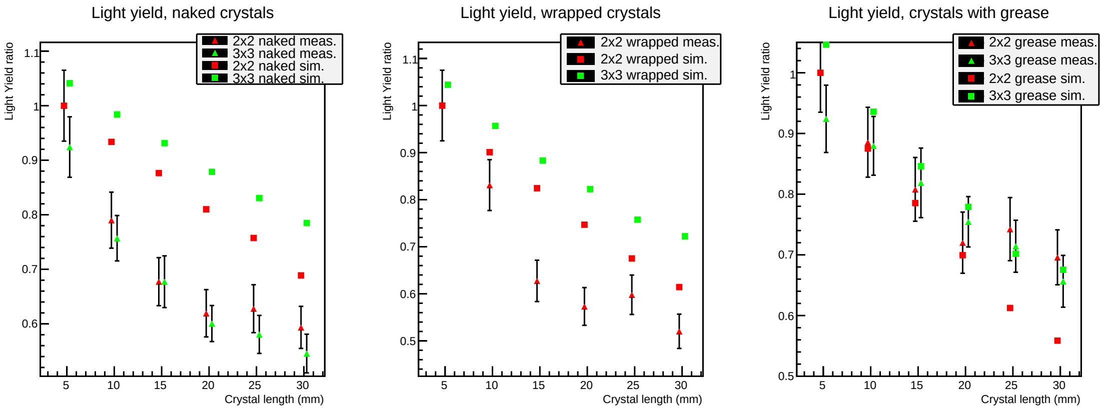

Figure 5.24: Comparison of the LY ratios extracted from the **measurements** and from the **simulations** of the 2×2 mm^2 and 3×3 mm^2 series with naked (left), wrapped (center) and greased crystals (right). A 3% **absorption probability** on crystal surface was introduced in simulations.

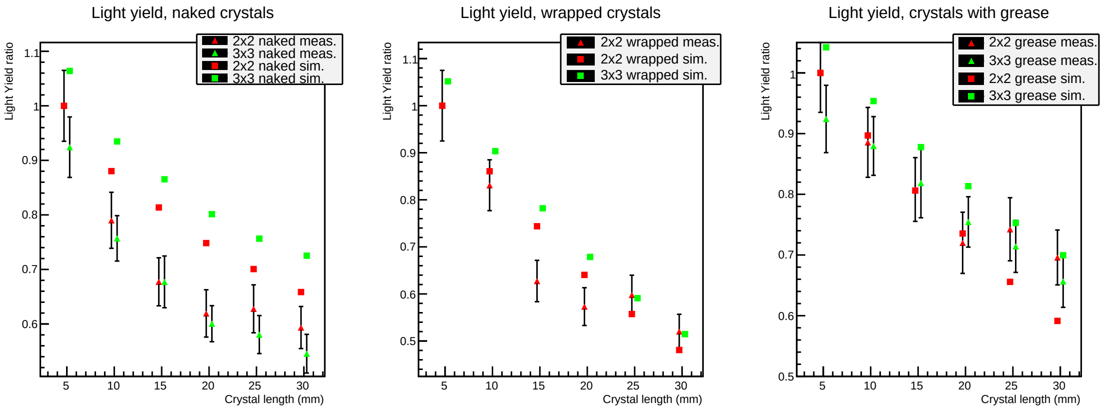

Figure 5.25: Comparison of the LY ratios extracted from the **measurements** and from the **simulations** of the 2×2 mm^2 and 3×3 mm^2 series with naked (left), wrapped (center) and greased crystals (right). A 5% **diffusive component** was added to the crystal surfaces.

Length (cm)	LY_1	LY_2	LY_3	LY_4
1.4	148	134	138	135
1.5	137	124	130	126
1.6	122	115	125	125
1.9	120	115		

Table 5.9: Light yield values for the four samples measured expressed in ph/MeV. Four sets of measurements were taken.

with a simulation where the surface has a 95% specular component and 5% diffusive. These simulations show that modifying some parameters regarding crystal surfaces is it possible to drastically change the simulation output. Far from being a procedure to apply to a generic crystal, it becomes a very specific modelling that requires a fine tuning on crystals samples available.

5.6.3 $PbWO_4$ Crystals

Light yield measurements were performed also on $PbWO_4$ samples. A crystal of the same batch used in the CMS experiment [27] was chosen. These anisotropic crystals, produced at the *Bogoroditsk Plant of Technochemical Products* [28], show the optical axis parallel to the small faces plane. The original 2×2×20 cm^3 crystal was cut parallel to the small faces, extracting four samples of about 2×2 cm^2 sections and length of 1.4, 1.5, 1.6 and 1.9 cm.

Since the Cs-137 source adopted in our measurements emits 661 keV gamma, a low light output was expected. The resulting energy resolution is not enough to distinguish the photo peak from the Compton edge as the first spectra acquired with naked crystals have shown. For this reason the Teflon wrapping was applied around crystals except for the surface coupled with PMT. In addition grease was applied to the extraction surface. The increased number of optical photons collected was enough to distinguish total energy releases from partial ones.

An example of the spectrum obtained can be see in Figure 5.26 where the 1.9 cm length crystal was measured and LY extracted. The plot shows also the fit applied to find the mean value of the photopeak. The function chosen was the same used for the LYSO crystals (Equation 5.6.3). Each crystal was measured four times with the exception of sample 1.9 where only two measurements were performed. Table 5.9 shows values extracted by measurements.

The photomultiplier used for these measurements proved to be unstable and gain error is the most relevant in Equation 5.6.3, estimated about 5%. Image 5.27 shows

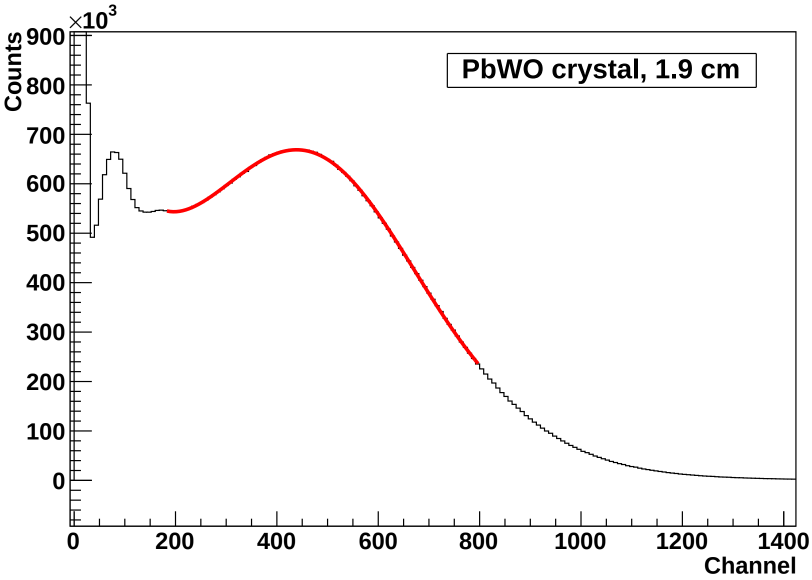

Figure 5.26: Spectrum obtained with a 6 min. long acquisition of the light output of the 1.9 cm length $PbWO_4$ crystal. The red line shows the fit applied to the photopeak.

the single values obtained for each crystal and set of measurements. In Plot 5.28 four sets have been averaged and error is calculated now from STD formula.

The self-absorption in crystals bulk and lateral light escape should decrease the light yield as the crystal thickness increases as seen with LYSO crystals. This effect is barely visible in Figure 5.28 where all the values are reported as function of the crystal length. Crystal 1.9 is practically compatible with the crystal 1.6 cm long. Two reasons can explain this behaviour: $PbWO_4$ has a low light yield per MeV and differences in crystals lengths are too small with respect to calculated errors to point out the exponential trend visible with LYSO crystals. On the other hand

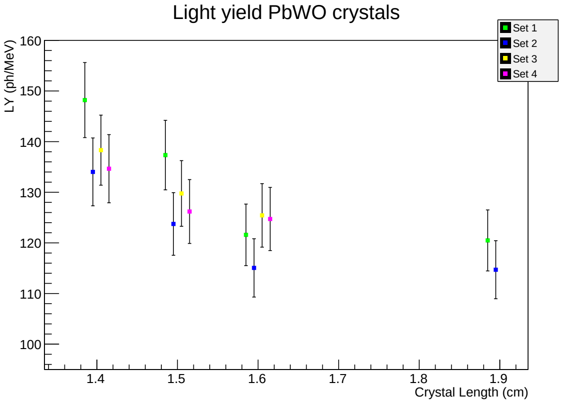

Figure 5.27: Light yield values of the 4 $PbWO_4$ samples; error is evaluated to be 5% of the measurements.

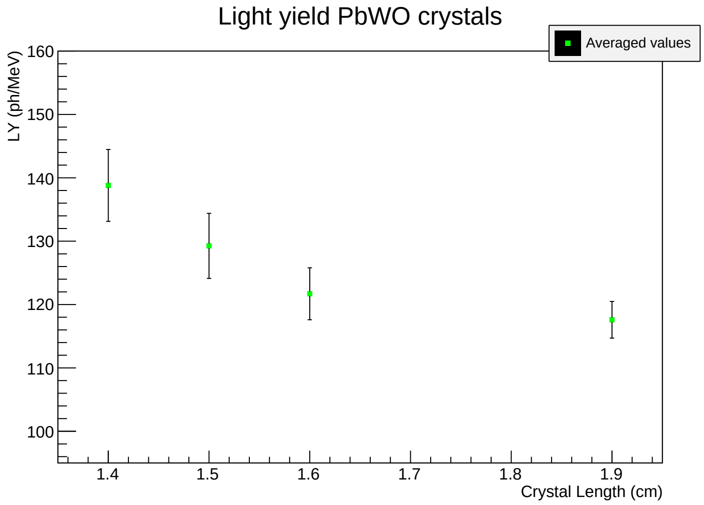

Figure 5.28: Light yield averaged values of the 4 $PbWO_4$ samples.

imperfections of the crystal structure and in particular of the edge where crystals were cut greatly influence the light output. Damages in the crystals do not work just as light absorbers but they can be diffusion centres. In this way optical photons that are exiting the crystal from the wrong side may be scattered again in the crystal volume.

5.7 Summary

The results I obtained have to be analysed taking into consideration the starting aim of this work: a comparison between Monte Carlo toolkits to find the most suitable for EndoTOFPET-US project. With this premise, it is possible to say that both the software are able to simulate ray tracing of optical photons in isotropic crystal. There are minor differences in how surfaces treatments are handled that can be stressed with dedicated simulations but basically they can be ignored if users are interested in the photon extraction efficiency of crystals. Differently, if the simulation of an anisotropic crystal is required, SLitrani becomes a mandatory choice. For our purpose this feature is not necessary since the collaboration was already oriented to use LYSO crystals because of their density and light yield and this material does not show anisotropic behaviour. Physics processes involved can be summarized in interaction between gamma rays and materials (that means photoelectric process and Compton), scintillation inside the crystals and ray tracing of optical photons. These are simulated by both software but different complexity models are applied. The absence of secondary particles in SLitrani is a serious problem for timing applications and EndoTOFPET, as the name reports, requires computing of the gammas time of flight. Both MC toolkits are able to simulate complex geometry like crystals matrices with different layers of packaging and wrapping. More generic evaluations but not less important in the choice between the two simulators were taken into consideration:

- both G4 and SL are open source has preferred by the collaboration;
- extraction of the physics information during the particles lifetime in a simulation is easier in Geant4 but the code required for a SLitrani simulations is shorter to be created;
- the time required to run a simulation was also taken into consideration. A simulation like the one used in the LY measurements (in isotropic configuration) was performed with both the software. Geant4 required about 10 minutes while SLitrani lasted for 25 minutes. Also in simulations where only ray tracing is required (only optical photons are produced) Geant4 results almost twice faster than is similar. Even if Geant4 seems better, it is important to notice that this is not an absolute evaluation because only after a good optimization the codes can be compared. More studies are required about this topic;
- eventually it was also considered that Geant4 was born from a large collaboration and from 1998 (first public release) the number of people and organization involved has become bigger and bigger. This allows to have a frequently updated code and fast support if help is required. Moreover developers have created, starting from Geant4 particles libraries and classes, toolkits with specific characteristics for every kind on simulation (see *GATE* in next chapter).

Evaluating all these factors, Geant4 was chosen inside the collaboration as the software to be used in EndoTOFPET simulations.

Chapter 6

ENDOTOFPET-US SIMULATIONS DEVELOPMENT

6.1 Framework

The EndoTOFPET-US prototype is a innovative scanner for the study of the pancreatic carcinoma and the prostatic cancer. It consists of a PET head mounted on a commercial ultrasound endoscope and a PET plate to be placed outside the patient body (see Section 2.2.2 for more details). In particular the probe requires very tight constraints regarding its dimension because of the limited space available to reach the organ of interest. In a cylinder of about 15 mm diameter and 20 mm length a matrix of 9×18 crystals, each one with a volume of $0.71\times0.71\times15$ mm^3, has to be inserted. The SiPM array for the crystals readout, the cooler system and the EM tracking sensor must be placed in the same space too. The miniaturization required by the probe offers a challenge to the people working on this project but also the external PET plate presents some space limitations because it must be placed near the patient and moved in order to cover a wider angle of view. The final goals of a spatial resolution of 1 mm and a coincidence time resolution of 200 ps are ambitious but the first results on some of the single components are encouraging. How the choice of scintillator crystals, their dimensions and their readout impact on the PET scanner performance can be foreseen using the support of Monte Carlo simulations. The Collaboration of the EndoTOFPET-US project has eventually chosen Geant4 as simulation tool. In order to simulate the electronic chain of a detector that is responsible of converting optical photons in a digital signal and eventually in an events list GATE was chosen. It is an open source software specifically developed for the simulation of medical imaging scanners and radiotherapy [29]. It uses Geant4 libraries for the particles interactions while dedicated classes are developed for the simulation of the electronics chain and the drawing of medical imaging scanner, overcoming G4 complexity in defining the geometry.

6.2 Implementation

6.2.1 Geometry

The geometry I simulated reproduces in a simplified way the external plate and the probe of the EndoTOFPET scanner. I focused my attention on the reconstruction of crystals dimensions, arrays layout and casing while I omitted all the readout and service components surrounding crystals as SPADs, electronic connections and cooling system. Following the same modularity defined by the project, the crystals arrays that compose both detectors were divided in module and sub-module. I created a configuration file to pass all the geometric information to the simulation software. By mean this file it was possible to modified easily the initial parameters as:

- crystals dimension;
- gap between crystals;
- number of crystals per sub-module;
- number of sub-modules per module;
- number of total modules;
- crystal and casing material.

In Figure 6.1 an example of the detector geometry which can be simulate is shown, together with the list of parameters used.

6.2.2 Data analysis

GATE is able to simulate the electronics chain of a PET scanner. It means that starting from the single events detected on each plate it is able to provide a list of the detected coincidences and all the related information as: energy deposited, time of detection, double readout, if depth of interaction is implemented, and affected crystals IDs. Also sources of uncertainty that are introduced by the acquisition chain

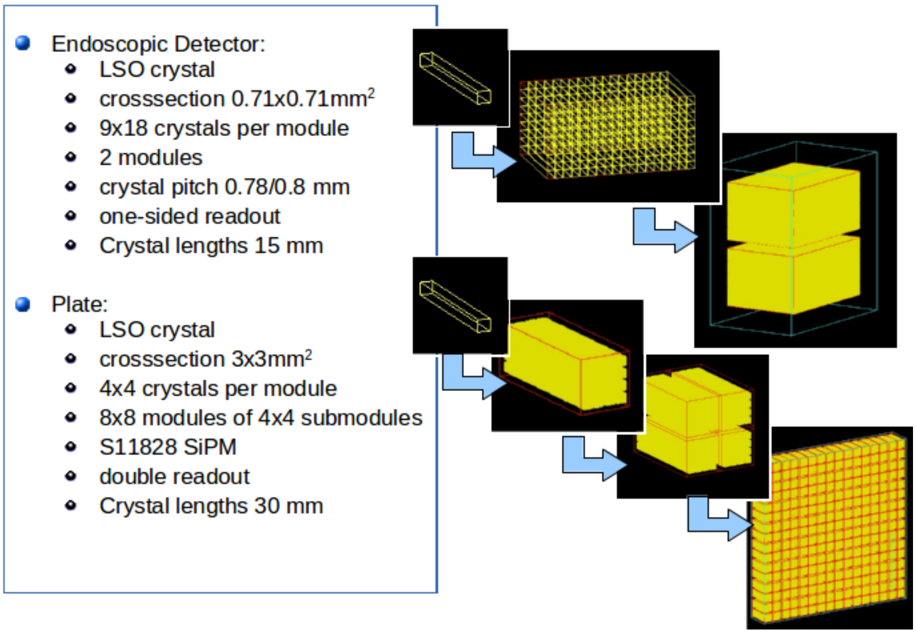

- Endoscopic Detector:
  - LSO crystal
  - crosssection 0.71x0.71mm^2
  - 9x18 crystals per module
  - 2 modules
  - crystal pitch 0.78/0.8 mm
  - one-sided readout
  - Crystal lengths 15 mm
- Plate:
  - LSO crystal
  - crosssection 3x3mm^2
  - 4x4 crystals per module
  - 8x8 modules of 4x4 submodules
  - S11828 SiPM
  - double readout
  - Crystal lengths 30 mm

Figure 6.1: One of the detectors configuration I have simulated. The S11828 SiPM imposes own constraints on plate crystals pitches.

are simulated defining some parameters as energy resolution, time resolution and DOI resolution. Relevant modification to the GATE software have been required because GATE is not able to simulate asymmetric plates detector. GATE can simulate the EndoTOFPET probe and the external plate in the same run, in this way they share the same gamma source, but each detector behaves as an independent SPECT detector. The asymmetric configuration is quite unusual in PET scanners because normally the gamma source (i.e. the patient) is in the center between the two plates and there are no geometrical constraints, for this reason it was not expected in GATE. This issue required to redevelop what regards the chain simulator from beginning. While writing the new code to adapt GATE, I have added also new features that GATE version did not take into account. This code (called *Coincidences Sorter* or CS) was developed in C++ including ROOT libraries. It consists of two parts:

- **Smearing**: As explained before, the data each detector collects have to be modified with the introduction of an error to simulate the precision of the instrument and of the electronic chain. When a gamma deposits energy in a crystal, its ID and the one of the sub-module, module and detector is stored in a list that collects all these single events. Also the energy deposited, the time of arrival and the relative position inside the crystal are registered. The "smearing effect" is applied to these values (except for the ID). The singles list is scrolled and each parameter was randomly modified following a Gaussian

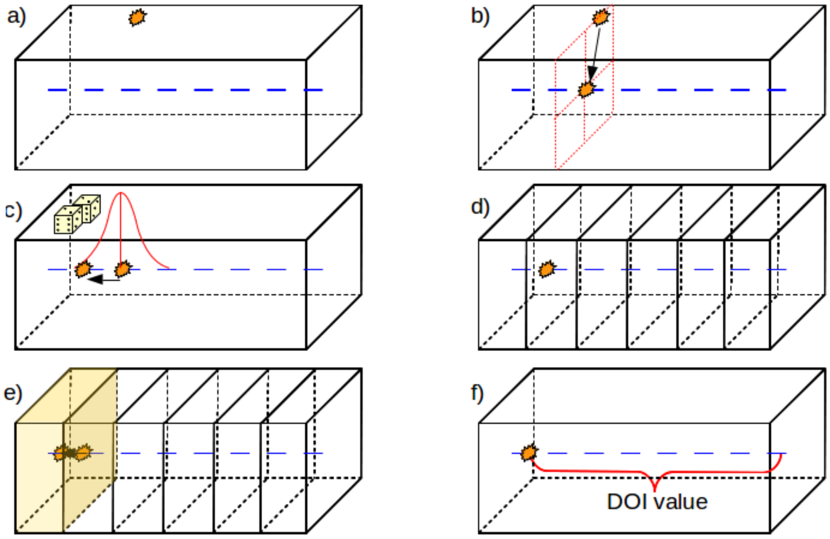

Figure 6.2: Graphical scheme of the method applied for the DOI calculation.

function centred on the value itself and with σ depending on the instrumental resolution. For what concerns the measurement of the DOI, I am interested only to hit position with respect to one of the extracting surfaces. For this reason the three coordinates of the hit position I obtained from the simulation, are changed in a single value that is calculated projecting the hit position on the main crystal axis. Then the smearing is applied to the DOI value. Constraints are placed for the DOI calculations because if the random extraction brings the position out of the crystal borders, it is eventually rejected. Then the crystal is divided in *crystal length / DOI precision* segments and the DOI interaction value is shifted to the center of the segment the hit belongs to.

The smearing values are based on what was supposed to be the resolution of the EndoTOFPET scanner (see Section 2.2.2) but also other values were tested. GATE toolkit and custom made chain simulator can be launched independently. This is better than what GATE does since in single long simulation I am able to apply the effects of the coincidences sorter with different parameters instead launching several time consuming simulations.

- **Sorting**: When the new values are calculated with the smearing function, it is necessary to transform the singles list in a coincidences list. To decide if two events, belonging each one to a different detector, are a coincidence three different algorithms have been created.
  - *Kill All*: The first element of the singles list is read and a time window is opened. The list is scrolled and if another event belonging to the

other detector falls before the end of the time window the coincidence is created. Then the first single in the list after the closing of the countdown will trigger another time window and coincidence will be chosen with the same criteria. If no second event falls in the required time, no coincidence is created. If more than one event belonging to the second detector can be chosen, only the first is considered and the others are lost.

- *Keep All*: The algorithm is similar to the previous one but if the triggering event can be coupled with more than one event of the second detector within the time window, all the possible coincidences are saved.
- *Keep Best*: A bit more complex than the other two methods. The first event triggers the countdown. All the elements belonging to the same detector that fall inside the time window are collected and the one with the highest energy is chosen. The same method is applied to the events of the other detector and the coincidence is created between the chosen ones.

Other two option can be activated in addition to these methods and they depends mainly on the acquisition procedure of the scanner electronics.

- *Multiple windows*: Each event creates its own time window even if it was already included to the one of a previous element in the single list. The idea is that crystals are independent from each others and readout electronics is able to acquire more than one signal at a time.
- *Neighbouring crystals*: The triggering event can be replaced by another event falling within the time window but only if it happened in a crystal surrounding the initial one and if its energy is bigger. The same criteria is used for the choice of the second event of the coincidence. As *Keep Best* method it should be able to take into consideration crosstalk effect and multiple energy depositions.

Using these algorithms I am able to tune the number of true, random or scatter coincidences accepted in the simulation. For instance, the most restrictive one can be used in simple simulations where it is possible to simulate a very large number of decays and the scanner sensitivity is not a limit. I have developed a controller software to launch simulations and data analysis in parallel on computers where multi-core processors are installed. This gives us the possibility to obtain an output up to 15 time faster then launching single simulations. The list of coincidence events is then processed by the reconstruction algorithm that is able to create a 3D map composed

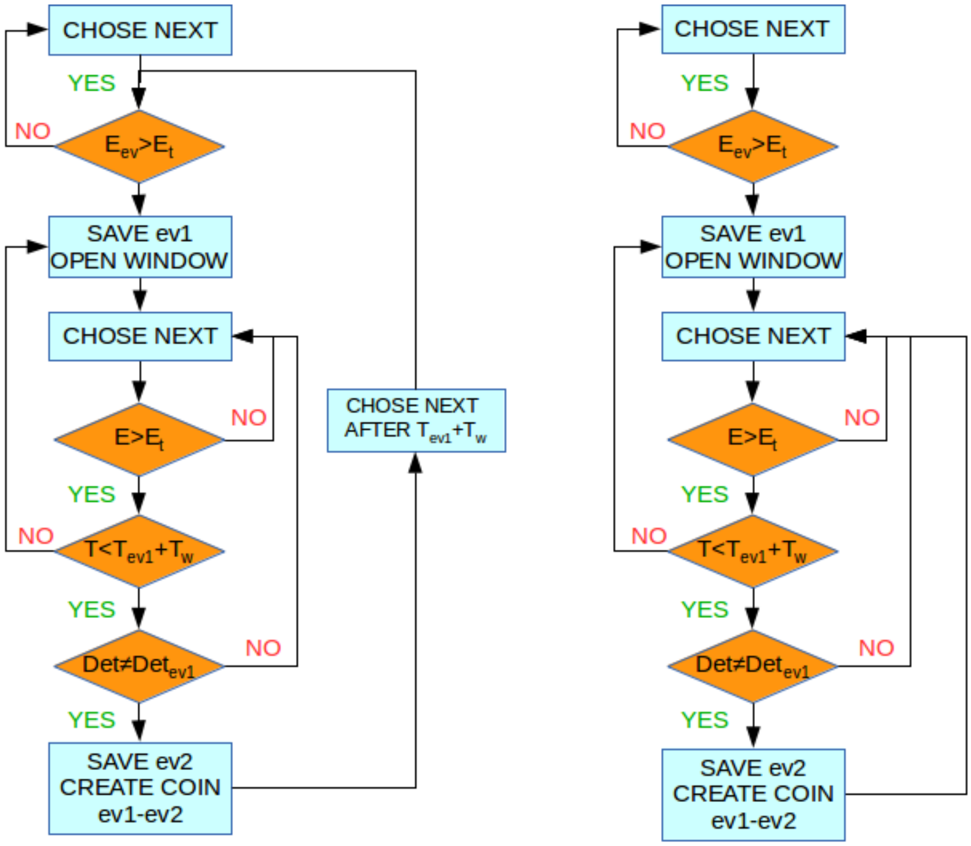

Figure 6.3: "Kill All" algorithm to chose coincidences in singles lists files.

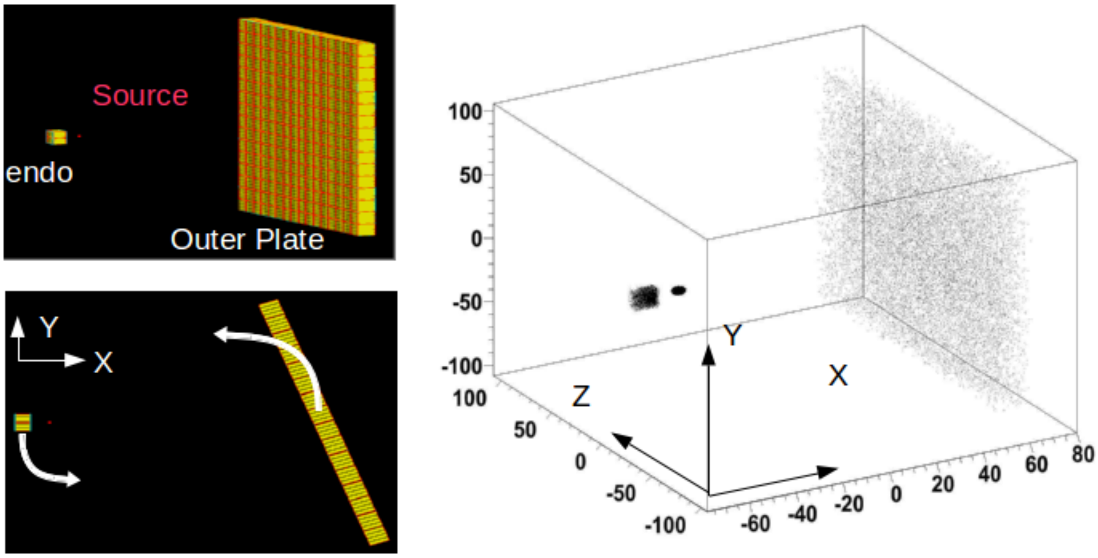

Figure 6.4: a) A scheme of the probe coupled with the external plate and the point source placed between them. b) Orientation of the axis and rotation of the system. c) Visualization of the coordinates where gammas were generated and where hitting the crystals.

by voxels [30]. Each element will carry a number proportional to the number of decays that have taken place in that region of space and to the density distribution of the emitting source (which in our case come from the radiopharmaceutical).

6.3 Simulations

6.3.1 EndoTOFPET vs ClearPEM detector

As first test, I decided to run a comparison between EndoTOFPET detector with a hypothetical scanner composed by two symmetric plates as the ones used in the CleraPEM (see Sec. 2.2.1). This simulation should be as a sort of verification test for the choices made in the EndoTOFPET configuration. The two plates scanner is shown in Figure 6.5 with a 1 mm radius 250 kBq source placed in the middle, at 20 cm from the inner faces of both the detector heads. The system was rotated by 135° around z axis centred in the source and at each 45° step an acquisition of one minute was computed (see Figure 6.4). The four lists of single events obtained were analysed using the Coincidences Sorter and results were reconstructed by mean of a listmode algorithm, performed without further iterations.

Spatial resolution is one of the main parameters adopted to test the quality of the image and therefore the performance of the scanner. If we want to calculate the spatial resolution along the z axis we extract a slice of the 3D map in the X-Z plane

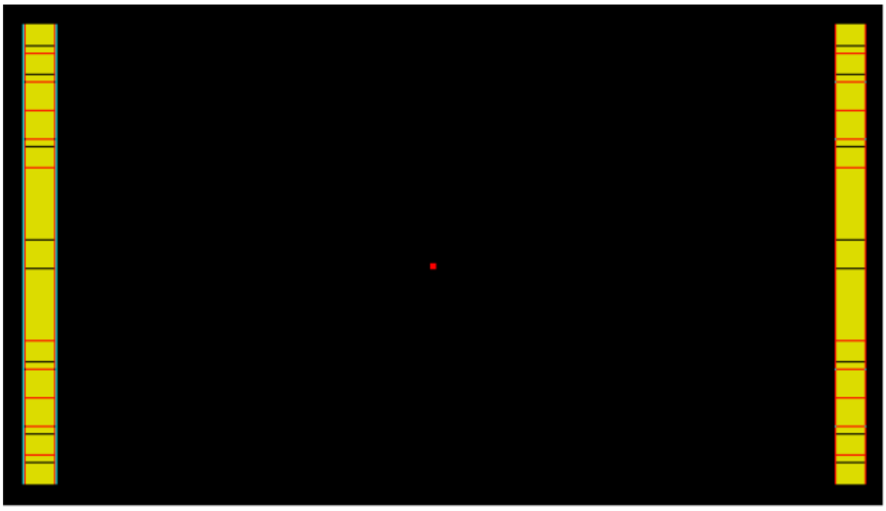

Figure 6.5: A scheme of the two plates with a point source placed in the middle at 20 cm from the internal surfaces.

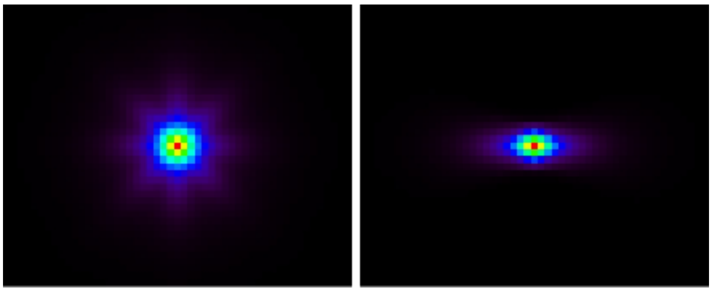

Figure 6.6: Reconstruction of the 1 mm source placed at 20 cm between the two plates. On the left a transverse view and a coronal view on the right. DOI correction not activated.

at y = 0 (in the simulation the source is placed at 0,0,0 and the two detectors are centred in front of it). If we analyse the profile of the slide at the x value where the voxel with the maximum number of counts is placed we obtain a Gaussian curve. The FWHM of this distribution gives the spatial resolution. For the point source simulated the spatial resolution along z was calculated to be 2.80 ± 0.05 mm (± 2%) FWHM, without applying DOI analysis and with 51×41×41 voxels with a size of 1 mm^3. When I enable DOI calculation, the spatial resolution can be reduced to 2.23 ± 0.04 mm FWHM. Sensitivity is another parameter required for the evaluation of the scanner. For the configuration described, I calculated a value of 20.95 ± 0.06 cps/kBq.

At this point I simulated the EndoTOFPET scanner placing the probe at -20 mm from the point source and the external plate at 200 mm as in the previous case. From the reconstruction I obtained an spatial resolution in z of 1.84 ± 0.03 mm without DOI analysis. The result is unchanged if DOI correction is activated. A sensitivity of almost 10 cps/kBq is obtained under this configuration.

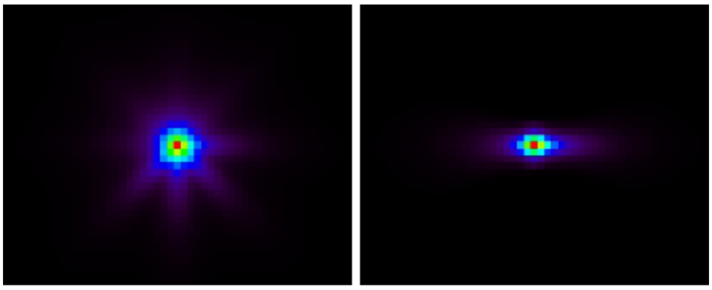

Figure 6.7: Reconstruction of the 1 mm source placed at 20 cm between the two plates. On the left a transverse view and a coronal view on the right. DOI correction activated.

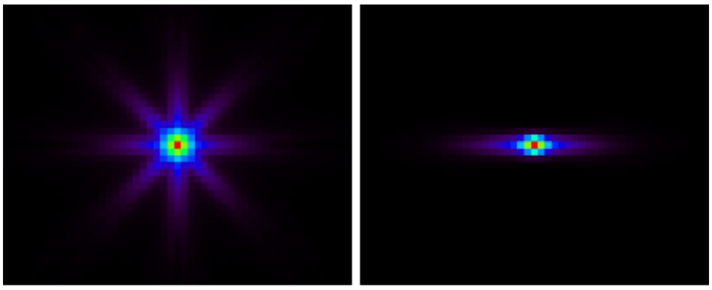

Figure 6.8: Reconstruction of the 1 mm source placed at 20 mm from the probe and the 20 cm from the two plates. On the left a transverse view and a coronal view on the right.

If we compare the two systems we can see that EndoTOFPET scanner has a 53% improvement on the spatial resolution (without DOI information) but almost half sensitivity with respect to two plates version. Table 6.1 summarizes the results I obtained.

6.3.2 Plate shape

The collaboration had to chose between two possible configuration for the external plate: planar and curved. For this reason I simulated these shapes and their sensitivity was compared (Figure 6.9). In particular I simulated a point source with 0.5 mm of radius and a 250 kBq activity. The probe was placed at 20 mm from the source while the front surface of the plate at 200 mm. I decided to use this configuration as a standard since it is very similar to the real condition in which EndoTOFPET

	Spatial resolution (mm)		**Sensitivity (cps/kBq)**
	with DOI	without DOI	
EndoTOFPET	1.84 ± 0.003	1.84 ± 0.003	$\simeq 10$
Two plates	2.80 ± 0.05	2.23 ± 0.04	20.95 ± 0.06

Table 6.1: Spatial resolution and sensitivity simulated in EndoTOFPET and two-plates configurations.

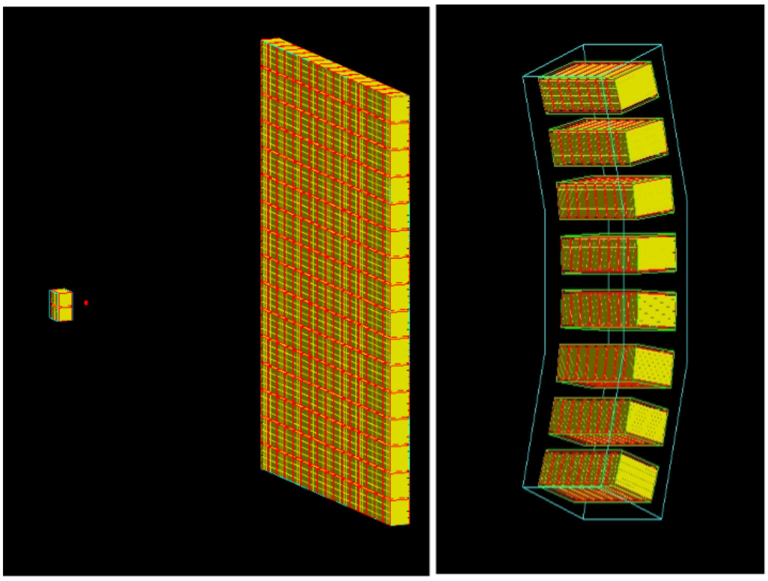

Figure 6.9: Scheme of the planar and the curved plate designed for the EndoTOFPET scanner.

scanner should work. For this simulation I rotated the scanner by 360° around z axis (with the centre in the source itself) and at each step of 45° an acquisition of one minute was computed. I tested the EndoTOFPET design with a planar and a curved plate and compared the sensitivity results with a theoretical configuration composed of two monocrystalline plates detector and a two plates detector with the segmentation used for the probe or the plate itself (similar to ClearPEM design).

The first information that can be extracted form Plot 6.10 is that planar and curved geometries present very similar values. Secondly both configurations have a smaller sensibility compared to the ClearPEM design or to two monocrystalline plates. Eventually the collaboration has chosen the planar configuration because it offers an easier assembling, even if this choice is preferred to the curved plate also for a marginally better sensibility (see zoomed box in Plot 6.10).

6.3.3 SiPM arrays

As explained in Sec. 2.2.2 the EndoTOFPET scanner should be equipped with SiPM (grouped in matrices) to readout the crystal light output of external plate. The gap between two crystals of the same matrix (or the distance between two matrices) depends on the position of the SiPM mounted on the array board. The collaboration have chosen several candidates as SiPM arrays each one with a different geometry. The sensitivity (defined as the rate in counts per second between detected true coincidence events and a given source activity) can be influenced by these differences

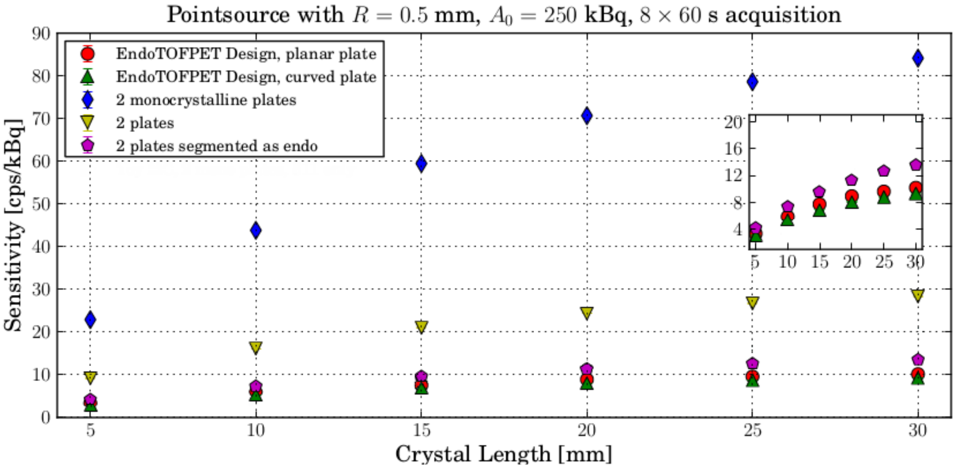

Figure 6.10: Sensitivity calculated for different plate configurations, some theoretical geometries have been added as comparison.

and a Monte Carlo simulation is a valid tool to calculate the scanner response.

Initially two SiPM models from Hamamatsu were tested, S11828 as the original choice and S11064 as the alternative. The first model is more compact since each row of SiPM as a common voltage supply and its geometrical filling factor is about 74%. Second one is composed of 4×4 completely indipendent SiPM, each one with active area of 3×3 mm^2, but with a total geometrical filling factor of 48%.

A point source of 1 MBq was placed at 2 cm from the front of the probe and 20 cm from the inner plate surface. LSO crystals were adopted. The system was rotated as in the previous simulation and eight steps of 45° were performed. Several plate crystals lengths were tested in both configurations while probe geometry was left unchanged. Sensitivity values obtained are shown in Figure 6.13. The S11828 model shows a sensibility 28% higher than S11064 model independently from the simulated crystal lengths. On the other hand, the sensitivity of a model increases with the crystal length since it gets more and more efficient in the 511 keV gammas detection.

S11828 and S11064 are not the only models taken into consideration. Another comparison between new SiPMs was conducted testing different parameters (Table 6.2) while other elements were fixed during this simulation campaign (Table 6.3 and 6.4).

The SiPMs arrays dimensions are reported in Figure 6.14.

As in the previous simulation, the probe was placed at 20 mm from the source, while plate was 200 mm on the other side. The source simulated is a sphere with 0.5 mm radius and 1 MBq activity. Each configuration was studied with one minute time acquisition, during which a rotation of 360° around Z-axis centred in the source

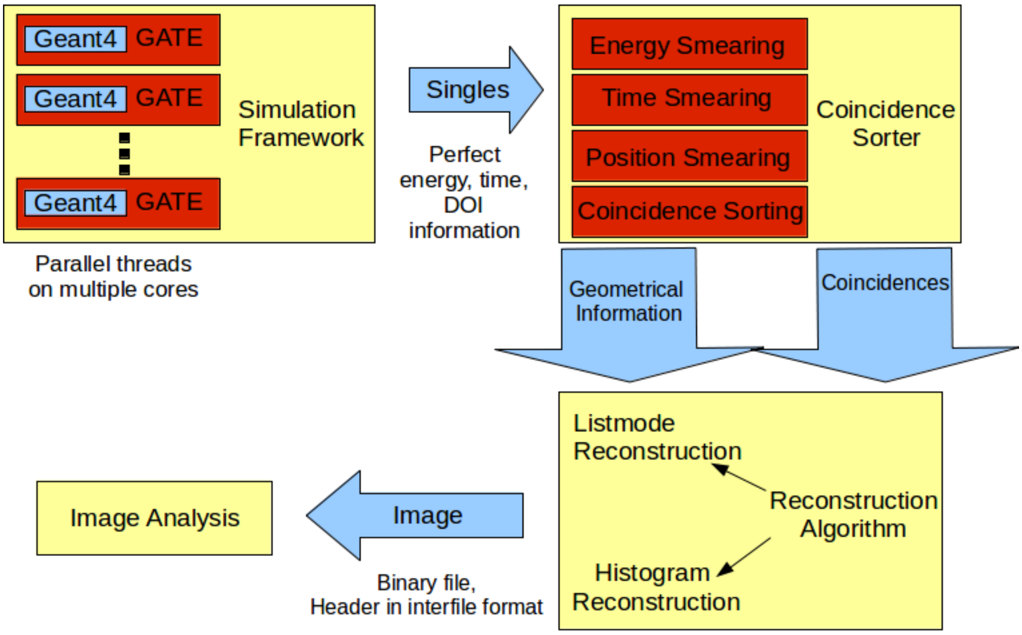

Figure 6.11: Scheme of analysis chain used for my simulations, from generation of data with Geant4 to the reconstruction algorithm.

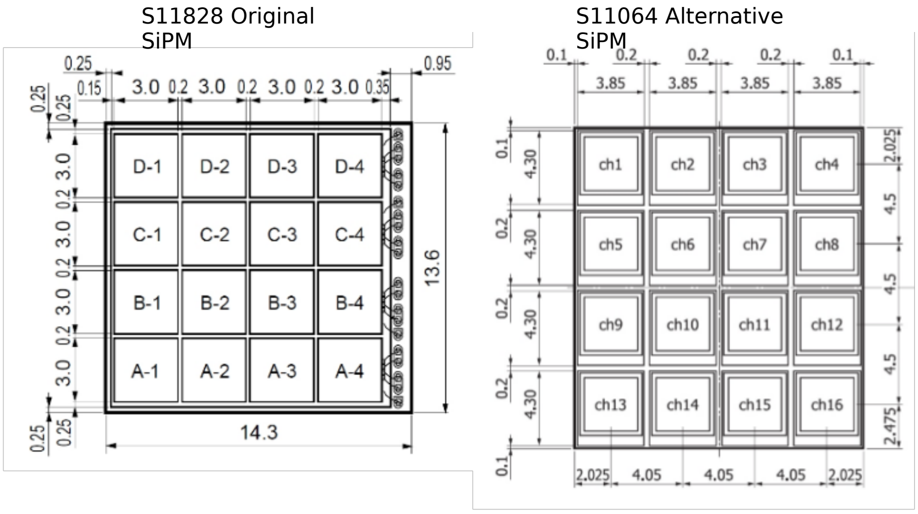

Figure 6.12: Schemes of two possible SiPM models, candidates for crystals plate matrices.

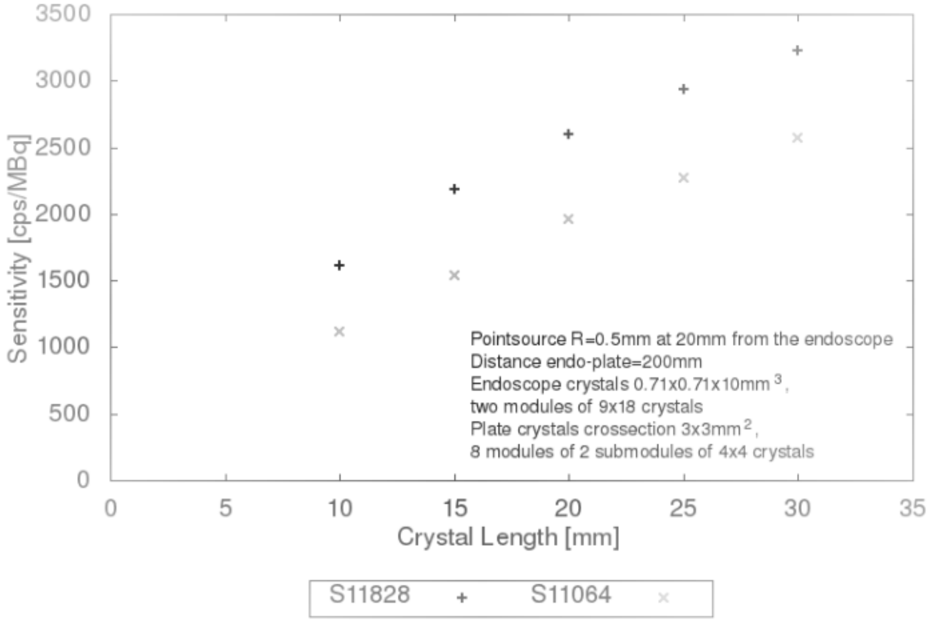

Figure 6.13: Plot of the sensitivity values obtained testing two possible SiPM models and different crystals lengths.

Studied Elements
Endoscopic probe:
Crystal lengths 10 or 15 mm
External plate:
Crystal length 5-30 mm, steps of 5 mm
Crystal cross-section 2×2, 3×3 or 3.25×3.25 mm^2
Different MPPC geometries

Table 6.2: Elements tested during the simulations.

Endoscopic Detector	
Material	LSO
Cross Section	0.71×0.71 mm^2
Crystals per module	9×18
Num Module	2
Crystal pitch	0.78/0.8 mm
Readout	one-sided

Table 6.3: Probe elements not modified during the simulations.

Plate Detector	
Material	LSO
Submodules per module	4×4
Num Module	8×8
Readout	two-sided

Table 6.4: Plate elements not modified during the simulations.

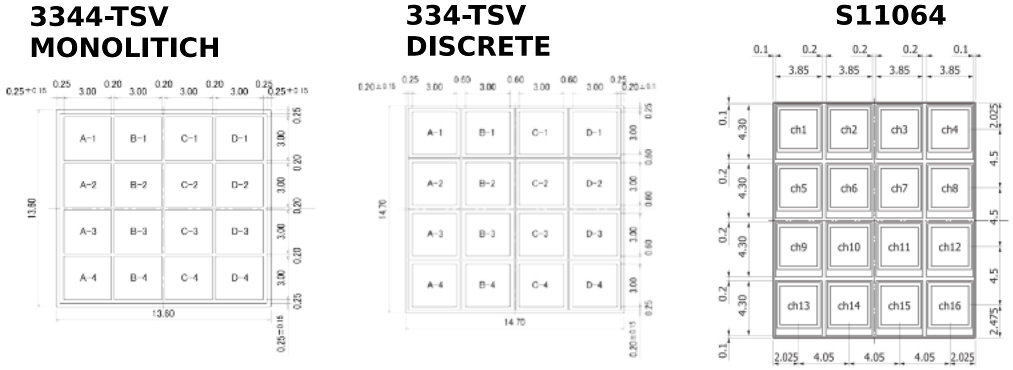

Figure 6.14: Schemes of three possible SiPM models, candidates for crystals plate matrices.

and steps every 45° occurs. Sensitivity results are shown in Figure 6.15 where a fit was also performed for each configuration. The error on each point is about 1% and it is obtained calculating the standard deviation from the 8 acquisition projections.

The simulation of the SiPM array with an active area of 3.25x3.25 mm^2 was added as a theoretical example. From the values I obtained we can summarize the effects that different geometries have on detector sensitivity:

- if we exclude the S11064 that has a very low filling factor, for the other SiPM models increasing the cross-section from 2x2 mm^2 to 3x3 mm^2 the sensitivity is increased of 30%;

- plate crystal length is still an important factor and generally increasing it from 15 mm to 30 mm the detector sensitivity has a gain of 40-50%;

- also the endoscope crystals length modifies the studied parameter: 15 mm long crystals have +30% sensitivity with respect to 10 mm.

I applied a back-projection with single iteration to the results and I created images of 0.5×0.5×0.5 mm^3 voxel size and with 41×41×21 voxels. From these images I evaluated the spatial resolution along the three axes as explained in Section 6.3.1.

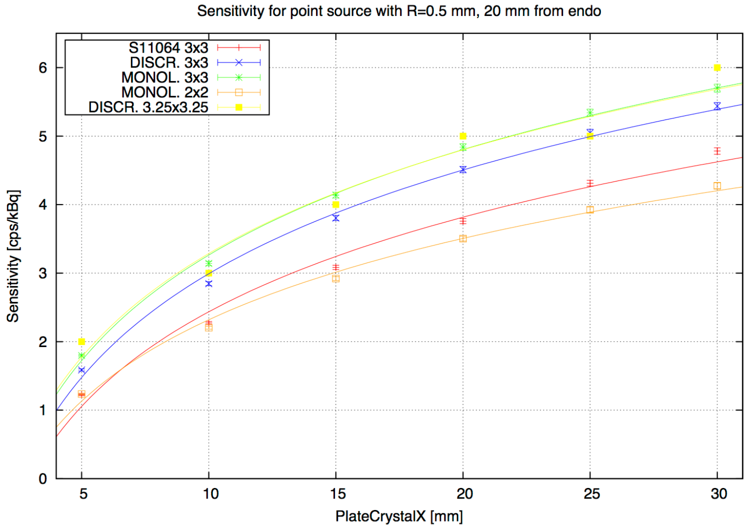

Figure 6.15: Sensitivity values of different SiPM models.

Figures 6.16 and 6.17 show the results I obtained for the geometrical configurations simulated.

From this data it is possible to extract some considerations:

- the CS applied to these simulations was run with the DOI information turned off. It meant that every hit is considered as coming from the crystal center. Therefore a parallax error is expected, in particular in longer crystals. However the geometric configuration of the probe results almost independent by DOI. Both plot 6.16 and plot 6.17 show that the variation of the spatial resolution is only 2% if we compare a 5 mm long crystal with a 30 mm long crystal. All the configurations show the same effect. A first explanation to this effect is that a point source placed in the center of rotation and very closed to the probe is too simple to introduce such an evident error and simulation with more complex subjects are required. A second reason could be that only a better image reconstruction algorithm is able to enhance DOI effect. Results shown in Section 6.3.1 seem to confirm this invariance for the DOI correction;
- differently than expected, along Z axis (see Fig. 6.16) a better spatial resolution in longer crystals is obtained. This improvement can only be explained by the better statistics longer crystals are able to achieve. Along X axis spatial resolutions gets worse with crystal length increasing as normally expected. Probably the larger number of counts is not able to balance the error introduced by longer crystals;

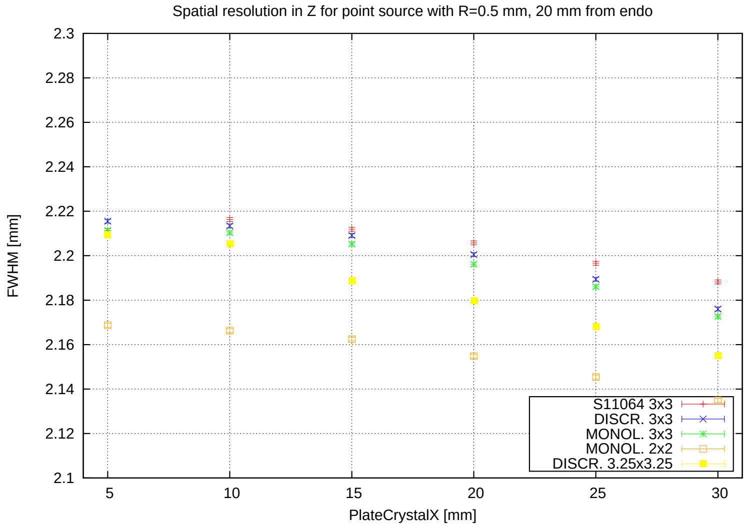

Figure 6.16: Spatial resolution along Z axis for different SiPM models.

- Considering the SiMP models, spatial resolution values shows a very small difference and they can be considered practically equal. A finer reconstruction algorithm may be able to show a different result. From a 3×3 mm^2 active area SiPM array to a 2×2 mm^2 model we gain a 2% of spatial resolution.

6.3.4 Extended source

Simulating human body and single organs is mandatory to test EndoTOFPET scanner response in a configuration as close as possible to real conditions. Before starting these simulations I decided to try an intermediate complexity, using a source surrounded by a low radiation liquid volume. I simulated a 14 mm side cubic box filled of water. Inside this volume I uniformly distributed a source with a total activity of 659.000 kBq. Inside the box I placed three not aligne point sources. The sources have different radii (0.5 mm or 1 mm) and each activity was chosen to have source-background activity concentration ratio of $\approx 8 : 1$. As in previous simulations I used 8 detector positions over a 360° angle with an acquisition time of 60 s each. This yields about 6.3×10^6 singles for the plate and 3.1×10^6 singles for the probe (see Figure 6.18).

When the radioisotope is injected in the body, it flows in the circulatory system and reaches the examined organs but also the nearest tissues. It creates a background noise surrounding the main source which can be simulated using the just defined extended source. Moreover gammas moving in water can be scattered by Compton

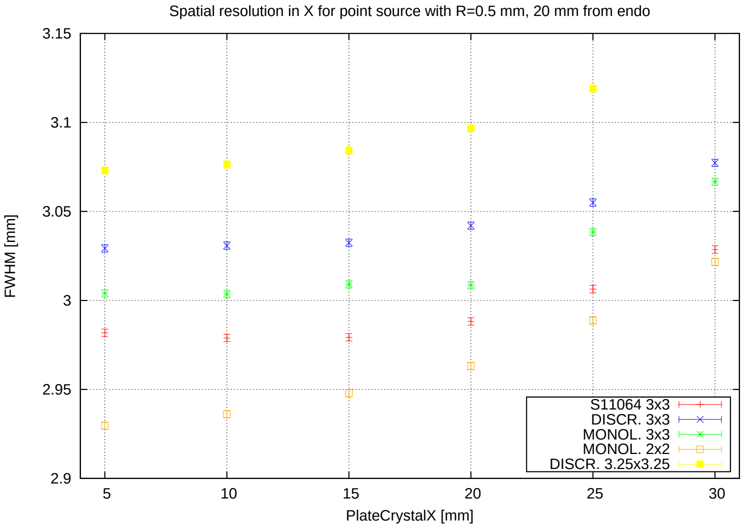

Figure 6.17: Spatial resolution along X axis for different SiPM models.

interaction and create false coincidences (see Section 2.1.3) as it can happens in human body. This is another source of noise for our image reconstruction similar to real conditions.

From the result of a single simulation I run several times the CS using different single time resolution values (STR): 4.25, 35, 50, 100, 150, 200, 300 ps equals for both detectors. The STR is the precision of a PET scanner plate to detect the arrival time of a gamma. If we consider both heads having the same STR value we are able to calculate the overall precision of the scanner using Equation 6.3.1 that gives us the coincidence time resolution:

$$CTR = \sqrt{2} \cdot STR \tag{6.3.1}$$

Some of these values are far from the real possibilities EndoTOFPET scanner has but they were used to test CTRs compatible with the source dimension. Assuming that two gammas are generated at the same time at the opposite sides of the water box and they are running along the X axis, the time difference between their arrival on one of the detector is:

$$\Delta t = \Delta z / c = 46\ ps \qquad for\ z = 14\ mm \tag{6.3.2}$$

Only with STRs quite below 46 ps it is possible to resolve the positions of the two gammas from their TOF. I reconstructed an image for each CTR applied in the CS and I calculated the spatial resolution in the z direction for the 1 mm radius

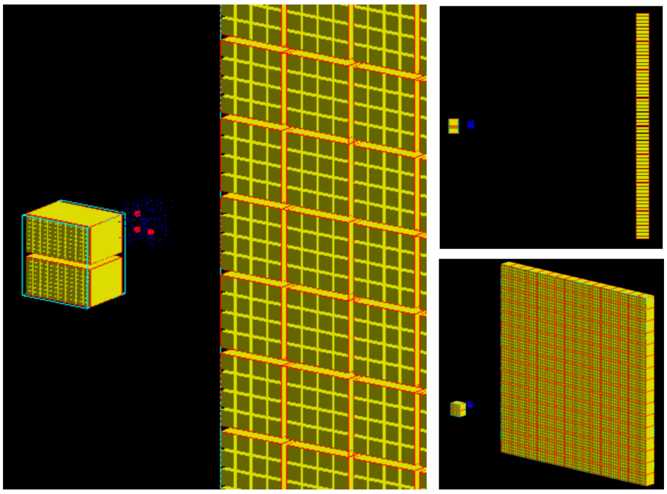

Figure 6.18: Simulation of a multifocal source in a background noise volume.

STR (ps)	CTR (ps)	Spatial resolution (mm)
4.25	6	1.84 ± 0.06
35	49.5	2.13 ± 0.12
50	70.7	2.22 ± 0.14
100	141.4	2.30 ± 0.17
150	212.1	2.35 ± 0.18
200	282.8	2.35 ± 0.17
300	424.3	2.39 ± 0.17

Table 6.5: Spatial resolution obtained applying different values of STR.

source. From Table 6.5 it is possible to see that our reconstruction is sensitive also to higher STRs but only with very small values we can obtain good differences.

Images 6.19 and 6.20 show the reconstructed source in transverse and coronal view.

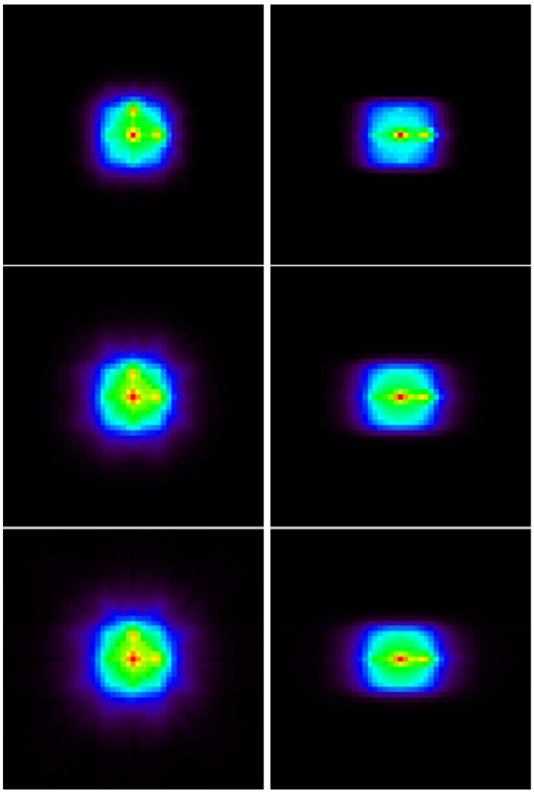

Figure 6.19: Transverse (left) and coronal (right) view for the 6, 49.5 and 70.7 ps CTR image reconstruction.

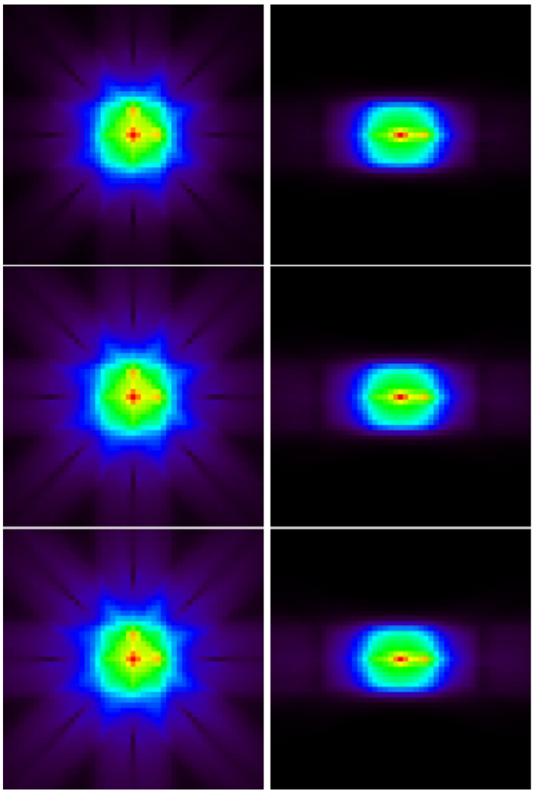

Figure 6.20: Transverse (left) and coronal (right) view for the 141.4, 212.1 and 282.8 ps CTR image reconstruction.

Chapter 7

Conclusions

Monte Carlo simulations are a powerful tool for physicists thanks to the possibility to predict particles behaviour in reconstructed experimental set-up. EndoTOFPET collaboration has decided to employ this method to support the development of the innovative high spatial resolution endoscopic PET scanner. We have chosen to adopt GATE, a software dedicated to nuclear medical imaging scanners based on Geant4 libraries. It proved to be particularly useful to construct the detector geometry but it is not able to simulate the electronics chain because of the asymmetry of EndoTOFPET modules. It required the development of a custom software that was able to read the output of a simulation and create the list the coincidence events for the reconstruction algorithm. The software can be tuned to simulate noise and the possible inaccuracy of an electronic chains and different method to discriminate true, random and scattered coincidences can be chosen. With this tool I started simulating simple cases where different plates geometries were tested, in particular taking into account two parameters: sensibility and spatial resolution. I simulated several SiPM arrays and crystals dimensions that the collaboration is investigating for their application in the scanner prototype. At this status of simulation I obtained a spatial resolution between 2.9 and 3.1 mm along the main axis and 2.1 and 2.2 mm along z-axis depending on the configuration applied. DOI error are evaluated to be independent to crystals length in our simulation, hence pushing the EndoTOFPET-US collaboration to the single plate readout choice. We moved from simple point sources to extended sources in order to simulate with more accuracy organs or human body. Thanks to this implementation we are able to study the effect of coincidence time resolution in the TOF as shown by the first results.

Bibliography

[1] *Crystal clear collaboration.* [Online]. Available: http://crystalclear.web.cern.ch/

[2] O. S. Brüning, P. Collier, P. Lebrun, S. Myers, R. Ostojic, J. Poole, and P. Proudlock, *LHC Design Report.*, Geneva: CERN, 2004.

[3] *Compact Muon Solenoid*, [Online]. Available: http://cms.web.cern.ch/

[4] Miles N. Wernick, John N. Aarsvold, *Emission tomography, the Fundamentals of PET and SPECT.*, Elsevier, 2004.

[5] E. B. Podgorsak *Radiation Physics for Medical Physicists*, Springer, 2006.

[6] S. De Benedetti, C. E. Cowan,W. R. Konneker and H. Primakoff, *On the angular distribution of 2-photon annihilation radiation*, Phys. Rev. 77, 205-12, 1950.

[7] WW. Moses *Fundamental Limits of Spatial Resolution in PET.*, Nucl. Instrum. Methods Phys. Res. A., 648 Supplement 1:S236-S240, 2011.

[8] *World Cancer Repor"*, International Agency for Research on Cancer. 2008. Retrieved 2011-02-26.

[9] B. Frisch, *Development of ClearPEM-Sonic - a multimodal positron emission mammograph and ultrasound scanner*, *in Nuclear Science Symposium and Medical Imaging Conference (NSS/MIC)*, 2011 IEEE, oct. 2011, pp. 2267-2272.

[10] P. Lecoq and J. Varela, *Clear-pem, a dedicated pet camera for mammography*, Nuclear Instruments and Methods in Physics Research, A, vol. 486, pp. 1-6, 2002.

[11] M. C. Abreu, D. Aguiar, E. Albuquerque, F. G. Almeida, P. Almeida, P. Amaral, E. Auffray, P. Bento, P. Bruyndonckx, R. Bugalho et al., *Clear-PEM: a PET imaging system dedicated to breast cancer diagnostics*, Nuclear Inst. and Methods in Physics Research, A, vol. 571, no. 1-2, p. 81-84, 2007.

[12] M. Pizzichemi, N. Di Vara, G. Cucciati, B. Frisch, A. Ghezzi, M. Paganoni, F. Farina, and R. Bugalho, *Image fusion software in the clearpem-sonic project*, in 13th ICATPP Conference on Astroparticle, Particle, Space Physics and Detectors for Physics Applications, 2011, submitted.

[13] L. Tessonnier, et al, *ClearPEMSonic: imagerie mammaire multimodale couplant PEM et échographie: aspects techniques et résultats cliniques préliminaires*, Médecine Nucléaire 36.4 (2012): 190.

[14] EndoTOFPET-US, *Novel Multimodal Endoscopic Probes for Simultaneous PETlUltrasound Imaging for Image-guided Interventions*, European Union 7th Framework Program (FP7 /2007 -2013) under Grant Agreement No. 256984, HEALTH-20 10.1.2-1.

[15] S. Mandai and E. Charbon, *Multi-Channel Digital SiPMs: Concept, Analysis and Implementation.*, IEEE Nuclear Science Symposium, Anaheim, Oct. 2012.

[16] Glenn F. Knoll, *Radiation Detection and Measurement.*, John Wiley & Sons, 2000.

[17] P. Lecoq, A. N. Annenkov, A. Gektin, M. Korzhik, C. Pédrini, *Inorganic Scintillators for Detector Systems. Physical Principles and Crystal Engineering.*, Berlin: Springer, 2006.

[18] M. Born, E. Wolf, *Principles of Optics: Electromagnetic Theory of Propagation, Interference and Diffraction of Light*, Cambridge University Press, 1999.

[19] Stanislaw Ulam, Eckhardt, 1987.

[20] Anderson, H.L. *Metropolis, Monte Carlo and the MANIAC*, Los Alamos Science 14, 96–108,(1986).

[21] Geant4 collaboration, S. Agostinelli et al., *GEANT4 - A simulation toolkit*, Nucl. Instrum. Meth. A506 250-303, 2003.

[22] *Geant4*, [Online]. Available: http://geant4.web.cern.ch/geant4/ .

[23] F.X. Gentit, *Litrani: a general purpose Monte-Carlo program simulating light propagation in isotropic or anisotropic media*, Nucl. Instrum. Meth. A486, 35-39, 2002.

[24] *ROOT*, [Online]. Available: http://root.cern.ch/drupal/ .

[25] *SLitrani*, [Online]. Available: http://gentitfx.fr/SLitrani/ .

[26] S. Baccaro, L.M. Barone, B. Borgia, F. Castelli, F. Cavallari, I. Dafinei, F. De Notaristefani, M. Diemoz, A. Festinesi, Emanuele Leonardi et al. *Ordinary and extraordinary complex refractive index of the lead tungstate (PbWO-4) crystal*, Nucl.Instrum.Meth. A385 (1997) 209-214.

[27] M. Lebeau, A. N. Annenkov, O. N. Kovalev, V. D. Ligun and V. A. Venetsev, *Cutting of five PbWO4 crystals in industrial prototype conditions*, CMS Note, 1997 .

[28] *Bogoroditsk Plant of Technochemical Products*, [Online]. Available: http://www.btcp-crystal.com/ .

[29] S. Jan et al. *GATE: A simulation toolkit for PET and SPECT*,Phys. Med. Biol. 49 4543, 2004.

[30] A. Cserkaszky, B. Frisch, M. Zvolsky, G. Cucciati, *Reconstruction of freehand PET examinations*, Wims, P 595, 2013.

[31] *WLCG, worldwide LHC computing grid*, [Online]. Available: http://wlcg.web.cern.ch/ .